Structural studies of the 5-HT3 receptor

Lucie Polovinkin

Communauté
UNIVERSITÉ Grenoble Alpes

THÈSE

Pour obtenir le grade de

DOCTEUR DE LA COMMUNAUTÉ UNIVERSITÉ GRENOBLE ALPES

Spécialité : **Biologie Structurale et Nanobiologie**

Arrêté ministériel : 25 mai 2016

Présentée par

Lucie Polovinkin

Thèse dirigée par **Hugues Nury** et
codirigée par **Stéphanie Ravaud**

préparée au sein du l'Institut de Biologie Structurale
dans **l'École Doctorale Chimie et Sciences du Vivant**

Etudes structurales du récepteur 5-HT3

Thèse soutenue publiquement le **18 Octobre 2019,**
devant le jury composé de :

M. Franck FIESCHI Professeur UGA Grenoble	Président
M. Martin PICARD Directeur de Recherche IBPC Paris	Rapporteur
Mme. Sarah LUMMIS Professeur University of Cambridge	Rapporteur
M. Jean-Michel JAULT Directeur de Recherche MMSB Lyon	Examinateur
Mme. Stéphanie RAVAUD Maître de conférences IBCP Lyon	Membre

Abstract

Cys-loop receptors are pentameric ligand-gated ion channels (pLGIC), which play a crucial role in rapid neurotransmission. They are the targets of a legion of drugs (antiemetics, general anesthetics, benzodiazepines, smoke cessation drugs, etc.) and their physiological properties are intensively studied. When pLGICs bind neurotransmitters, they undergo conformational changes, from a resting closed pore state to a transient open pore state; they can also enter a ligand-bound, closed pore, desensitized state. Moreover, the gating properties of pLGICs can be influenced by a variety of compounds (e.g. lipids, competitive inhibitors, allosteric modulators, ions such as Ca^{2+}), which makes them flexible receptors capable of integrating different signals into conformational changes.

In this thesis we focus on structural studies of the mouse serotonin type 3 receptor (m5-HT3R). The first structure of the m5-HT3R, obtained by X-ray crystallography using stabilizing nanobodies, was a closed pore inhibited conformation *(Hassaine et al., 2014)*. As a follow up, we aimed to obtain structures of the m5-HT3R in other conformations, in order to elucidate its gating mechanism. For this purpose we used both X-ray crystallography and cryo-electron microscopy and thus the whole thesis follows two story-lines.

A general introduction of the pLGIC family is followed by a detailed structural description of the m5-HT3R. In the results section, we present the optimized protocol for the receptor purification, we report that limiting diffraction is a bottleneck in the crystallographic trials and we emphasize limits met using nanobodies for conformational stabilization of the receptor. In the electron microscopy results part we present the optimization of the sample and grid preparation that ultimately permitted data collection. We report four different structures representing distinct functional states of the m5-HT3R: an inhibited tropisetron-bound closed conformation, an open pore state and a putative pre-active state obtained in the presence of serotonin, and finally a closely-related putative pre-active state in the presence of serotonin and of the allosteric modulator TMPPAA. We compare our data with structures of the same receptor obtained by other laboratory.

It was shown for the first time in our work how the antagonist (tropisetron) and the neurotransmitter (serotonin) bind to the full-length m5-HT3R. And our structures deepen the knowledge of the receptor's gating mechanism.

Résumé

Les récepteurs Cys-loop sont des canaux ioniques pentamériques activés par un ligand (pLGIC), qui jouent un rôle essentiel dans la neurotransmission rapide. Ils sont la cible de nombreuses familles de médicaments (antiémétiques, anesthésiques généraux, benzodiazépines, médicaments pour arrêter de fumer, etc.) et leurs propriétés physiologiques sont, en conséquent, très étudiées. Lorsque les pLGIC lient des neurotransmetteurs, ils subissent des modifications conformationnelles, d'un état au repos où le pore est fermé vers un état transitoire ouvert. La liaison de ligand peut également provoquer un état conformationnel fermé et désensibilisé. En outre, les propriétés des pLGIC peuvent être influencées par divers composés (lipides, inhibiteurs compétitifs, modulateurs allostériques, ions tels que Ca^{2+}), ce qui en fait des récepteurs capables d'intégrer différents signaux via des changements de conformation.

Dans cette thèse, nous nous concentrons sur des études structurales du récepteur de la sérotonine de type 3 chez la souris (m5-HT3R). La première structure du m5-HT3R, obtenue par cristallographie aux rayons X, représentait une conformation inhibée à pore fermé, stabilisée par des nanobodies *(Hassaine et al., 2014)*. Nous avons cherché à obtenir des structures dans d'autres conformations, afin d'élucider son mécanisme moléculaire de fonctionnement. Pour ce faire, nous avons utilisé à la fois la cristallographie aux rayons X et la cryo-microscopie électronique. Les résultats obtenus sont décrits dans 2 chapitres dédiés de la thèse.

Une introduction générale de la famille pLGIC est suivie par une description détaillée de la structure du m5-HT3R. Dans la section résultats, nous présentons le protocole optimisé pour la purification du récepteur, nous expliquons que la mauvaise diffraction est un facteur limitant dans les essais cristallographiques, et nous montrons les freins rencontrés lors de l'utilisation des nanobodies pour la stabilisation conformationnelle du récepteur. Dans les résultats de la microscopie électronique, nous présentons l'optimisation de la préparation de l'échantillon et de la grille qui a finalement permis la collecte de données. Nous décrivons quatre structures différentes représentant des états fonctionnels distincts du m5-HT3R : une conformation inhibée fermée liée au Tropisétron ; un état ouvert et un état pré-actif présumé obtenus en présence de sérotonine ; et enfin un état proche de l'état pré-actif supposé, en présence de sérotonine et du modulateur allostérique TMPPAA. Nous comparons nos données avec les structures du même récepteur obtenues par un autre laboratoire.

Notre travail a montré pour la première fois comment l'antagoniste (Tropisétron) et le neurotransmetteur (sérotonine) se lient au m5-HT3R. Nos structures approfondissent également la connaissance du mécanisme d'action du récepteur.

Table of content

Acknowledgements

J'aimerai bien exprimer mes remerciments les plus profondes à mon encadrant Hugues Nury pour son imense soutien. Pour qu'il a cru en moi meme pendant la period difficile, pour sa incommesurable tranquilité et elegance avec lesquelles il a dirigé mon project. Merci pour toutes les moments inoubliables quand j'avais la possiblité d'appreindre de toi et pour ton patience avec moi. Tu est et tu va rester la plus forte motivation pour ma future carrière scientifique.

I would like to express my sincere gratitude to all committee members: Franck Fieschi, Jean-Michel Jault, Sarah Lummis, Martin Picard and Stéphanie Ravaud for a kind agreement to spend their precious time reading and correcting my manuscript, travelling to the defence and thinking about our research in general. Thank you all!

I am deeply grateful to all the current and former members of the laboratory. To Eva Pebay-Peyroula for giving me the chance to join her lab and showing me, that there is a way how to combine science and family and that time can be used super-efficiently, if you are organised. To Stéphanie Ravaud for being my co-supervisor and helping me whenever I needed her. To Jacques Neyton for all his kind permissions regarding the work during weekends and his advices: "c'etait un grand honneur de travailler avec toi!". To Céline Juillan-Binard and Delphine Baud for taking a perfect care about the order, chemicals and instruments, what was making the work in the lab so much easier. To Jonathan Perot for mastering our cell-cultures and protein overexpression and most importantly for his inspiring neatness. To Sonja Minniberger, best master student I have ever met, for her permanent cheerful spirit. To Orso Subrini for his helpful attitude and smart ideas. To Hubert Mayerhofer for showing me, that if you have a reasonable idea it is faster to test if it works rather than to talk about the reasons why it might not work. To Yann Huon de Kermadec for his suppor during my lab and social incorporations. To Florine Dupeux for putting herself out for me. And also to Aleksandra Woźnicka-Misăilă, Georgy Derevyanko and all our stagiaires.

Thank you, all lab members, for being a great team which makes the definition of "lab" being: a place where people are sharing the passion for science in an outstandingly friendly atmosphere. I will miss you all.

I really appreciate the help of our collaborators: Ghérici Hassaine, Lamia Mebarki,

Anders A. Jensen, Emmanuelle Neumann, Anders A. Jensen, Solene N. Lefebvre, Pierre-Jean Corringer, Christophe Chipot, Francois Dehez, whose work is stressed in my thesis and in the enclosed publication. Many special thanks go to Guy Schoehn for his patience and for the precious time on microscope which he shared with us.

Děkuji mé rodině. Rodičům, prarodičům a bráchovi. Můj odchod do zahraničí byl náročným obdobím pro Vás všechny. Nesmírně si vážím Vaší podpory, protože bez ní bych to nikdy nedokázala. Každý z Vás je pro mě jedinečnou inspirací a nekonečným zdrojem k osobnímu rozvoji. Děkuji, že mě tolik milujete. Jsem šťastná, že můžeme být spolu, protože jsou to pro mě jedny z nejdůležitějších chvilek v životě.

At last, but certainly not least, I would like to say "большое спасибо" to my husband who was standing by my side, being my personal and scientific support and to our little daughter Adriana. You are my life drive, please "Stand by me".

A special thank belongs to Dr. Kvido Strisovsky who helped me in my non-standard situation.

Abbreviations

5-HT3R	serotonin receptor of type 3
5-HT	5-hydroxytryptamine
$C_{12}E_{10}$	polyoxyethylene(10)dodecyl ether
$C_{12}E_9$	polyoxyethylene(9)dodecyl ether
CHS	cholesteryl hemisuccinate
CINV	chemotherapy induced nausea and vomiting
CMC	critical micellar concentration
CNS	central nervous system
cryo-EM	cryo-electron microscopy
Cymal5	5-cyclohexyl-1-pentyl-β-D-maltoside
Cymal6	6-cyclohexyl-1-hexyl-β-D-maltoside
Cymal7	7-cyclohexyl-1-heptyl-β-D-maltoside
DDM	dodecyl-maltoside
DHA	docosahexaenoic acid
ECD	extracellular domain
Fab	antigen-binding fragments
FEG	field emission gun
Fos-C12	n-dodecylphosphocholine
F-TAC	fluorinated surfactant
GluCl	glutamate receptor
GlyR	glycine receptor
ICD	intracellular domain
LAPAO	3-dodecylamido-N,N'-dimethylpropyl amine oxide
LCP	lipidic cubic phase
LDAO	lauryldimethylamine-N-oxide
MNG3	maltose neopentyl glycol-3
nAChR	nicotinic acetylcholine receptor
NMR	nuclear magnetic resonance

OGNG	octyl glucose neopentyl glycol
OG	octyl glucoside
PAGE	polyacrylamide gel electrophoresis
PA	phosphatidic acid
PC	Phosphatidylcholines
pLGIC	pentameric ligand-gated ion channel
PNS	peripheral nervous system
RMSD	root-mean-square deviation
SCAM	substituted cysteine accessibility mutagenesis
SDS	sodium dodecyl sulfate
SEC	size exclusion chromatography
TMD	transmembrane domain
UDM	undecyl-maltoside
VCS	voltage-clamp fluorometry
XFEL	X-ray free-electron laser

Table of figures

1 Introduction

When someone is searching for a job, her/his abilities to communicate represent one of the most appreciated skills by human resource recruiters. In biological processes communication also plays a very important role. Unicellular organisms developed the ability to recognise stimuli coming from their surroundings, ways to process the information, and signalling pathways which allow these stimuli to be acted upon (e.g. chemotaxis as a response to a chemical stimulus). Cells in multicellular organisms need to communicate with each other to properly develop into different tissues and organs, fulfil their desired role depending on the cell type, accommodate to external conditions and react to the requirements of the organism. The scope of this thesis is the structural study of a ligand-gated ion channel, which mediates crucial communication, which takes place in excitable cells.

As early as the 19th century, neurons were declared to be the functional building blocks of the nervous system and defined to be independent cells, able to transfer directionally a signal from dendrite towards axones, and the Nobel prize was awarded to Santiago Ramón y Cajal and Camillo Golgi in 1906 for these discoveries. At that time, the propagation of the signal through neurons was not well understood. The development of electrophysiology during the 20th century permitted the mechanism of signal propagation to be elucidated and emphasised the role of ion channels in this process, Nobel prize in Physiology and Medicine awarded to Alan Hodgkin and Andrew Huxley in 1963. Our current molecular understanding of how ion channels operate arises in part from the ability to obtain atomic structures by crystallography or cryo-electron microscopy since the turn of the millennium *(Doyle, 1998; Liao et al., 2013)*.

1.1 Action potential

The neuronal signal transfer is divided into two stages: I) propagation along the nerve cell through changes in the membrane potential (electrical signal) and II) the transmission of the signal at the neuron-neuron interface called the synapse, mediated by neurotransmitters (coupling).

The cytoplasmic membrane is the semi-permeable hydrophobic barrier which encloses all living cells. While small hydrophobic molecules can diffuse across membranes, charged molecules such as ions cannot and thus they require specialised proteins to transport them. There are two types of transport across the membrane.

Active transport mediated by pumps and transporters consumes energy to transport molecules against their chemo-electrical gradient. Passive transport occurs along a gradient and is mediated by channels.

Concentrations of ions differ at the interior and exterior side of the plasma membrane. In a typical neuron, there are more Na^+ ions outside than inside the cell whereas the opposite is true for the K^+ ions (Fig. 1).The general charge imbalance on different sides of membrane creates electrical field, negative inside, called membrane potential. Polarised neurons have a resting membrane potential of about -70 mV. This polarisation is maintained by sodium/potassium pumps and K^+ channels. For two K^+ pumped in 3 Na^+ ions are pumped out of the nerve cell. If an excitatory stimulus reaches the neuron in the resting state, this results in the opening of ion channels and the passage of sodium ions into the cell. If the stimulus is strong enough, the potential may reach -55 mV and thus overcome a barrier for an all-or-nothing phenomenon. At this threshold, the change of the potential triggers the opening of voltage-gated ion channels, which mediate further depolarisation. This depolarisation is then propagated along the neuronal body to the axon terminal - to the synapse. In synapses, the depolarisation opens calcium channels, yielding a flux of Ca^{2+} into the presynaptic terminal. The rise in presynaptic calcium concentration triggers the fusion of intracellular vesicles, filled with neurotransmitters, with the presynaptic membrane and the liberation of neurotransmitters into the synaptic cleft. Ligand-gated ion channels located in the postsynaptic neuronal membrane bind these neurotransmitters, open and let some ions pass through the membrane of the cell. This can result in the depolarisation or hyperpolarisation (depending on the channel selectivity) of the new neuron and the message may eventually be transported through this new neuron as described above.

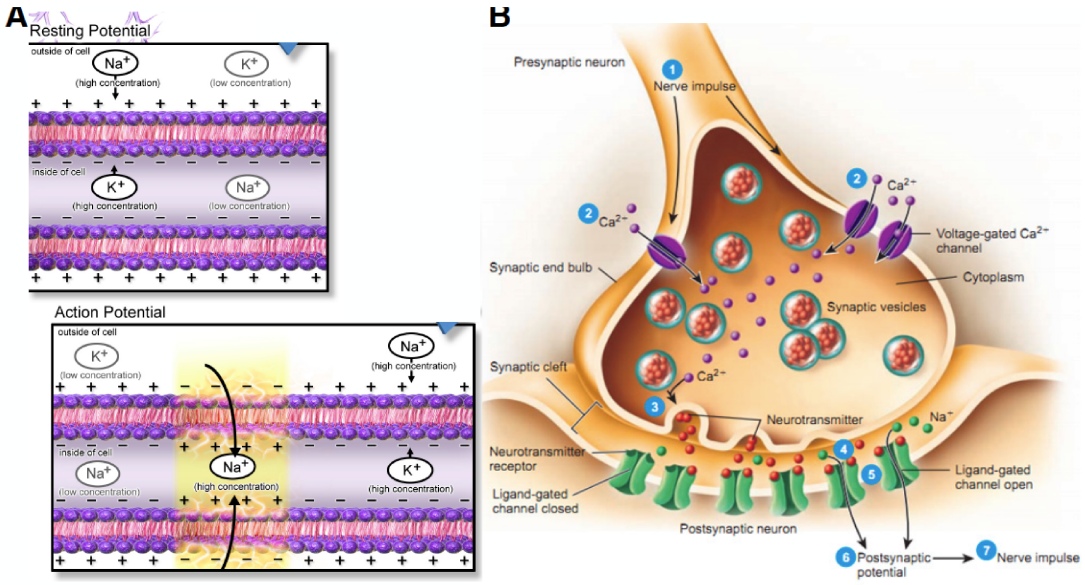

Figure 1 | A schematic of the resting and the action potential and a detailed view of the electric-to-chemical signal transition at the synapse.

A) In the resting state the neuronal membrane is positively charged on the outer and negatively charged on the inner side. The stimulus causes the inward flux of sodium cations. If the -55 mV barrier is overcome, the voltage-gated ion channels are activated and the signal is propagated along the axon. (image adapted from *(Blaus, 2014)*. **B)** When the stimulus reaches the axon termini, voltage-gated calcium channels allow the penetration of the Ca^{2+} ions, mediating neurotransmitter release into the synaptic cleft. Neuron-to-neuron communication occurs through those neurotransmitters interacting with the ligand-gated ion channels located in the postsynaptic neuronal membrane. Once those channels are open the ions can pass into the neuron and the chain of reactions allowing signal propagation continues. Adapted from *Antranik Kinartna*.

1.2 The ion channels

Because of their crucial role in the nervous system the ion channels have been intensively studied more than 60 years *(Hodgkin and Huxley, 1952)*. Together with the G-protein coupled receptors and kinases, the pore forming units of ion channels are amongst the most abundant genes in the human genome. Almost all ion channels are composed of several subunits and form homomers or heteromers. The existence of different heteromers increases the number of the variants of a certain type of ion channel compared to the number of different subunits encoded by DNA sequences. Differences between the subunits modify the channel properties and thus support their specialisation and plasticity. Functional channels of various oligomeric states exist, from dimeric channels up to hexameric ones. Very often subunits are arranged around a central pseudo-symmetrical axis perpendicular to the plane of the membrane, which coincides with the pore (Fig. 2).

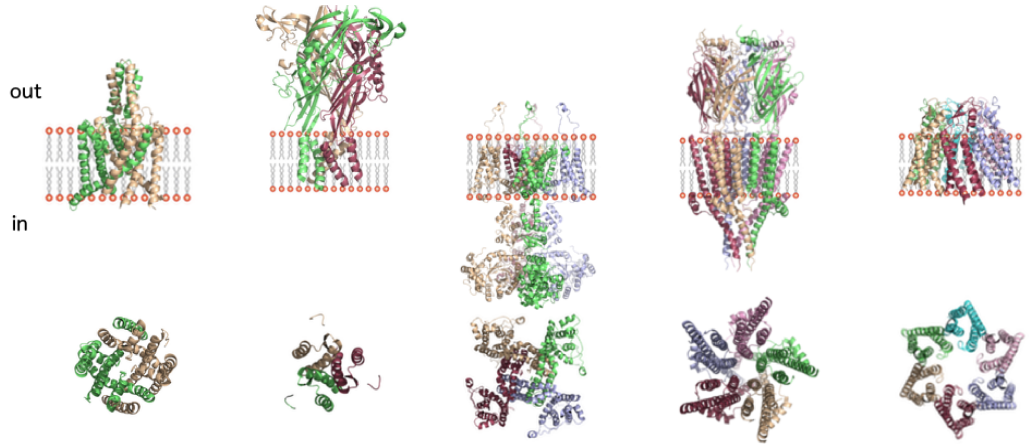

Figure 2 | Comparison of the architecture of ion channels and membrane gap junction proteins of different oligomeric states.

Side view (upper panel) and top view (lower panel) of the membrane domains of several ion channels ranging from dimeric to hexameric composition. From left to right: dimeric TREK 2 channel (each subunit has two pore-domain motifs) (PDB 4XDK), trimeric ATP-gated P2X3 ion channel (PDB 5SVJ), tetrameric potassium channel Kv 1.2 (PDB 3LUT), pentameric 5-HT3 receptor (PDB 4PIR), and hexameric gap junction protein (PDB 5ER7).

The ion channels do basically two things: they close or open to let the ions pass through the highly hydrophobic core of the membrane. The channel stays in its open or closed state(s) several milliseconds, and the conformational change from the opened to closed gates occurs in the order of a hundred times per second with the flux of 10^{6-7} ions/s *(Gadsby, 2009)*. The ion channels are either strictly selective to the certain type of ions (e.g. K^+ *(Roux, 2017)*) or they manifest promiscuity among either cations or anions (e.g. 5-HT3 channel among cations, Na^+, K^+, Ca^{2+} etc. and even some organic cations *(Yang, 1990)*. We distinguish two classes of ion channels: the leaky and gated ion channels. Leaky channels show constitutive opening, and even if they can be regulated by external factors (e.g heat or mechanical stress for TREK channels), they do not directly participate in rapid neurotransmission. The determining characteristic of gated channels is their ability to react to different stimuli coming from their environment, and their rapid response. They all possess a "gate'', which is closed in the resting state and open only once the correct stimulus is detected. Depending on the signal the channels recognise, they can be classified into further subgroups. Voltage-gated ion channels, as the name suggests, react to changes of the membrane potential and this group comprises for example of the K^+, Na^+ and also the Ca^{2+} channels. Members of another class of gated ion channels respond to mechanical stimuli. The last group of gated channels are the ligand-gated ion channels. Their opening is dependent on the binding of a chemical compound. This last group comprises

of several super-families: the tetrameric glutamate receptors, the TRP channels, the ATP-gated ion channels and the Cys-loop receptors. The Cys-loop receptors are pentameric ligand-gated ion channels and as the serotonin receptor of type 3 (5-HT3R), which is the focus of this thesis, belongs to this family, they are discussed in more detail in the following sections.

1.3 Discovery and characteristics of pLGIC

The mechanism behind the chemo-electrical conversion during neurotransmission has been intensively studied since the beginning of the 20th century. The main limiting factors during that period were the available methods and the biological accessibility of the material studied. Key discoveries were made hand in hand with the development of the pharmacological, electrophysiological and biochemical methods.

Emil du Bois-Reymond, known as the father of electrophysiology, was able to detect electrical signals in frog muscle in 1843 and 4 years later, with an improved instrument, he was able to repeat his experiment in humans. In 1868 one of his followers, Julius Bernstein, measured the first action potential across the cellular membrane. In 1902 he formulated the membrane theory further developed by Howard Curtis and Kenneth Cole. After the proposition of ion channel existence in 1952 by Alan Hodgkin and Andrew Huxley, the first direct observation of single functioning ion channels was obtained in the 1970s by the "patch clamp" electrophysiology method invented by Erwin Neher and Bert Sakmann. A breakthrough took place with the injection of brain extracted mRNA into *Xenopus laevis* oocytes, leading to functional ion channel expression at the cell surface, which could be characterised by electrophysiology *(Gurdon et al., 1971)*. This approach helped to overcome the fact that sequencing and cloning techniques were not available during that period and thus it was not possible to identify and overexpress the protein of interest. Those limiting factors were solved by two biological factors in the case of the nicotinic acetylcholine receptor (nAChR), which made it the first pLGIC discovered and characterised. First, cells of the electric organ from *Electrophorus electricus (Nachmansohn, 1959)* were shown to be extraordinarily rich in the acetylcholine neurotransmitter sensing receptors. This tissue provided sufficient amounts of working material but it was only of low specificity. The second biological factor that helped to identify the sensing unit was the discovery of a snake venom component, the alpha-bungarotoxin *(Chang and Lee, 1963)*, which specifically binds to the nAChR receptor and was shown to be a blocker of neurotransmission. A close homologue of this toxin, linked to Sepharose beads, served

as the first tool for the affinity purification of receptors. This breakthrough helped to clarify that it is the nAChR and not the acetylcholinesterase that interacts with the toxin. The nAChR was determined to be the bearer of the neurotransmitter response.

In parallel with the advancements being made on the nAChR, the inhibitory neurotransmitters glycine and γ-aminobutyric acid (GABA) were used to identify their receptors, which were both purified in 1982 *(Pfeiffer et al., 1982; Stephenson et al., 1982)*. Only five years later the DNA regions encoding these two receptors were sequenced *(Grenningloh et al., 1987; Schofield et al., 1987)* and shown to be homologous to the nAChR. The Cys-loop receptor family was further enlarged with the cloning, expression and characterisation of the 5-HT3R *(Maricq et al., 1991)* and the invertebrate glutamate-gated chloride channels (GluCl) *(Cully et al., 1994)*. Prokaryotic homologues were also identified using sequence analysis *(Tasneem et al., 2005)*. Two of them, originating from *Gloeobacter violaceus* (proton-gated GLIC receptor) and *Erwinia chrysanthemi* (GABA-gated ELIC receptor) have been extensively studied in structure-function projects aimed at understanding gating and transitions. These two receptors lack the characteristic Cys-loop and thus the alternative name - pentameric ligand-gated ion channels can be considered as more precise. All receptors from this family share a similar architecture but the prokaryotic receptors lack the intracellular domain (ICD).

The pentameric ligand-gated ion channels are classified according to their ion selectivity. The nAChRs and 5-HT3Rs are cation-selective channels, so movement of ions through them causes a depolarisation of the membrane (excitatory postsynaptic potential). Conversely, the glycine receptor (GlyR) and the GABAA receptors (GABAAR) are anion-selective channels and movement of ions through them leads to a hyperpolarisation (inhibitory postsynaptic potential). Both prokaryotic homologues GLIC and ELIC are cation selective.

The variety of the genetically encoded subunits and the ability of the cell to compose pentamers composed of diverse subunits adds to the overall functional plasticity and physiological properties of the receptors. The human genome codes for about 19 different subunits of GABAAR and for 17 different subunits of nAChR. Smaller diversity is observed for the GlyR represented by only 5 different subunits as well as for the 5-HT3R where the five different subunits carry the names from A-E. The phylogenetic relationships between the different subunits of each receptor class are shown in (Fig. 3).

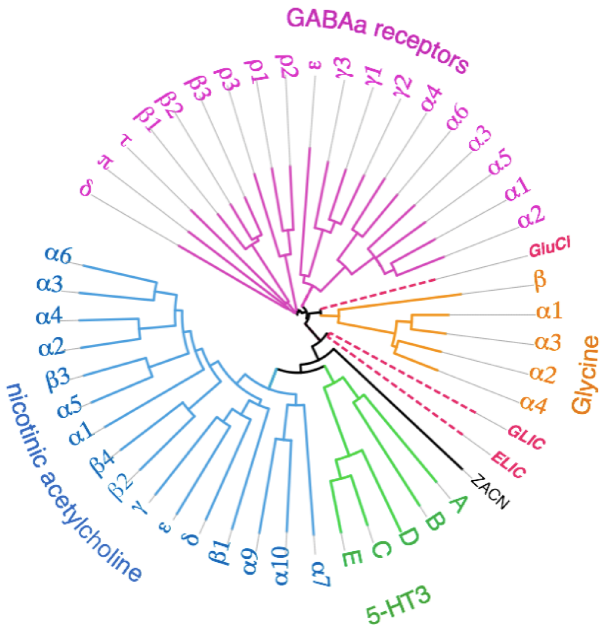

Figure 3 | Bayesian sequence similarity tree depicting the pLGICs superfamily.

The tree highlights the amount and sequence variability of the subunits of the GABAA, glycine, nicotinic acetylcholine and 5-HT3 receptors.

Generally the working mechanism of all the Cys-loop receptors is the same. They open transiently when an agonist binds but after longer exposure to the agonist they switch into the stimuli ignoring state during which the cellular response decreases. This state is called the desensitised state and ions are not able to pass through the channel in this state. After the washout of the agonist the receptor returns into its resting state directly, without the need for reopening. This entire process was first described for the nAChR *(Katz and Thesleff, 1957)*. Since then, its binding specificity and the binding kinetics have been further studied. It is clear now that a variety of molecules might interact with and dissociate from the receptor with different kinetics, which is further influenced by allostery and that this process might be dependent on the receptor conformational state *(Monod et al., 1965)*.

The Cys-loop receptors are implicated in multiple diseases, for example in anxiety, epilepsy and Alzheimer's disease. They are targets of clinically used anaesthetics, anti-emetics, barbiturates, steroids and on the biological level also of toxins, alcohol and nicotine *(Connolly and Wafford, 2004; Lester, 2004; Thompson et al., 2010)*. I will focus on the detailed functional properties of the 5-HT3R and its structural features compared to the other Cys-loop receptors in the following sections.

1.4 The 5-HT3 receptor. Discovery, composition, physiological properties and pharmacology

5-hydroxytryptamine (5-HT) or serotonin is the neurotransmitter biochemically derived from tryptophan. It is mostly produced in the enterochromaffin cells of the gastrointestinal tract but it is also present in the serotonergic nerves in the central nervous system (CNS). There are seven classes of receptors sensing serotonin - the serotonin receptors. The 5-HT3R is the only ion channel out of the 7 different classes of serotonin receptors. The rest of the serotonin receptors are G protein-coupled receptors and they influence physiological processes such as sleep, memory, learning, respiration, mood, anxiety, locomotion and more (the overview of the G-protein coupled serotonin receptors can be found in the review of *Pytliak et al.(2011)*).

The initial discovery of the 5-HT3 receptor is linked to the determination of the two pharmacologically distinct types of serotonin receptors. The "D" type receptors, which can be inhibited by dibenzyline, mediate the contraction of smooth muscle and the "M" type, which can be inhibited by morphine, cause the depolarisation of the cholinergic neurons in the guinea-pig ileum *(Gaddum and Picarelli, 1957)*. When the classification and the unique nomenclature was established the "M" type serotonin receptors became the 5-HT3 receptors *(Bradley et al., 1986)* and were further characterised as we know them today *(Maricq et al., 1991)*.

5-HT3Rs are located in the peripheral nervous system (PNS) as well as in the CNS *(Tecott et al., 1993)* both, pre- and post-synaptically. The presence of the 5-HT3R was proven in the peripheral preparations of myenteric plexus *(Mawe et al., 1986)*, submucous plexus *(Derkach et al., 1989)*, nodose ganglion *(Higashi and Nishi, 1982)* and vagus nerve *(Azami et al., 1985)*. After its localisation to the PNS, its existence was also proven in the CNS by mapping of the 5-HT3R activity in the rat brain *(Kilpatrick et al., 1987)*. In the CNS, 5-HT3R is localised to the hippocampus, the amygdala, the area postrema and the nucleus tractus solitarius *(Koyama et al., 2017; Miquel et al., 2002)* (Fig. 4).

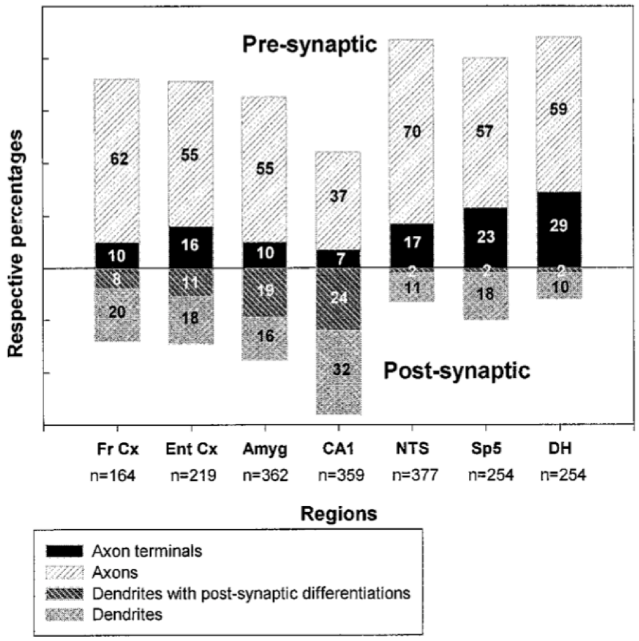

Figure 4 | The localisation of the 5-HT3R in the neurons of the rat CNS.

Even though the post-synaptically located receptors are the better studied ones, the majority of the receptors are present in the presynaptic neuron part - in axons.

Fr Cx, frontal cortex; Ent Cx, entorhinal cortex; Amyg, amygdala; CA1, CA1 field of hippocampal Ammon's horn; NTS, nucleus of the tractus solitarius; Sp5, nucleus of the spinal tract of the trigeminal nerve; DH, dorsal horn of the spinal cord. Taken from *Miquel et al. (2002)*.

Five subunits A-E of the 5-HT3R have been identified to date. The A subunit was followed by the B subunit discovery and expression four years later *(Davies et al., 1999)*. Three more putative 5-HT3R-encoding genes HTR3C, HTR3D and HTR3E were found in the human brain coding for the C-E subunits *(Niesler et al., 2003)*. Some of the subunits exist in a variety of isoforms. The 5-HT3R A subunit (5-HT3RA) has short and long splice variants differing by 32 amino acids, and other post translational variants are also known for the 5-HT3R B (5-HT3RB) and E subunits. The homopentamer receptors can be made only of A subunits *(Davies et al., 1999)*. None of the subunits B-E forms functional homopentamers and moreover the heteropentamers require the presence of at least one A subunit. The functional properties of the C-E subunits and their presence across species is discussed in detail in the work of Holbrook and co-workers *(Holbrook et al., 2009)* and that of Niesler and co-workers *(Niesler et al., 2007)*. The rodents genome codes only for the A and B subunits and interestingly, they never vomit. The absence of the other subunits as a reason of the phenotype is tempting but remains speculative.

The general architecture of all the different subunits is identical. They are composed

of the extracellular domain (ECD) formed mostly by beta-sheets. They have four transmembrane helices. Only helix 2 (M2) is the pore forming helix and the rest of the helices protect it from contact with the lipid bilayer. The M3 helix is connected to the M4 helix by the long M3-M4 loop. C-terminal to the M3 there is a peri-membrane short helix (MX) and then the unstructured longer loop connects the MX helix to the cytoplasmic prolongation of the membrane helix 4 (M4) called the MA helix (Fig. 5). The binding site of the receptor is formed by the contact of the two consecutive subunits. The detailed view of the structural features of the 5-HT3 receptors will be provided in section 1.5.2.

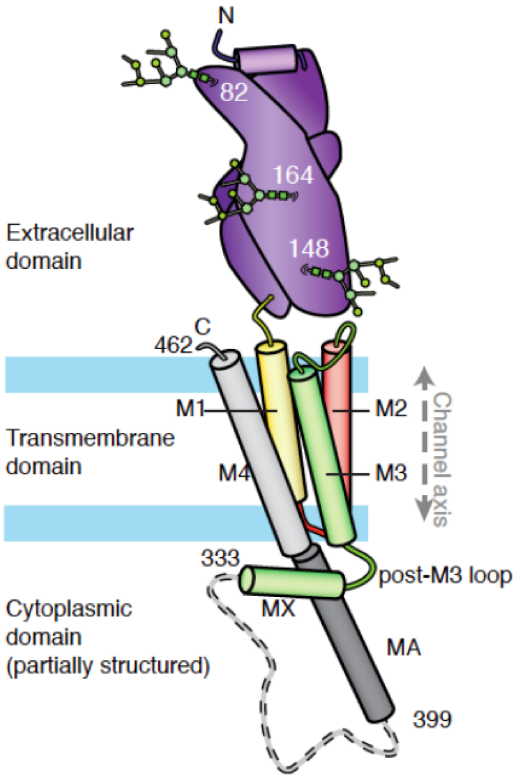

Figure 5 | A schematic of the mouse 5-HT3RA subunit.

A mostly B-sheet extracellular domain with the three glycosylation sites, a membrane domain composed of four membrane helices and the intracellular domain formed by the MX helix, the unstructured part and by the prolongation of the M4 helix called MA. Taken from *(Hassaine et al., 2014)*.

1.4.1 Functional properties

The early electrophysiological studies were performed on isolated tissues or on cells expressing the 5-HT3R naturally *(Hussy et al., 1994)*. Only after the successful isolation of the gene coding for the A subunit were the homopentamers studied in oocytes *(van*

Hooft et al., 1997). The single channel conductance of native 5-HT3Rs was tissue dependent and ranged between 9 and 17 pS *(Fletcher and Barnes, 1998)*, whereas it was only in the sub-pS range for 5-HT3A homopentamers expressed in a heterologous system *(Gill et al., 1995)*. This suggested that multiple forms of the receptor might be present. At first, splice variants of the A subunits were hypothesised to be a source of the heterogeneity but it was shown that the presence variants had only a minor impact on the pharmacological and functional properties of the receptor *(Hope et al., 1993)*. In the end, it was a direct comparison between the heterologously expressed 5-HT3RA and the native receptors of the superior cervical ganglion neurons, which provided the evidence for multiple channel forms. Although the pharmacological properties were nearly identical, the conductance of the heterologously expressed receptors was about 0.4-0.6 pS compared to the 9 pS conductivity of the native receptors *(Hussy et al., 1994)*. Furthermore, the whole-cell noise analysis of the mureine superior cervical ganglion neuron receptor revealed the single-channel conductance of 3.4 pS. This suggested a co-existence between 9 pS conductance channels and channels with a lower conductance. It implied the presence of at least two different forms of the receptors. The B subunit was discovered and shown to be unable to form a functional homopentamer. The conductivity of the A-B heteromers fitted well with the data obtained from the measurements carried out with the 5-HT3Rs expressed natively *(Davies et al., 1999)* (Fig. 6).

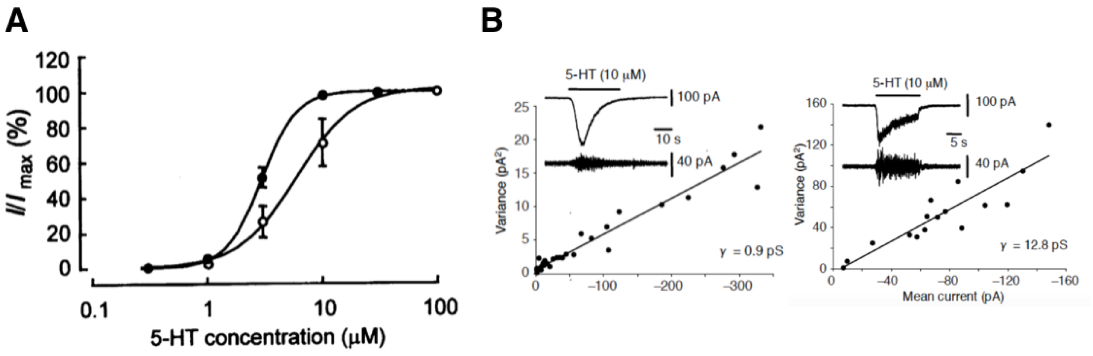

Figure 6 | The comparison of the biophysical and pharmacological properties of homo (only A subunit) and heteropentamers (co-expression of A and B subunit).

A) Concentration-dependent current recorded using HEK cells transfected with the 5-HT3RA cDNA (filled circles) and cells co-transfected with cDNA coding for the A and B subunits (empty circles). The graph shows that higher concentrations of 5-HT are needed to elicit a current response in 5-HT3RB. Taken from *Davies et al. (1999)*. **B)** Whole-cell estimation of the single channel conductance from noise analysis for the m5-H3RA subunit alone (left) and when coexpessed with the m5-HT3RB subunit (right) in tSA201 cells. Taken from *Kelley et al. (2003)*.

To further explain the effect of the B subunit on the conductance, chimeric receptors swapping domains between the A and B subunits were created *(Kelley et al., 2003)*. The conductivity-determining region was shown to be in the cytoplasmic portion of the receptor. The alignment of the sequences of the A and B subunits from different organisms revealed three highly conserved arginine residues (R416, R420, R424) within the cytoplasmic region of the A subunit. When these were mutated to the corresponding residues of the B subunit (R416Q, R420D and R424A) and co-expressed with the WT A subunit, the conductivity increased. Importantly, this conductivity corresponded to the one observed in tissues expressing the A/B heteromers natively. Initially, it was believed that the positive charge of these residues was the main determinant of their role: they would essentially lower the flux of cations exiting the receptor through lateral portals *(Kelley et al., 2003)*. Later on, based on the structural prediction of the MA helix and on site directed mutagenesis, it was shown that putative salt bridges could be more important than the actual presence of the charge *(Kozuska et al., 2014)*. This was demonstrated by a study where acid residues E414, E418 and D425 were mutated to their amide counterpart (QQN) to break salt bridges made with the other residues. The conductivity of this triple mutant was comparable to that of the initial RRR to QDA mutation and moreover the single mutant E418Q also presented a big conductance. General suggestion that the charged residues in the intracellular domain might play stabilising roles being involved in salt bridges was further supported by mutagenesis of the other charged residues preceding E418.

The RRR residues line the portals of the cytoplasmic vestibule and it was under question whether they determine only the conductance of the receptor or if they also participate in size selectivity towards the permeant ion. By analysis of the ion selectivity of the 5-HT3R mutants missing the M3-M4 loop compared to the selectivity of the WT receptor, it was shown that the RRR triplet is not essential for ion selection *(McKinnon et al., 2011)*.

The channel selectivity filter was determined based on the mutagenesis of the 5-HT3R residues analogous to those influencing the ion selectivity properties of the other Cys-loop receptors *(Gunthorpe and Lummis, 2001)*. The alignment of anion-selective and cation-selective Cys-loop receptors revealed the conserved presence of positively or negatively charged residues corresponding to the anion- and cation-selectivity, respectively. These rings are located on the extracellular and intracellular ends of the pore. Based on mutagenesis studies results, the lower ring formed by E250 on the intracellular side seems to be the main determinant of the 5-HT3R selectivity *(Thompson and Lummis, 2003)*. The 5-HT3R is relatively

promiscuous with regard to its selectivity. The selectivity among different cations was predicted based on the property to reverse near 0 mV, suggesting similar permeabilities for Na^+ and K^+ cations. The 5-HT3R discriminates between the small monovalent ions (Cs^+, K^+, $Li^+ < Na^+ = Rb^+$) only weakly *(Yang, 1990)*. Moreover, even some of the organic cations (e.g., ammonium and methylamine) are able to pass through the channel and unsurprisingly their permeability decreases with their increasing size *(Yang, 1990)*. The divalent cations (Ca^{2+}, Ba^{2+}, Mg^{2+}) also pass through the selectivity filter of the 5-HT3R. The calcium permeability of the receptor varies between the splice variants of the 5-HT3R A subunit, with the shorter variant enabling higher permeability *(Hargreaves et al., 1994)*. Moreover, the presence of divalent cations modulates the amplitude of the signal and also the duration of the response to the agonist *(Thompson and Lummis, 2009)*. The absence of calcium cations increases both of these factors. The Ca^{2+} inward flux into presynaptic terminals results in exocytosis *(Rondé and Nichols, 1998)*. As the presynaptic 5-HT3 receptors were shown to mediate GABA release in proportion to the Ca^{2+} concentration *(Turner et al., 2004)*, it has been speculated that Ca^{2+} permeability was more relevant to presynaptic physiology than to postsynaptic Ca^{2+} uptake.

1.4.2 Pharmacology

The 5-HT3Rs are proposed to play a role in the development of multiple diseases and psychological disorders *(Fakhfouri et al., 2019; Gupta et al., 2016)*. They are the main pharmacological target of drugs marketed for irritable bowel syndrome *(Tyers and Freeman, 1992)* and chemotherapy induced nausea and vomiting (CINV), as well as for post-operative nausea and vomiting *(Humphrey et al., 1999)*. In both of the aforementioned cases the active drugs are antagonists from the ¨setron¨ family (Fig. 7).

CINV is one of the most dreaded effects of chemotherapy *(Coates et al., 1983)*. It causes discomfort and negatively influences adherence to the chemotherapy treatment regime *(Bloechl-Daum et al., 2006)*. Since their discovery in the 1980s, antagonists of 5-HT3R are used and have been further developed as the most potent drugs for the treatment of CINV *(Sanger and Andrews, 2018)*. Currently, together with the NK1 inhibitors and with steroids, they form the three drug CINV treatment regimen *(Gilmore et al., 2018)*. There is a tendency to create universal guidelines for CINV prophylaxis but all attempts are complicated by a lack of understanding of the underlying pathophysiology and by the subjectivity of nausea assessment by patients.

Some of the drugs targeting the 5-HT3R such as ondansetron and clozapine have

been shown to have a positive effect on schizophrenic symptoms *(Meltzer et al., 2003)*. Furthermore, mutations in the 5-HT3R were observed in the genomes of patients with bipolar disease and schizophrenia but their impact on pathology has not been directly proven *(Niesler et al., 2001)*. Although further clinical tests are needed it has been concluded that the 5-HT3R antagonists are involved in the treatment of the depression *(Hewlett et al., 2003)*. Indeed, the recently marketed Vortioxetine antidepressant, in addition to its known effects on the serotonin transporter and the 5-HT1 receptors, also potently inhibits the 5-HT3R. However, the role of 5-HT3R inhibition in the clinical effect of Vortioxetine remains undetermined, even if the marketing of the drug insists on its "multimodality" *(Katona and Katona, 2014)*. Substance abuse and addiction studied in mice determined that the 5-HT3R is involved in self-administration of ethanol and for cocaine sensitisation *(Hodge et al., 2004, 2008)*. Importantly, self-administration of ethanol was also shown to be reduced by 5-HT3R antagonists in humans *(Johnson et al., 2002)*. The 5-HT3R also reacts to anaesthetics from different families including inhalation and intravenous anaesthetics, as well as local anaesthetics *(Barann et al., 2008; Stevens et al., 2005; Urban et al., 2006)*.

Amongst natural compounds acting on the 5-HT3R, morphine (the opioid analgesic from unripe poppy seeds) *(Gaddum and Picarelli, 1957)*, alpha-thujone (the psychotropic component of absinthe from wormwood) *(Deiml et al., 2004)*, and the gingerols and shogaols (the antiemetic compound from the ginger extracts) *(Abdel-Aziz et al., 2006)* can be mentioned.

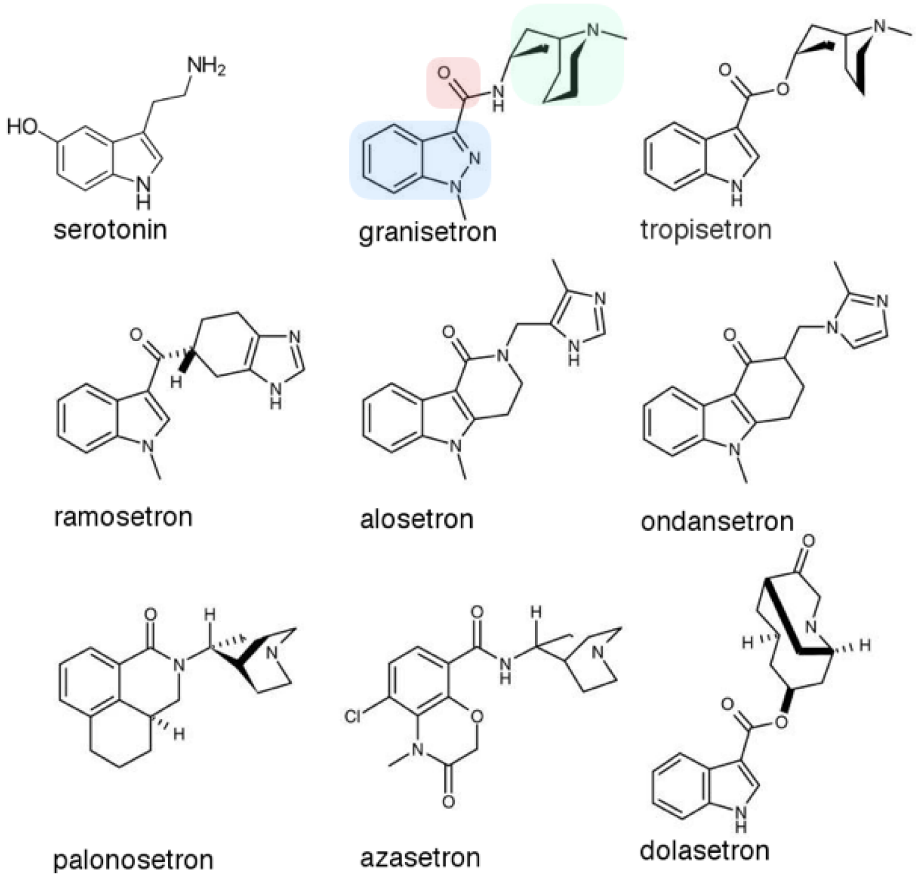

Figure 7 | The antagonists from the setron family alongside the biological agonist serotonin.

Common features might be observed within the setron family. The aromatic heterocycle is highlighted in granisetron in blue, the carbonyl linker in red and the amine carrying cycle in green.

1.5 The 5-HT3R structure and its comparison to other known structures of Cys-loop receptors.

Efforts to elucidate the structure of the Cys-loop receptors began with the soluble acetylcholine binding protein, a marine snail protein homologous to the extracellular domain of the Cys-loop receptors. Its X-ray structure was solved in 2001 *(Brejc et al., 2001)* and unveiled the architecture of the extracellular domain of pLGIC and the organization of the orthosteric binding site. The first structure of a full length Cys-loop receptor was the cryo-electron microscopy (cryo-EM) structure of the heteromeric nicotinic acetylcholine receptor extracted from the *Torpedo marmorata* electric tissue *(Miyazawa et al., 2003; Unwin, 2005)*. It permitted to understand the receptor global architecture and provided a first structural framework to interpret the accumulated body of functional data on pLGIC. However the resolution remained limited. As a consequence, the register of the amino acid assignment of this structure was later shown

to be out by ~1 helix turn beginning with the M1/M2 loop when compared to newly published structures *(Hibbs and Gouaux, 2011)*. The first full-length structures to be solved by crystallography were of that of pentameric ligand-gated ion channels from prokaryotic organisms, ELIC from *Erwinia chrysanthemi (Hilf and Dutzler, 2008)* and GLIC from *Gloeobacter violaceus (Bocquet et al., 2008)*, hypothesised to be in the closed and the open conformation, respectively. Interestingly, neither ELIC nor GLIC possess intracellular domains: they lack the MX helix, the long unstructured loop, and the MA cytoplasmic helix. Thus, their subunits are composed only of the ECD and the 4 membrane helices connected by shorter loops. These structures were followed by the first eukaryotic structure of the *Caenorhabditis elegans* glutamate-gated chloride channel α, the GluCl channel, where the natural intracellular domain was replaced by the short linker M3-Ala-Gly-Thr-M4 *(Hibbs and Gouaux, 2011)*. In that case, stabilising antigen-binding fragments (Fab) proteins were used as crystallization chaperones to enhance the pentamer stability and also to help with crystal contacts. In 2014, the structures of the first two mammalian Cys-loop receptors were obtained by X-ray crystallography. These were those of the homomeric GABAA receptor composed of β3 subunits, and with its intracellular domain removed (replaced by the SQPARAA amino acid sequence) *(Miller and Aricescu, 2014)* and of the m5-HT3RA, which included the structured parts of the intracellular domain, the MX and the MA helices *(Hassaine et al., 2014)*. The latter was obtained in the presence of stabilising nanobodies. The GABAA receptor was supposed to be in the desensitised state and the 5-HT3R was speculated to be in the closed conformation based on the fact that the stabilising nanobody used in the structure is actually acting as an antagonist. Structures of the homomeric glycine receptor in the open, desensitised and closed conformations, obtained by cryo-electron microscopy, enabled direct comparison of the different conformational states *(Du et al., 2015)*. The constructs used for that study lacked the intracellular domain, which was replaced by M3-Ala-Gly-Thr-M4. At the same time the X-ray structure of the GlyRα3 was solved, with a resolution up to 3 Å, in the presence of the antagonist strychnine *(Huang et al., 2015)*. As in most cases, its intracellular domain was absent and the receptor is supposed to be in the antagonist-bound closed conformation. The only known heteromeric structures to date belong to the nAChR and GABAA family. Thirteen years after the low resolution EM structure of the *Torpedo nAChR*, the X-ray structure of the recombinant 2α:3β nAChR α4β2 was solved. The structure was obtained in the presence of nicotine bound to the binding site and is believed to be in the desensitised conformation.

After the crystallographic structure of 2α:3β nAChR α4β2, the stoichiometrically distinct nAChR α4β2 3α:2β was solved by cryo-EM *(Walsh et al., 2018)*. This enabled a

direct comparison between different assemblies and elucidated the principles of the subunit packing mechanism. The cryo-EM structure of the 5-HT3R without ligand *(Basak et al., 2018a)* revealed only minor differences between the potentially inhibited receptor solved in the presence of VHHs and the apo structure. Two conformationally distinct structures of the GABAA α1β2γ2 receptor *(Zhu et al., 2018)* and one additional structure of GABAA α1β1γ2 *(Phulera et al., 2018)* were recently solved, all by cryo-EM, showing the organisation of consecutive subunits, revealing the ECD vestibule glycosylations and more importantly illuminating the mode of ligand binding. Interestingly, GABAA α1β1γ2 structure revealed the asymmetry of the TMD subunit organisation around the pore axis and the GABAA α1β2γ2 structure showed the complete gamma subunit collapse into the TMD pore. In contrast to those two structures, the GABAA α1β3γ2 structures *(Laverty et al., 2019; Masiulis et al., 2019)*, solved by cryo-EM as well, presented the symmetrical organisation corresponding to that of the homopentameric GABAA β3 solved by X-ray crystallography. The potential source of dissimilarities might be a use of detergents and engineered constructs (deletion of ICD) in the case of distorted structures in contrast to the use of nanodiscs and full length construct for the symetricaly organised GABAA α1β3γ2 structures. The X-ray structure of the chimeric ELIC(ECD) - GABAA α1(TMD) indicates the differences between the apo and alphaxalone-bound chimeric receptor which is supposed to be desensitised *(Chen et al., 2018)*. Finally our recent structural study of the 5-HT3RA receptor mapped the changes that occur during the activation of the receptor by serotonin. These conclusions are supported by the comparison of the apo *(Basak et al., 2018a)*, two open pore structures , two agonist-bound closed pore states *(Basak et al., 2018b; Polovinkin et al., 2018)* and one pre-active state *(Polovinkin et al., 2018)*. A simplified overview of the pLGIC structures solved up to 2018 is summarised in Fig. 8 and for the sake of completeness table with structures of pLGIC can be found in supplementary data Tab. 1.

The non-physiological membrane domain environment (mostly detergent until last year, and now also nanodiscs) together with the experimental conditions (crystal packing or freezing) often raises questions about the correlation of structures with physiological conformations existing in the cell membrane. Moreover, regarding the Cys-loop receptors, the functional assignments of the captured conformational states might be strenuous. Still the comparison of multiple steady-state structures of the same protein is probably the best tool we have at the moment to understand the molecular mechanism of operation. As with GlyR, more and more receptors are being solved in different conformations and stoichiometries, permitting us to better understand this family.

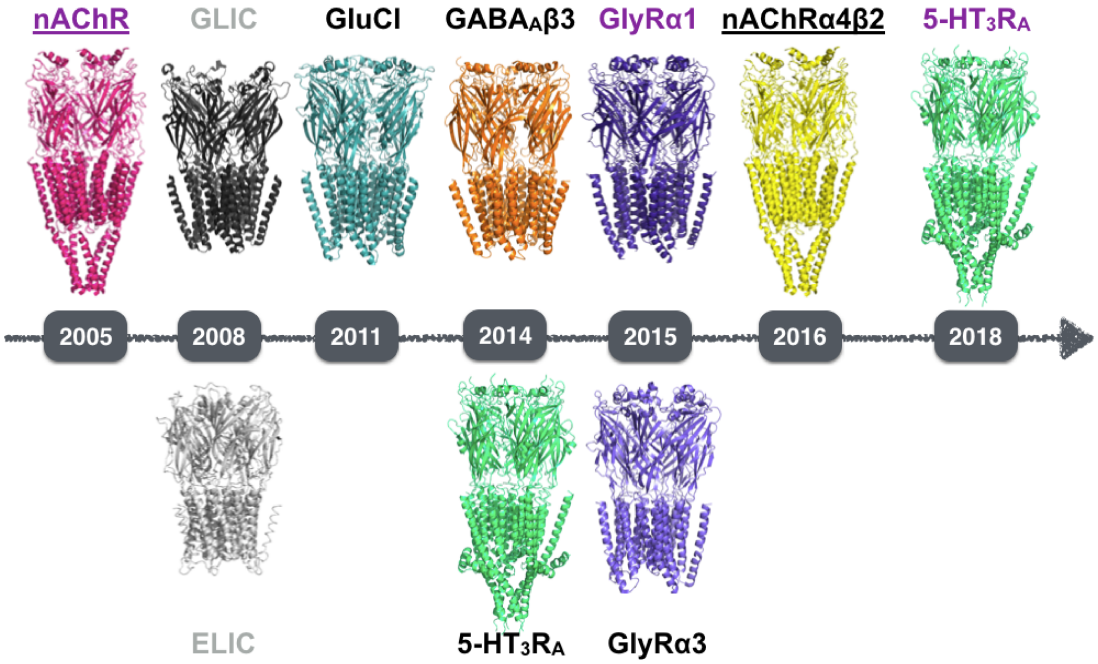

Figure 8 | A chronological overview showing the first discovery of structures of representatives from each pLGIC family potentially by different methods up to the year 2018.

Receptors are graphically divided into different groups by the font of the receptor names. All of the receptors are eukaryotic except for the grey-labeled receptors, which are prokaryotic. The majority of the structures were solved by X-ray crystallography and only violet-labeled structures were solved by cryo-EM. The heteromeric structures are underlined. Together with the expanding use of the cryo-EM method in the pLGIC field the number of structures solved during last year has significantly grown.

To complete the panorama of the structural knowledge the recent structures together with the mutated receptors, chimeric receptors and receptors in different conformational states are listed in the supplementary data table 1.

1.5.1 The overall structure

The 5-HT3R is composed of five subunits arranged in a pseudo-symmetrical manner around the axis formed by the ion permeation pathway. The ECDs are formed by β sheets forming a β-sandwich. Each β-sandwich overlaps with the consecutive one on the outer side of the receptor in a counter-clockwise manner. On the interface of two consecutive ECDs the overlap of the main subunit, the (+) side of the binding pocket, and the complementary subunit, the (-) side of the binding site, create the orthosteric binding site for the neurotransmitter (Fig. 9). The ECDs form multiple contacts with the membrane helices through the loops, which allows signal to be propagated from the bound neurotransmitter to the membrane portion of the receptor (Fig. 10). The membrane helices are organised in concentric rings. The innermost ring is formed by the M2 helices of each subunit which line the pore. These are enclosed by the middle

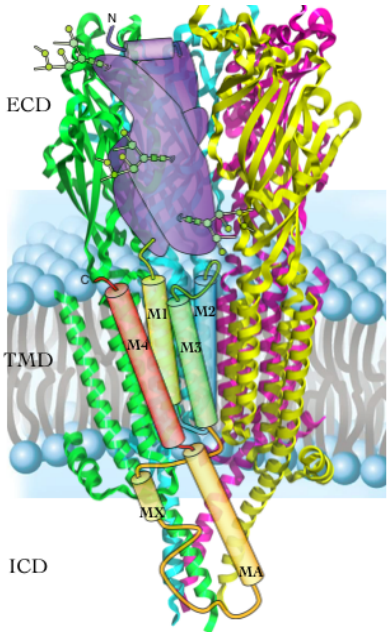

ring, composed of the M1 and M3 helices, and the M4 helices form the peripheral ring (Fig. 11). The position of the M4 helix provides it with a large surface with which to interact with the lipid environment. The MX helices are positioned at the outer side of the M4 helices, reminiscent of clamps that may keep the entire membrane portion together and may stabilize the M4 position. There is no structural information about the unstructured part of the M3-M4 loop. The continuation of the M4 helices protruding into the cytoplasm, the MA helices, are slightly twisted counter-clockwise relative to the ion permeation axis. The M4 ends at the extracellular side, determining the topology of the protein whereby both C- and N- termini are located outside of the cell.

1.5.2 Detailed structural features

1.5.2.1 Extracellular domain - neurotransmitter binding site

For the Cys-loop receptors, the neurotransmitter binding site was elucidated by the use of the homology, comparing the Cys-loop receptor ECD to the structure of the AChBP *(Brejc et al., 2001)*. The ECD β-sandwiches are formed by the 10 β-strands divided into two main β-sheets. The binding site is formed by "loops" A, B and C from the principal subunit and "loops" D, E, F and G from the complementary subunits *(Nys et al., 2013)* (Fig. 9A). It is worth noting that the term "loops" is not strictly correct, because not all of these elements are actually loops. Structurally, only the following elements corresponds to loops: loop A connecting β-strand 4 to β-strand 5 (β4-β5 loop), loop C (β9-β10 loop) and loop F (β8-β9 loop). ¨Loops¨ E, D and G are actually portions of β-strands. Residues that participate in ligand binding in the orthosteric binding site come from "loop" B and are located partially on the β7 strand and partially on the β7-β8 loop. Some of the features of this binding site are well conserved among the Cys-loop receptors, even though their ligands vary. There is a conserved "aromatic box" within the majority of the Cys-loop receptors, located on the interface of some of these conserved elements *(Lester, 2004)*. In the 5-HT3R, the "aromatic box" is defined by

aromatic residues W156, Y207, W63, Y126 and F199 from loops B, C, D, E and F, respectively. Some of the binding site residues are conserved across all of the different types of Cys-loop receptors as seen on the sequence alignment in (Fig. 9B). The observation that the loop C is generally more open in the case of the antagonist-bound/closed or resting/closed state, and moves closer to the binding site if an agonist is present and induces the agonist-bound/open conformation or the agonist-bound desensitised/pore closed state, was extrapolated from AChBP to pLGIC. Thus the loop C was commonly used to be a criterion for the determination of the overall receptor functional state. The ligand-bound structures of the pLGIC generally manifest described C loop movement, but it might be very subtle and allows rather comparison of two structures than the interpretation of the structural state by itself. The subunit-subunit rearrangement is a better guideline to the functional state determination *(Hassaine et al., 2014)*. The structure of the 5-HT_3R_A was solved using the VHH15 nanobody, which binds to the subunit interface from the outside of the binding pocket and actually grasps loop C, bending it towards the outside.

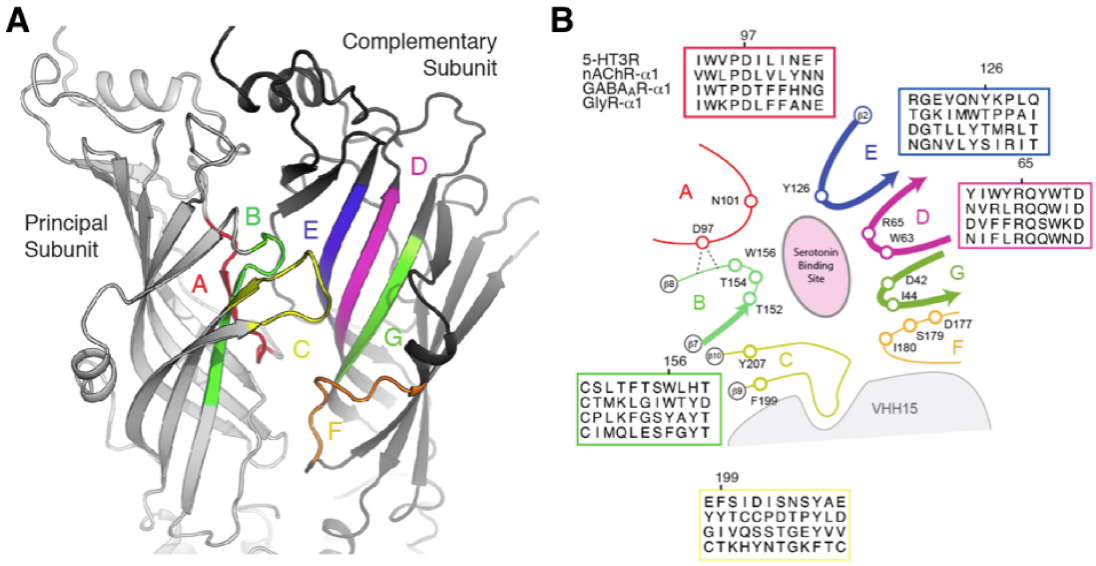

Figure 9 | Structural and sequential features defining the binding site located between two consecutive subunits.

A) The binding site is defined by loops A, B and C of the principal subunit and loops E, D, G and F from the complementary subunit. **B)** In the majority of Cys-loop receptors there is a so-called "aromatic box", conserved and consisting of aromatic residues corresponding to W156, Y207, W63, Y126 and F199 in 5-HT3R. Taken from *Hassaine et al. (2014)*.

Insights into ligand binding to the 5-HT3R were obtained by comparison with the AChBP solved in the presence of ligands. Mutagenesis of the AChBP binding site to

mimic the 5-HT3R binding site led to the creation of the model protein 5-HTBP, which has the binding properties of the 5-HT3R *(Kesters et al., 2012; Price et al., 2016)*.

Based on functional studies of the 5-HT3R binding site mutants, the impact of different amino acids on ligand binding was proposed *(Beene et al., 2002; Spier and Lummis, 2000; Thompson et al., 2005)*. The majority of the binding studies were done with antagonists of the receptor from the "setron" family, mostly tropisetron and granisetron. The π electrons from the aromatic residues are supposed to interact with the cation provided by the positively-charged ring-embedded nitrogen what was hypothesised for both, agonists *(Spier and Lummis, 2000)* and "setron" antagonists. The orientation of the ligands within the binding site was speculative and controversial. Yan and White *(Yan and White, 2005)* proposed that the granisetron orients its bicyclic ring to interact with residue W63. Mutagenesis to introduce unnatural amino acids at this position suggested a different interaction mode between granisetron and the W63 position, showing that the cation-π interaction might actually occur via W156 *(Duffy et al., 2012)*. Recently, the binding properties of granisetron and tropisetron, which are closely related, were discussed. Even though the structures of the AChBP solved in the presence of these ligands implies they are orientated in the same way, the extensive mutagenesis of the 5-HT3R binding site and the binding studies of the two agonists implied different properties, suggesting that these two ligands might interact differentially with the 5-HT3R binding site *(Ruepp et al., 2017)*. Moreover, the binding orientations based on functional studies and modelling, were proposed by the same study.

A very recent structures of the tropisetron bound (see the results presented in section 5.2.2) and granisetron bound m5-HT3R *(Basak et al., 2019)* confirmed the orientation of the ligand in the binding pocket; the amin-carrying bicyclic ring points outwards and the indazole ring mediates the cation-π interaction deeper in the binding pocket.

1.5.2.2 ECD-TMD interface - binding signal transduction

pLGICs can possess several orthosteric binding sites (5 in the case of the 5-HT3RA) where the binding of a ligand can trigger the channel opening. Conformational changes are often described either as of a ligand-induced selection from the pre-existing conformational states (Monod-Wyman-Changeux model, MWC) or as ligand-induced sequential conformational changes (induced fit model, IF). According to the MWC model all subunits of the existing populations of receptor are in the same conformation

and the switch of equilibrium induces the concerted change of all the subunits at once. In contrast, IF model predicts that the binding of ligand changes the conformation of influenced subunits, what increases the binding affinity of the following ligand up to the complete rearrangement of all subunits. In a way the MWC model describes the conformational changes rather at the quaternary structure level and the IF model rather at the tertiary structure. The following paragraphs aim to point to the structurally important and interacting elements (residues, secondary, tertiary and quaternary structures) regardless the ligand-induced cooperativity scheme they follow.

Considering the available structural knowledge of the Cys-loop receptors, a relevant description of the mechanism of signal transduction probably comes from a comparison of the multiple conformations of the GlyR solved by EM *(Du et al., 2015).* This series of structures permits a direct comparison of the interface between the ECD and the TMD among different conformational states within one receptor type. Starting with the binding of a ligand in the binding pocket, the C-loop moves outwards when an antagonist is bound or moves inward (towards the binding site) when an agonist is present. When we consider only the principal (+) subunit , the binding signal might be transduced through movements of the β9 and β10 strands, thus influencing the conformation of loop β8-β9 (F loop) and of the β10/pre-M1 loop region (Fig. 10) at the ECD-TMD interface.

Conformational changes affecting the M1 helix can directly influence the position of the M2 helix. Moreover, the β10/pre-M1 loop region is in contact with the Cys-loop, which in turn interacts with the β1-β2 loop and, most importantly,with the M2-M3 loop. The M2-M3 loop can then directly influence the conformation of the M2 helix. This is also the place where two neighboring subunits meet each other at the ECD-TMD interface. The M2-M3 loop from the (+) subunit interacts with the β8-β9 loop (F loop) and the β10/pre-M1 loop from the neighbouring (-) subuni. In the article reporting the GlyR structures, a direct link between M2 helix rotation and the position of the ECD was described in detail, highlighting residues that play a role in this process *(Du et al., 2015)*. The tip of the Cys-loop, which plays the central role in the signal transduction, is very well conserved among the family. The 142-F/YPXD-145 motif in particular is found in all the receptors of the family. Another conserved residue is the arginine located at position 218 in the m5-HT3RA. R218, reported to be responsible for changes in gating properties after ligand binding *(Hu et al., 2003)* is the key interactor with multiple elements on the ECD-TMD interface. It is sandwiched from the top and bottom by the two aromatic residues W187 of the β8-β9 loop (F loop) and F142 of the Cys-loop. Moreover, R218 is enclosed by multiple negatively charged residues, specifically by D145 of the Cys-loop from one side, by E186 of the β8-β9 loop (F loop)

from the other side, and by E53 located on the β1-β2 loop from the front *(Hassaine et al., 2014)*. Unfortunately, the tip of the M2-M3 loop is not resolved in the 5-HT3R structure and thus hinders the assignment of the interactions of the 4 missing TAIG residues. There is actually an alanine insertion in the mouse construct used in structural studies from our laboratory, mimicking the human M2-M3 loop.

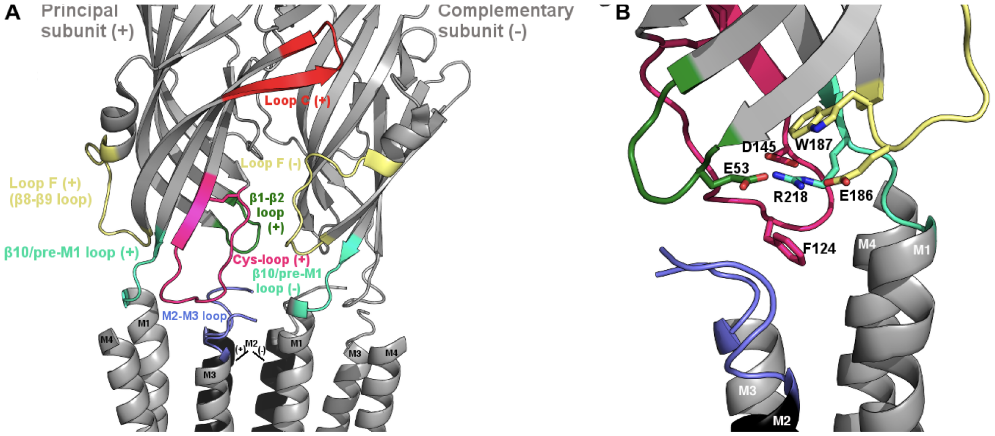

Figure 10 | Key structural features of signal transduction from the binding site to the membrane domain.

A) Upon agonist binding to the binding site the signal is transduced through the ECD to the membrane domain where it alters the M2 position and influence the opening of the pore. The M2 position is mainly affected by two factors: i) movement of the β8-β9 loop (F loop) and the β10/pre-M1 loop region which induces an M1 position change, causing the move of the M2, and ii) the M2-M3 loop receiving the incoming binding signal from the movement of Cys-loop, which in turn results in the movement of M2. **B)** The arginine at position 218, located on the β10/pre-M1 loop, is the mediator of the interaction with multiple structurally important elements. It is in between of residues W187 and E186 from loop F, and between residues D145 and F124 from the Cys-loop. The β1-β2 loop interacts with R218 through E53.

1.5.2.3 Transmembrane domain - ion pathway through the membrane

The actual pore of the pentameric ligand-gated receptors which is in contact with the passing ions is formed only by the M2 helices. The M2 helices are enclosed by the ring of M1 and M3 helices and are not in direct contact with the M4 helices on the periphery (Fig. 11).

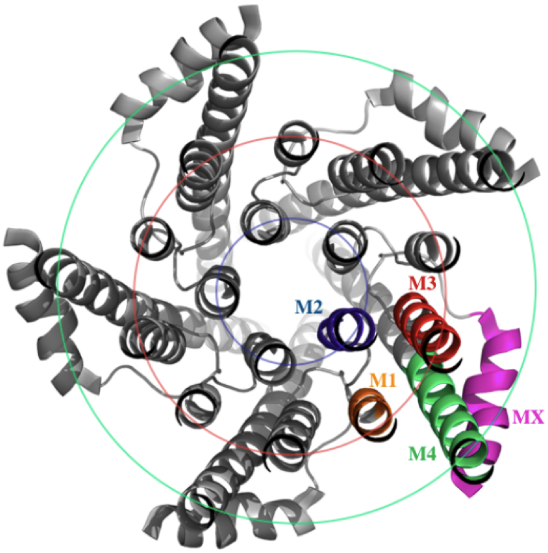

Figure 11 | The structural arrangement of the membrane helices and the pore forming M2 helices.

The concentric organisation of the membrane helices. The outermost ring is formed by M4 helices, M3 and M1 form the middle layer and the innermost circle is the actual pore of the channel made by the M2 helices.

The M2s are oriented more or less perpendicularly to the membrane plane and the pore is defined by the amino acid side chain residues pointing inside to create constrictions parallel to the membrane plane. For the purpose of simplification and better orientation the M2 helix residues of the first nAChR structure to be solved were assigned new numbers, starting with the lowest membrane residue carrying the number 0', up to the residue closest to the extracellular part of the membrane having the number 20' *(Miyazawa et al., 2003)*. All structures solved later respect this numbering system and define the 0' residue based on sequence alignment. If some residues, shown to be before the 0' residue, are still within the membrane, they are numbered with negative numbers starting from -1' and going from the 0' residue lower along the M2 helix.

The structures solved to date indicate the existence of multiple constrictions determining the ion pathway. Generally there are two main constriction sites on the M2 helices, one in the middle and the second closer to the intracellular side. The middle position is defined by the highly conserved leucine at the 9' position *(Alqazzaz et al., 2011)*. This residue is a geometrical determinant of ion permeability in closed states (Fig. 12) and together with the V13' and I16' residues forms the hydrophobic gates *(Miyazawa et al., 2003)*. The V13'S mutation lead to the gain-of-function phenotypes *(Dang et al., 2000)*. The L9' mutations to Phe, Tyr or Ala cause the slower desensitisation in contrast to the Thr mutation *(Yakel et al., 1993)*. Its position differs among the different conformational states of receptors. Even though the relative

position of the M2 helices within the receptors in the antagonist-bound/closed and resting/closed conformation vary, the L9' remains the main restriction determinant in all of these structures (5-HT3R, strychnine-GlyRα1 and apo-GluCl). The ion pathway at the P9' position is blocked by the too small radius (~1.4 Å) in the closed GlyRα1 but is widely open (4-5 Å) in the open and desensitised state of the same receptor. In the 5-HT3RA serotonin-bound structure the M2 rotates by 13° in comparison to the apo structure, causing the rotation of L9' away from the pore *(Basak et al., 2018b)*. Additionally, a tilt was observed at the S2' position, widening the vestibule at the intracellular end.

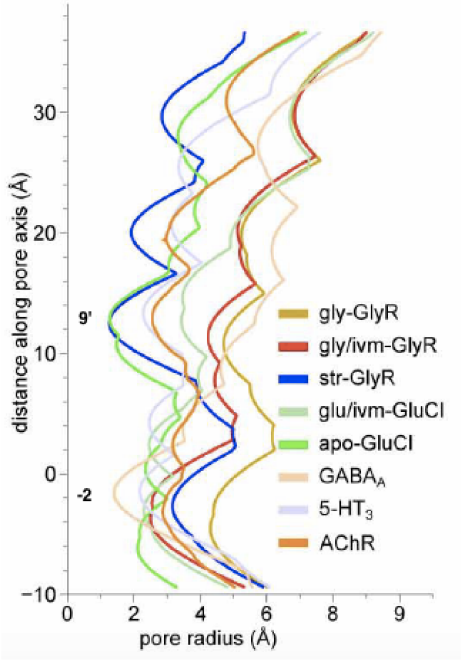

Figure 12 | The general comparison of the pore radii forming residues of M2 helix in different pLGIC.

The pore radii as a function of the distance along the pore axis with the 0 set to the 0' Arg of the GlyR shows the 9' and/or the -2' to be the main geometrical restriction point/s of the ion pathway. The comparison of the open pore agonist-bound, open pore agonist/modulater-bound, antagonist-bound closed pore of the GlyRα1 top to bottom. Followed by apo, agonist-bound closed pore, nanoobody-bound closed pore and agonis-bound closed pore structures, top to bottom.

Adapted from *(Du et al., 2015)*.

In the apparently desensitised structures the L9' is not a pore size limiting residue. All the structures of desensitised receptors known to date present the smallest pore radius in the lower part of the M2. For the GlyRα1 in the closed state it is at the proline -2' position *(Du et al., 2015)*, for the nAChRα4β2 receptor, the channel is tightest at the E-2' position *(Morales-Perez et al., 2016),* and for GABAA at the A-2' position as well

(Miller and Aricescu, 2014) (Fig. 12). As mentioned above, these residues are responsible for the selectivity of the ion channels and thus the conserved residues at this position vary according to the channel permeability *(Thompson and Lummis, 2003)*. Anion-selective channels usually have uncharged amino acid residues here, and cation-selective channels contain mostly negatively charged glutamic acids at this position.

The X-ray structure of the 5-HT3RA was solved using stabilising nanobodies, which were shown to act as antagonists. The radius formed by the L9' residues is about 4.6 Å, a width that might be too tight for hydrated Na^+, which have a radius of about 4.7 Å. This agrees with the suggestion that the structure is in the closed conformation. Moreover, it is supported by the results of MD performed with the recently obtained structures *(Basak et al., 2018b)* (and our structures presented in the 5.2.2 section). It shows that prediction of the pore de-wetting by MD is a better indicator of the pore permeability rather than the measurement of geometrical constriction. Interestingly, the comparison of the backbone within the structure with the open channels (GLIC and open GluCl) suggests a closer resemblance to these open structures rather than to the closed ELIC and GLIC structures, which led to some speculation questioning if the channel is really closed. The side chain of E-1' was unfortunately not clearly defined in the electron density map and was modeled only as the most plausible rotamer, thus not allowing any further interpretation. The X-ray structure mostly agrees with the apo state receptor solved by cryo-EM, which supports the theory that the X-ray structure is of a closed state and as mentioned above, it is confirmed by the MD.

Different parts of the TMD were proposed to be a predominant location where allosteric modulators bind *(Sauguet et al., 2015)*. Those are amphipathic molecules including anesthetics, ivermectin, ethanol, as well as lipids/detergents *(Hibbs and Gouaux, 2011), (Basak et al., 2017), (Nury et al., 2011)*.

The presence of lipids is a very important factor influencing the functional properties of receptors, mediated by the transmembrane portion of the protein. First it was shown that nAChR solubilised by detergent maintains its ligand-binding capacity but does not allow ion flux *(Sobel et al., 1977)*, requiring the presence of lipids to help regain its natural functional properties *(Epstein and Racker, 1978)* (Fig. 13). Based on the composition of the membrane naturally surrounding nAChR, tests probing the effects of the addition of cholesterol and of phosphatidic acid (PA, negatively charged head group) were done *(Baenziger et al., 2000)*. Both of these lipids are able to maintain the coupling between the binding of a ligand and the conformation of the pore. In the presence of phosphatidylcholine lipids only, the nAChR enters a so-called "uncoupled" state that differs from the desensitised state and has lost the capacity to transduce signal

from the binding site to the pore *(daCosta et al., 2009)*. When the effect of lipids on the desensitisation process was further studied, the M4 helix, situated at the periphery of the membrane bundle and as such the perfect candidate for lipid interaction, was shown to play a role in this process, at least for nAChRs *(daCosta et al., 2013)*.

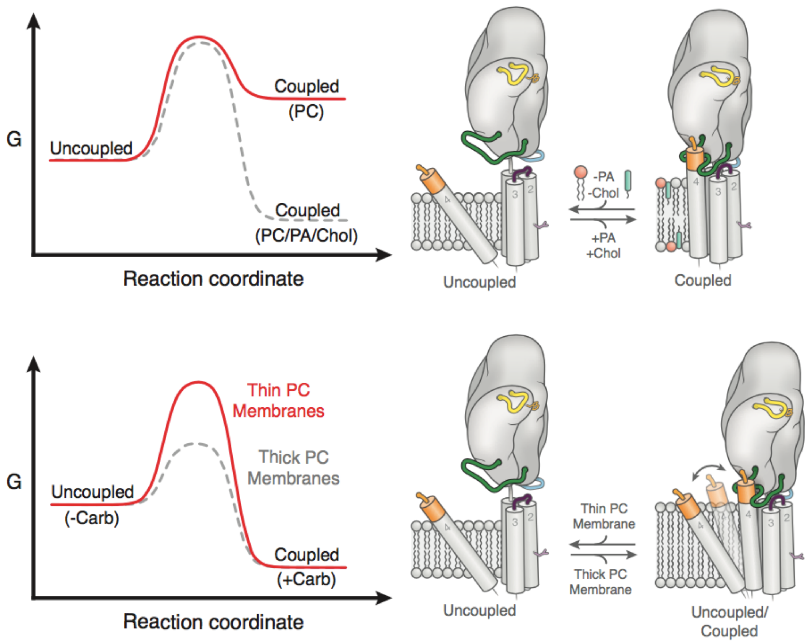

Figure 13 | The effect of membrane lipid composition on uncoupling of the nAchRs.

The proposed structural conformational differences between the coupled and uncoupled form of the nAchR shown on the single subunit model. The main factors influencing the proper functioning of receptors are the presence of anionic lipids and the thickness of the membrane (the thicker the better). Taken from *Baenziger et al. (2017)* .

Moreover, the GLIC receptor was shown to be sensitive to docosahexaenoic acid (DHA) that induces the desensitised conformation of the receptor *(Basak et al., 2017)*. DHA binds in between the M4 and M3 helices at the ECD-TMD level, inducing small changes in side chain residues of neighbouring amino acids (among them Phe260 from the M3 and Phe315 from the M4 helix). Another example of the TMD modulators are endogenous neurosteroids which interact with residues T305 (M3 of principal subunit) and Q241+W245 (M1 from consecutive subunit) *(Laverty et al., 2017)*.

1.5.2.4 The intracellular domain

Although the intracellular domain has been shown to play an important role in conductance determination, in trafficking, in determining life-time kinetics at the synapse and also in protein-protein interactions, structurally it is the least well defined element of the Cys-loop receptors. The prokaryotic homologues lack the intracellular domain completely and the majority of the structures of eukaryotic receptors were solved using mutants where the M3-M4 loop was replaced by short linkers. The M3-M4 loop comprises of the MX peripheral helix, in cation-selective pLGIC, on the intracellular side of the membrane, followed by an unstructured loop and by the MA helix, which becomes the M4 helix at the membrane border (Fig. 5). The only partial structural information available about the M3-M4 region comes from the *Torpedo* nAChR structure *(Unwin, 2005)* and from the 5-HT3RA structures *(Hassaine et al., 2014)* where a part of the unstructured domain, the post-M3 loop, and the MX and MA helices are resolved. For the nAChRα4β2 structure, the post-M3 loop and the MX helix were left in the expression construct *(Morales-Perez et al., 2016)*. However, the loop between the MX helix and the M4 helix is absent in this structure, showing potential flexibility of the unnatural linker. The post-M3 loop is resolved in the very recent GABAA structures but the existence of the MX in anion-selective pLGIC remain unproven because of the poor densities at this level *(Laverty et al., 2019; Masiulis et al., 2019)*. Interestingly, the importance of the length of the M3-M4 loop was studied in the 5-HT3R and it was shown that even a loop as short as 2 alanine residues is sufficient to obtain the functional receptor *(McKinnon et al., 2012)*. Varying the length of the alanine linker resulted in differentially active receptors, suggesting that it is not only the loop length that matters but also the secondary structure of the linker, which may influence proper receptor functioning and expression of the protein *(McKinnon et al., 2012)*.

Functional studies of the 5-HT3R have revealed the importance of the intracellular domain region, particularly that of the residues of the MA helices influencing the single-channel conductance of the receptor *(Kelley et al., 2003)*. The residues responsible for the difference in conductivity between the homo- (A subunit only) and heteropentamers (AB receptor) were determined to be R416, R420 and R424 (Fig. 14) as described in detail in the section 1.4.1.

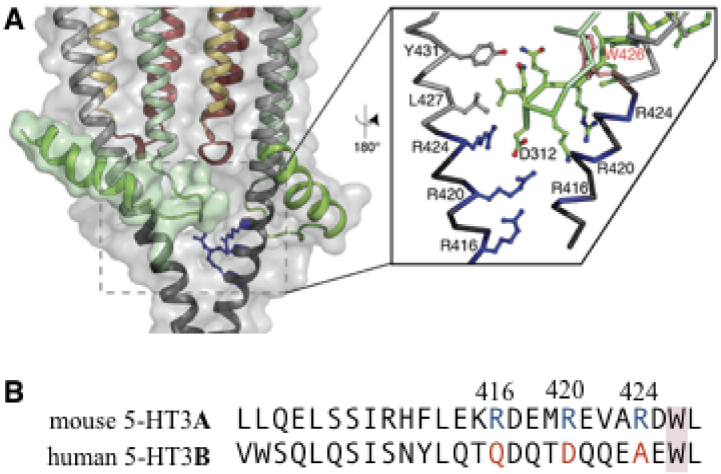

Figure 14 | The intracellular domain conductance-determining features.

A) The portals between two consecutive subunit's MA helices are occupied by the post M3 loop (surface depicted in green). A close-up view of the interaction between the MA and M4 helices and the post M3 loop. **B)** Sequence alignment of the MA region, showing the mouse 5-HT3A arginine triplet (in blue) and their counterparts in human 5-HT3B (red). The pink tryptophan at position 246 is conserved in cationic Cys-loop receptors and controls the position of the post M3 loop relative to the MA and M4 helices. Taken from *(Hassaine et al., 2014)* .

The pathway for ions through the ICD region is still to be elucidated and is speculated not to continue along the pore axis. Cations passing through the 5-HT3R are putatively thought to exit through the lateral portals at the level of the M3-MX loop below which the rings of positively charged arginines are located, whose function might be the repulsion of the positively charged ions or rather the formation of the salt bridges *(Kozuska et al., 2014)*. Further down the membrane the MA helices expose hydrophobic residues on the inside of the bundle and this region represents the tightest part of the whole pore vestibule with a minimal width of about 4.2 Å.

Regarding interacting partners of the 5-HT3R, the only known protein binding directly to the ICD is the resistance to inhibitors of cholinesterase type 3 protein (RIC3) *(Nishtala et al., 2016)*, known to be a protein chaperone. Its presence enables the maturation of multiple Cys-loop receptors *(Halevi et al., 2002, 2003; Lansdell, 2005; Walstab et al., 2010)*.

1.6 X-ray crystallography and cryo-electron microscopy of the membrane proteins

During the recent years we have seen a complete revolution in macromolecular structure determination. X-ray crystallography was, for a long time, the main tool

supplemented by NMR. However, methodologic development and technical advancement have made it possible to determine the first high-resolution structures of membrane proteins by single-particle cryo-electron microscopy in 2013 *(Cao et al., 2013; Liao et al., 2013)*. Since then the ratio of membrane protein structures solved by X-ray crystallography compared to cryo-EM has decreased (Fig. 15), with cryo-EM structures representing almost 37% of all membrane protein structures solved during the first four months of 2018 *(Cheng, 2018)*.

Without considering the common difficulties during the overexpression and purification of membrane proteins, both methods have their one specific bottleneck to surpass on the way to atomic resolution structures. X-ray crystallography requires crystal growth, which is generally a very challenging and complex procedure. Moreover, crystal growth of membrane proteins is complicated by the presence of detergent micelles. Solubilised membrane proteins might not be stable enough to form crystals, plus the presence of the micelle may limit the possibility of crystal contact formations. Multiple techniques aiming to solve this problem have been introduced. Among them are the use of antibodies/nanobodies to increase the potential effective surface for crystal contact formation and the insertion of proteins into the lipidic mesophases that may mimic more native-membrane-like conditions.

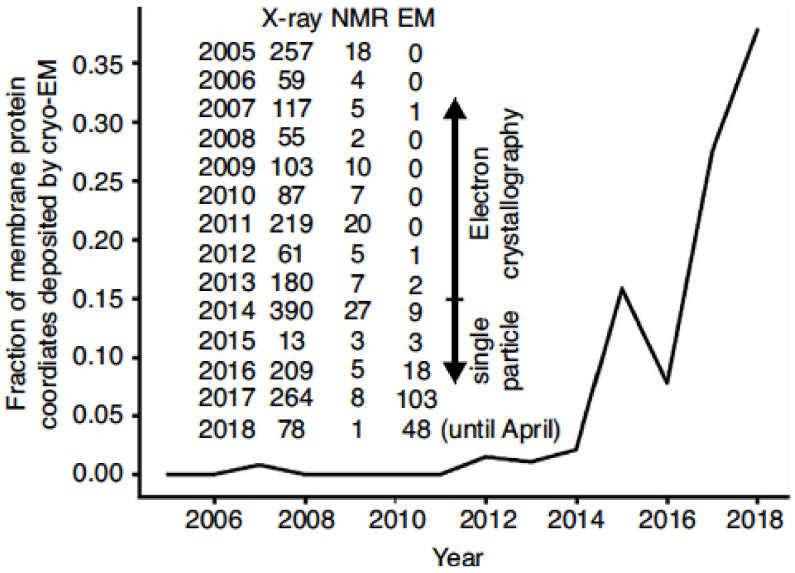

Figure 15 | Increased use of the cryo-EM method to solve structures of membrane proteins.

It is clear that the cryo-EM method became an increasingly competitive method for membrane protein studies. Taken from *Cheng (2018)*.

The cryo-EM method demands the same high-quality protein sample regarding its

purity, monodispersity and stability as X-ray crystallography. Crystals are no longer required but free micelles might pose a problem. They increase the noise and make data analysis more complicated (especially for small proteins analysed in combination with large micelle-forming detergents). To eliminate this problem, detergent was replaced by amphipol at least in the early cryo-EM studies of membrane proteins. Nowadays, the structures of membrane proteins are solved using not only amphipols *(Cao et al., 2013)* but also detergents *(Du et al., 2015)* and nanodiscs *(Efremov et al., 2014; Gao et al., 2016)*. Another obstacle is the need to have multiple orientations of protein particles in the holes of the frozen grid. Fluorinated detergents can be a helpful tool for membrane proteins *(Basak et al., 2017; Efremov et al., 2014)*, but one should keep in mind the fact that those detergents can potentially influence the membrane proteins as has been recently shown for the ryanodine receptor *(Willegems and Efremov, 2018).*

At the beginning of my PhD the only 5-HT3R structure available was the crystallographic structure of the m5-HT3RA receptor obtained using stabilising nanobodies. We wanted to solve other conformational states of the receptor using X-ray crystallography but the fast development of cryo-EM and the first high-resolution structures of membrane proteins solved via the cryo-EM method encouraged us to start using this method as well. Moreover, the m5-HT3R is an ideal candidate for cryo-EM due to its reasonable size (~250 kDa) and symmetry. The methodology of the X-ray crystallographic and cryo-EM structural studies together with the results and their discussion follows after the Objective of the thesis section.

2 Objective of the thesis

Due to their important role in neuronal signaling and their potential for pharmacological intervention, many receptors from the pLGIC superfamily are studied extensively, both functionally and structurally. Even though intensive efforts are being made, our knowledge of the signal transduction within the receptor remains limited. The best way to understand the mechanism of the receptor function is the co-interpretation of functional and structural data. Although this thesis focuses on structural studies, all the steps were planned taking into account the functional properties of the receptor known from the literature and complementary functional experiments were carried when needed.

As a follow up of the already described crystallographic structure of the 5-HT3RA receptor solved up to a resolution of 3.5 Å, the aim of my thesis was to try to obtain the structure(s) of an other state(s) and/or potentially obtain a structure with a better resolution, which would allow better structure-function interpretation. In the initial stages, the crystallographic approach was prefered; we quickly realized that the rapidly developing cryo-electron microscopy technique was to become the best tool for the structural studies of our target. Thus, the main goals of my thesis were:

I) Crystallography:

Use of nanobodies, which were shown to stabilise the receptor and help to create the crystal contacts, for co-crystallisation with the receptor using a classical vapour diffusion method to obtain the receptor locked in (an) other conformation(s).

Use of the lipidic cubic phase to obtain a better resolution structure of the 5-HT3RA.

Co-crystallisation of the receptor with drugs known to improve its stability to obtain better resolution or block the receptor in the open state.

II) Cryo-EM:

To obtain the closed conformation of the receptor as a confirmation of / comparison to the existing crystallographic structure and potentially obtain a structure of the desensitised and/or open state of the receptor.

3 The m5-HT3R isolation, purification and treatment

3.1 The m-5HT3R preparation - materials and methods

3.1.1 DNA construct(s)

Even if I have generated a variety of constructs during my PhD (including 5-HT3 receptor constructs for expression in *Leishmania tarentolae* cells, α4β2 constructs fused with GFP), most of the work described here was performed with a single construct encoding for the full-length homomeric receptor. It originates from previous work on the homomeric 5-HT3RA *(Hassaine et al., 2013)* .

The DNA construct for the mouse 5-HT3RA is in a pcDNA5/TO vector, enabling transient transfection of mammalian cells (typically 293F cells), generation of stable inducible cell lines in HEK-Trex cells, and injection into *Xenopus laevis* oocytes for TEVC functional assays. The insert is composed of a signal sequence, four consecutive Strep tags for purification, a TEV cleavage site and the mature 5-HT3RA sequence (depicted in the Extended Data Figure 1 of our paper *(Polovinkin et al., 2018)*).

3.1.2 Cell culture

The adherent, stable, inducible, cell-line HEK 293 5-HT3RA receptor originates from previous work on the homomeric 5-HT3RA receptor *(Hassaine et al., 2013)*. This cell line expresses constitutively the tetracycline repressor, preventing the expression of the target protein in the absence of tetracycline, and it also bears copies of the gene of interest. This cell line was adapted to be used not only for roller bottle expression, which is a tedious and manpower-heavy technique, but also for expression in suspension cultures.

For this purpose we used the adherent stable cell line HEK 293 5-HT3RA. We detached the cells from an 85% confluent 25 mL flask (Dutscher) with 5 mL PBS (Gibco) by gently pipetting up and down and we transferred 1 mL of the cell suspension into a 100 mL Erlenmeyer tube containing 10 mL of FreeStyle media (Gibco) supplemented with 10% of newborn calf serum (Corning). The serum concentration was halved every 3rd day during the passaging of the cells. Cells were plated to the density of 0.8 million cells/mL. At every passage, the amount of antibiotics was increased in a stepwise manner up to the final concentration of 5 μg/mL of Blasticidin and 100 μg/mL of Hygromycin B. Cells were grown while shaking in an orbital shaker at 37 °C, 5%

CO_2 and 90 rpm.

Typically, expression was induced by adding 4 mg/L of tetracycline to batches of 2 L of cultures at 2.10^6 cells/mL. The day after induction 4 mM valproic acid was added. Cells were harvested 48-72 h after induction.

3.1.3 Isolation of the 5-HT3RA

I have optimised the purification protocol of the receptor described in *(Hassaine et al., 2014)* and only the final version is described in the following sections.

3.1.3.1 Membrane preparation

To avoid contamination by the cytosol debris, I performed a membrane preparation step prior to the solubilisation step.

The collected cells were resuspended in resuspension buffer (10 mM HEPES pH 7.4, 1 mM EDTA and the inhibitor mix CLAPA (1µg/ml Chymostatin,1µg/ml Pepstatin, 1 µg/ml Leupeptin, 1 µg/ml Antipain and 4µg/ml of Aprotinin)) using 10 mL of buffer per 1 g of cells. Cells were kept on ice and lysed using the T25 Ultra Turrax homogeniser by five consecutive 30 s steps with increasing rotation of the homogeniser followed by a 1 min homogenisation at maximal speed. A low speed centrifugation was performed to remove unbroken cells (4000 x g, 20 min, 4 °C). The low-speed supernatant was further spun down using ultracentrifugation (120 000 x g, 1 h, 4 °C). The supernatant was decanted and the pellets containing the membranes were stored at -80 °C.

3.1.3.2 Solubilisation

Membrane proteins contain hydrophobic parts that are immersed in cellular membranes. To extract this hydrophobic moiety from the membrane and keep it intact and soluble in an aqueous solution, we use amphipathic molecules. These molecules consist of hydrophobic regions which are in contact with the transmembrane hydrophobic part of the protein and of hydrophilic polar group/s which is/are oriented into the solution. The most commonly used surfactants are detergents, which are able to extract the protein from the membrane and maintain it in solution, and amphipols,

which are not suitable for the extraction but work well for protein stabilisation in solution *(Seddon et al., 2004)*. Detergents are composed of a hydrophobic carbon tail and a polar head. Each detergent has specific properties regarding its harshness, its capability to extract the protein out of the membrane, the level of the native membrane lipids that it is able to remove from around the extracted protein, and its ability to form micelles (the self assembly of single detergent molecules into a supramolecular structure). An important property of a given detergent is its critical micellar concentration (CMC: the concentration border, which once exceeded initiates and favours the formation of the micellar formation over free detergent). For solubilisation of membrane proteins, high detergent concentrations can be necessary (typically 10-100xCMC); but to keep the protein soluble it is generally sufficient to keep detergent levels at at least 1xCMC.

Our membranes were resuspended in the solubilisation buffer (50 mM Tris pH 8, 500 mM NaCl and the inhibitor mix CLAPA) using a 1:25 mass ratio of membranes:buffer. After homogenisation on the magnetic stirrer, 0.15% $C_{12}E_9$ (50xCMC) was used to solubilise the receptor. Solubilisation was performed on the magnetic stirrer for 1.5 h at 4 °C followed by ultracentrifugation (120 000 x g, 1 h, 4 °C). The supernatant contained the solubilised protein.

3.1.4 Purification of the 5-HT3RA

3.1.4.1 Affinity chromatography

The Strep tag on the N-terminus of the receptor was used for affinity chromatography on the Strep-Tactin resin (IBA). For a typical purification we used 1.5 mL of the resin/1 g of membranes. We used the gravity-flow set up in columns. The resin was equilibrated with 5x column volumes (CVs) of equilibration buffer (50 mM Tris pH 8, 500 mM NaCl and 0.01% $C_{12}E_9$), the solution containing the solubilised protein was loaded once on the column and washed with 5 CVs of washing buffer (50 mM Tris pH 7.4, 125 mM NaCl and 0.01% $C_{12}E_9$). The protein was eluted with 3 CVs of the elution buffer (50 mM Tris pH 7.4, 125 mM NaCl and 0.01% $C_{12}E_9$ supplemented with 5 mM d-desthiobiotin). The protein was concentrated using Amicon concentrators (Merck Millipore) with a 100 kDa molecular weight cut-off.

3.1.4.2 Size exclusion chromatography

Size exclusion chromatography (SEC) on a Superose 6 10/300 GL column (GE Healthcare) was performed after enzymatic treatments (see the following section 3.1.5.1) to separate the cleavage products or after the amphipol exchange (section 3.1.5.2) to remove the remaining detergent. The column was equilibrated in size exclusion buffer (50 mM Tris pH 7.4). For crystallographic purposes the buffer contained 0.01% $C_{12}E_9$ and 125 mM NaCl. For the cryo-EM experiments, the buffer contained 0.01% $C_{12}E_9$ and only 65 mM NaCl. The SEC performed after amphipol exchange was done using the size exclusion buffer (50 mM Tris pH 7.4, 125 mM NaCl) in the absence of detergent. The 5-HT3RA eluted from the column at around 13.7-14mL and no significant shift was observed for the protein in amphipol compared to the protein in detergent.

3.1.5 Treatement of the 5-HT3RA

3.1.5.1 Enzymatic treatment

The 5-HT3A contains a partially unstructured intracellular domain, which causes the formation of badly diffracting crystals and we were thus using limited proteolysis by trypsin (0.0125:1 mass ratio of trypsin:protein, 2 h at 30 °C) to cleave this region out. SEC was performed immediately at the end of incubation with trypsin, in order to avoid excessive cleavage which could lead to protein degradation.

On the other hand, this unstructured part seemed to prevent aggregation when the protein was used for cryo-EM and thus only the N-terminal Strep tags were removed when we prepared samples for cryo-EM. They were cleaved by the TEV protease (0.04:1 mass ratio of TEV protease:protein, overnight (ON) at 4 °C).

The 5-HT3RA has 3 N-glycosylation sites. Glycosylations added heterogeneity and were perturbing crystallogenesis. We used PNGase F, which is an amidase that cleaves between the innermost GlcNAc and the asparagine residues of high mannose, hybrid, and complex oligosaccharides from N-linked glycoproteins. Cleavage was carried out using the 0.1:1 mass ratio of PNGase F:protein (2 h at 4 °C).

3.1.5.2 Amphipol exchange

The cryoEM structure of TRPV1 *(Cao et al., 2013)* was a landmark, in the field of membrane protein structures solved by this method. That structure was obtained with a sample solubilized in amphipol, and was the reason why we and others performed experiments in amphipol. It has different properties compared to the detergent. It does not form micelles but wraps the protein around its hydrophobic part, thus once all the proteins are protected by the amphipol molecules, no further free amphipol is needed in the solution. Amphipol is a long polymer composed of a different ratio of the monomers containing polar and nonpolar side chains *(Tribet et al., 1996; Zoonens and Popot, 2014)*. We used commercially available amphipol A8-35 (Anatrace) where the number 35 indicates the percentage of the overall amount of polar monomers present in the polymer. In principle, once amphipol is added to the protein-detergent solution, it starts to compete with the detergent for the hydrophobic parts of the protein. The exchange can only be completed by removal of the detergent from the solution either by dialysis or by the use of polymeric beads. We decided to use the bio-bead method rather than dialysis and we optimised the detergent-amphipol exchange protocol based on the publication explaining the use of the bio-beads *(Rigaud et al., 1997)* for optimal detergent removal and the publication describing the exchange of the TRPV1 receptor from detergent into amphipol *(Liao et al., 2013)*. Here I present only the final protocol.

First the protein was concentrated to the final concentration of 0.5 mg/mL. Then amphipol A8-35 was added in a 4:1 mass ratio of amphipol:protein and the solution was incubated (3 h, 4 °C, mixing). After the incubation the Bio-Beads (BIO-RAD) were added in a 106:1 mass ratio of Bio-Beads:protein and incubated overnight at 4 °C while mixing, to remove the detergent from the protein-detergent-amphipol solution. Bio-beads with the bound detergent were then removed from the protein-amphipol solution and SEC was performed as described in the section 3.1.4.2.

3.2 The m5-HT3R preparation - results

My project started as a follow up of the structure of the m5-HT3RA solved by crystallography. At the beginning I took over the protocols for the protein purification and crystallisation of the receptor *(Hassaine et al., 2014)* and I tried to optimise them with multiple aspects in mind, specifically aiming to increase the yields, shorten the purification time and lower the costs. The initial protocol comprised of cell homogenisation, membrane separation by ultracentrifugation, protein solubilisation followed by ultracentrifugation, which led to solubilised protein solution. The next step was a filtration which allowed us to proceed with Strep-Tactin affinity chromatography.

Pre-packed Strep-Tactin columns were used and purification was done using the peristaltic pump loading the sample overnight. To improve homogeneity of the sample and to remove potential flexible parts of the protein, deglycosylation was carried out by PNGase F in a ratio of 1 mg : 0.1 mg receptor to deglycosylase (2 h shaking at 37 °C) and limited proteolysis was done by trypsin in a ratio of 1 mg : 0.013 mg receptor to protease (incubated 2 h at 30 °C).

I optimised the solubilisation step, trying to lower the concentration of detergent used and to shorten the incubation time. In contrast to the initially quite high concentration of $C_{12}E_9$ (1%) used for 3 h at 4 °C, I demonstrated that using a concentration of 0.15% for 1.5 h at 4 °C solubilised the protein to the same extent (Fig. 16).

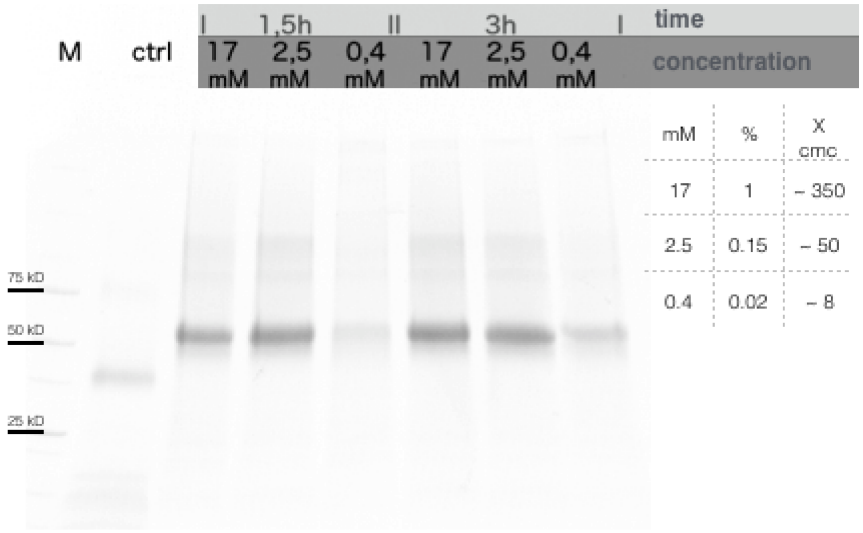

Figure 16 | The effect of $C_{12}E_9$ detergent concentration and incubation time on the 5-HT3RA solubilisation from membrane fractions.

Three detergent concentrations were tested during the 1.5 h and 3 h solubilisations performed at 4 °C. Membranes were incubated while gently mixing on the wheel shaker at 4 °C and spun down (120 000 g, 1 h, 4 °C). The supernatant containing the solubilised protein was loaded onto an SDS-PAGE gel. The SDS-PAGE gel shows that the 17 and 2.5 mM concentration effectively extracted the receptor from the membranes whereas the 0.4 mM concentration was shown to be too low. The shortest time (1.5 h) and lowest concentration (2.5mM = 0,15% = 50xCMC) to allow sufficient extraction were used for further purification. The ctrl sample is the pure receptor after the deglycosylation and trypsin treatment, explaining its different migration compared to the solubilised receptor prior to PNGase and trypsin treatment.

A very time-demanding step was the filtration of solubilised protein solution through 0.22 μm filters. This step was mandatory because of the clogging of the pre-packed Strep-Tactin column filter. We tested the gravity flow set-up and as neither the yield nor the purity of the protein was affected (Fig. 17) we switched to this approach which saved us ~ 2 h of filtration.

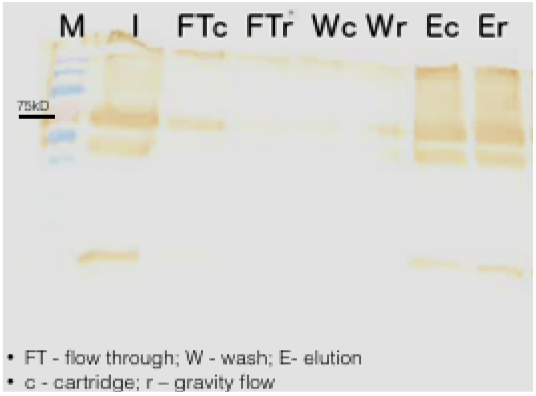

Figure 17 | Comparison of two Strep-Tactin resin based purification setups: gravity flow and pump promoted purification using cartridges.

The solubilised protein solution (filtered by 22 μm filters) from one membrane preparation was split into two parts and loaded onto the gravity flow column or the cartridge resin.

A relatively expensive part of sample preparation was the usage of PNGase F. We decided to adapt the protocol from *(Loo et al., 2002)* to purify PNGase F in-house instead of using the commercially available enzyme. I adapted it and we now express periplasmic PNGase F and purify it using NiNTA and size exclusion chromatography. We verified the activity of in-house purified PNGase F and tested the conditions for its activity. Compared to the initial 2 h incubation at 37 °C we have shown that the same level of deglycosylation can be achieved even when the reaction is incubated at 4 °C. This might prevent protein denaturation caused by increased temperature (Fig, 18).

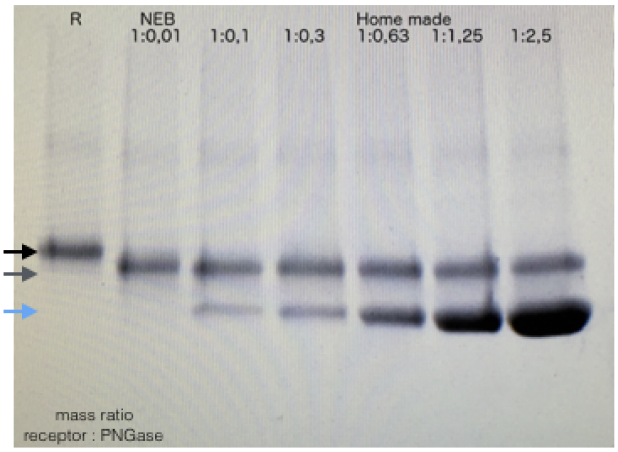

Figure 18 | The efficacy of the in-house prepared PNGase F compared to the commercially available one.

We optimised the overexpression and purification of PNGase F. We incubated purified PNGase F with the receptor in different ratios for 2 h at 4 °C. The black arrow shows the glycosylated receptor used as a control. The receptor was fully deglycosylated in all cases, resulting in a single band (grey arrow) on the SDS-PAGE gel after incubation with PNGase F (indicated by the blue arrow).

The isolation, purification and enzymatic treatment of 5-HTRA are carried out over 2 days. Generally, the yields vary from 0.2 - 0.3 mg of pure and treated protein per 1 g of membrane fraction after the final size exclusion chromatography, where a nice homogeneous peak corresponding to the pentameric receptor is observed (Fig, 19).

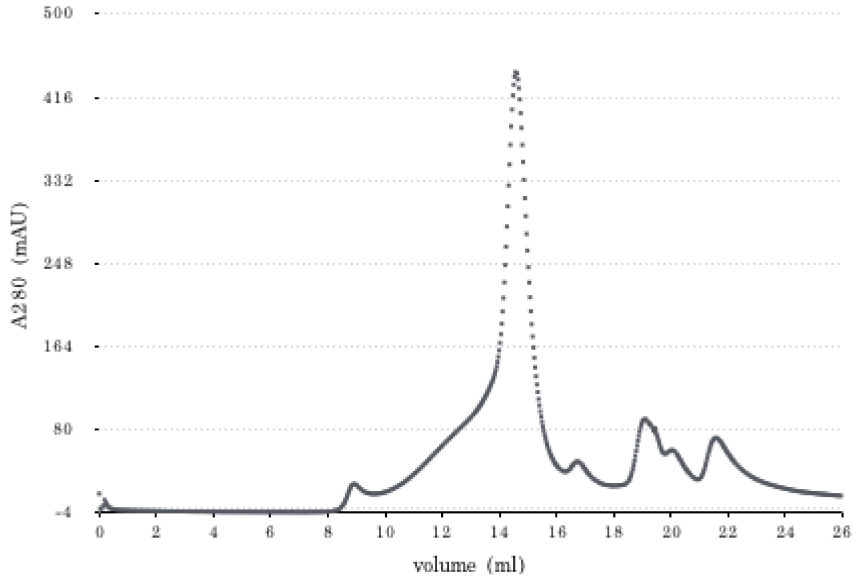

Figure 19 | The chromatogram of the 5-HT3RA after the purification on Strep-Tactin, the deglycosylation by PNGase F and the limited proteolysis done by Trypsin.

There is a very small fraction of aggregated protein, which elutes at the beginning of the column (8 mL). The main peak corresponds to the treated receptor (elution at ~14 mL). The fraction eluted at 16 mL probably corresponds to the monomers and we can observe the PNGase peak and the peak resulting from the Trypsin chopped protein fraction at the end of the column.

4 Crystallography

4.1 Crystallography - materials and methods

4.1.1 Vapour diffusion trials

All the screening was carried out on the High-Throughput crystallography platform (HTX-lab) at the EMBL in Grenoble.

Manual plates were mostly set up using a protein concentration of ~8 mg/mL. During the optimisation process different ratios of the protein:reservoir drops were used. To slow down the growth kinetics Ali-oil was used to cover the reservoir in the hanging drop set up. Microbatch under-oil crystallography was performed. Different initial concentrations of the protein were used (from 1 mg/mL up to 10 mg/mL). The seeding method used was seeding into the clear drops. Stepwise dehydration and direct dehydration were tested to improve the crystal X-ray diffraction.

4.1.2 The lipidic cubic phase (LCP) trials

The protein was concentrated typically to 40 mg/mL. In one of the trials the VHH15 was used to further stabilise the receptor but its use increased the hydrophilic part pointing out of the lipid bilayer, which is not favourable for the LCP method and thus we used mostly the receptor alone. In collaboration with the platform for high-throughput LCP crystallisation (Valentin Gordeliy's group, currently at EMBL Grenoble), we set up multiple plates. Commercial screens (Cubic phase I and II (QIAGEN) and MemMeso (Molecular Dimensions)) as well as plates based on the optimisation conditions arising from the positive vapour diffusion trials.

4.1.3 The detergent screen with a focus on further use in X-ray crystallography

We re-screened a dozen detergents ($C_{12}E_9$, $C_{12}E_{10}$, DDM, MNG3, OGNG, OG, cymal5, cymal6, cymal7, LDAO, LAPAO, FosC12), measuring the receptor stability upon heating, with the aim of selecting one with a shorter hydrophobic tail forming smaller micelles to allow for the formation of better protein-protein crystal contacts. We followed the intrinsic fluorescence of the protein's tyrosines and tryptophans during thermal denaturation of the receptor. Addition of 9% detergents was followed by 15 min

incubation on ice and then the measurement was performed. Typically the measurement was performed in the range of 20-100 °C using 2 °C/min steps. The fluorescence at two wavelengths, 330 and 350 nm was recorded. The 350/330 nm ratio of the two wavelengths was plotted against temperature and represents the unfolding transitions. The data were measured on the Prometheus (NanoTemper).

As a complementary method we used SEC performed after the heat shock. Protein was purified using $C_{12}E_9$ during solubilisation and for stability in solution. Different detergents were added at the 1% concentration and the mixture was incubated 15 min at 55 °C. After ultracentrifugation to remove potential aggregates, the sample was injected onto a Superose 6 column equilibrated with buffer containing 0.01% $C_{12}E_9$. The same concentration of this detergent was used in the running buffer (running buffer as for protein purification, see 3.1.4.2).

4.1.4 Blue native electrophoresis

Native gels can qualitatively characterise the size of protein complexes. Regarding protein-protein interactions this method can even answer binding stoichiometry questions. We used native electrophoresis for the estimation of the binding ratio in between nanobodies and the 5-HT3A.

All the buffers and procedures were prepared and performed according to the NativePAGE Novex® Bis-Tris Gel System manual (Novex, LifeTec MAN0000557). Briefly, 6% polyacrylamide gels were cast. 10 µg of the purified 5-HT3 were mixed with the 1:2 molar ratio of one receptor subunit:VHH and incubated on ice for 10 minutes. The sample was mixed with the sample buffer (for reference see the manual mentioned above) and 1 µL of 0.4% Coomassie G-250 per 10 µL of mix. Anode and cathode buffers were prepared according to the manual and filled into the electrophoresis system. We loaded the samples onto the gel prior to complete filling of the apparatus with the cathode blue buffer for better visualisation. The electrophoresis was performed either in the cold room or on ice at 150 V for ~2 h. When the run is complete, the blue cathode buffer, migrated through the gel, should start appearing in the normally transparent anode buffer. Extensive destaining of the gel is needed. The gel was first fixed by immersion in 100 mL fixing solution (containing 40% methanol and 10% acetic acid), then microwaved for 45 s and incubated on the shaker for 20 mins. The fixing solution was decanted. The gel was then destained in 8% acetic acid, microwaved for 45 s and incubated until the gel background became transparent.

4.2 Crystallography - results

4.2.1 Crystallisation of the m5-HT3RA using nanobodies

4.2.1.1 VHHs

Camelids possess antibodies made of heavy chains only. Engineered terminal domains of these antibodies are called nanobodies or VHHs. These domains retain their antigen-binding ability, their typical size is ~15 kDa, and they can generally be overexpressed in *E. coli*. The antigen-binding paratope is made up of 3 complementary binding regions (CDR1-3).

The use of nanobodies has multiple benefits in structural biology *(Pardon et al., 2014)*. They might help to solubilise the protein by increasing its polar surface and they can stabilise the protein, which reduces heterogeneity of the sample. Their use in crystallography can be instrumental in solving the structures of unknown proteins by enabling molecular replacement. Additionally their presence might also help to promote crystal growth by supporting the formation of crystal contacts, as was the case with crystallisation of the m5-HT3RA/VHH15 complex *(Hassaine et al., 2014)*. After this initial success, our strategy was to try to find another nanobody, which would stabilise the receptor in another conformation.

Nanobodies are obtained following immunisation of the animal (see *Pardon et al. (2014)* for methods). The protein of interest is injected into an animal and its immune response yields new antibodies. A library of all VHHs is created and those interacting with the protein of interest are selected by phage display and then assayed using ELISA tests with the purified protein. The nanobodies used in our studies were from collaborators in Marseille. The information available to us are the VHH sequences and their ELISA score. For better orientation in our library composed of about 15 nanobodies we sorted them into six groups according to their sequence similarity (Fig. 20).

Group A	Group B	Group C	Group D	Group E	¨Rest¨
VHH7 VHH14 VHH6	VHH4 VHH12 VHH15	VHH2 VHH8 VHH16	VHH5 VHH9	VHH17 VHH18	VHH1 VHH10 nVHH2 nVHH15

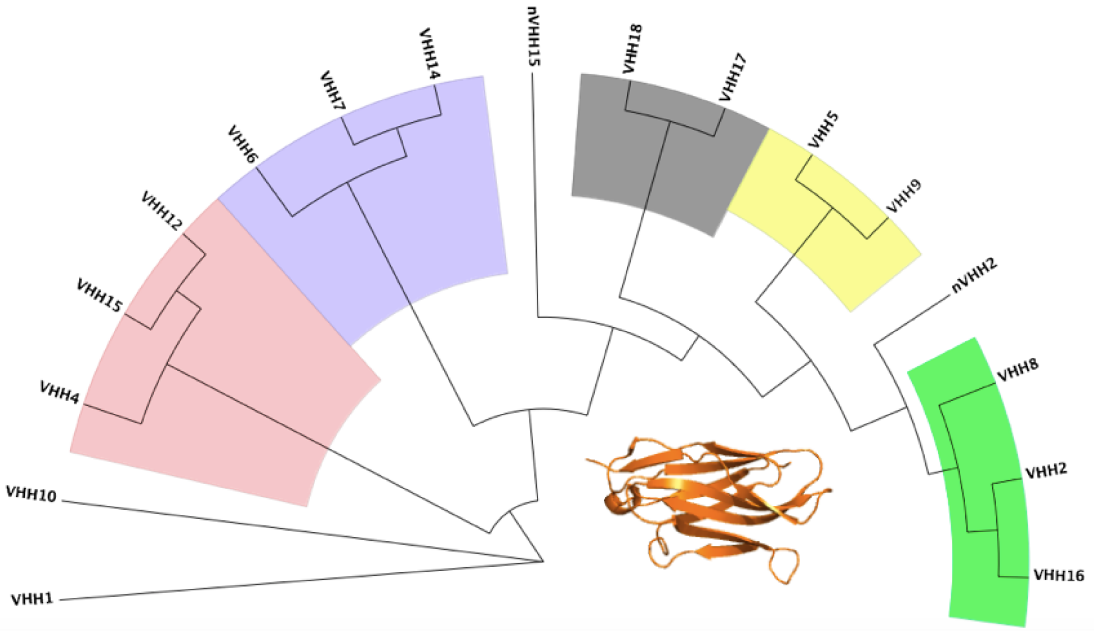

Figure 20 | The classification of nanobodies according to their sequence similarity.

For the purpose of crystallographic screening we needed to sort all nanobodies in our library and work only with representatives from each group. The table summarises how nanobodies were sorted into six groups, with VHH15 (for which we already had a structure) highlighted in group B. For better visualisation of their divergency the phylogenetic tree using the neighbour-joining method was used. The group colour coding corresponds to the groups highlighted on the tree.

4.2.1.2 Co-crystallisation

Following the current trend in crystallography, after the selection of nanobodies from sequentially different groups (one for each group) we used the service of the HTX laboratory on campus to set up commercial screens (generally starting with 6 screens: PACT, PEGs, JCSG and Wizzard I+II).

Protein was purified as described in section 3.1.3-4. After size exclusion chromatography, peak fractions were pooled together and concentrated to ~8 mg/mL. Before crystallisation, the protein was mixed with VHH in a 1:2 molar ratio, (1 monomer of the m5-HT3RA with an excess of 2 VHHs). This mixture was supplemented with 1 mM of Cymal-6. Here the role of Cymal-6 is not to further

stabilise the complex, as demonstrated by our thermostability data (Fig, 22). We hypothesise that the positive effect of Cymal-6 during crystallisation is caused by a decrease of the micelle size that promotes protein/protein contacts and results in better crystal packing.

Working towards our goal, we focused on the nanobodies sufficiently distinct from VHH15, hoping that they will stabilise the receptor in another conformation. Unfortunately, even though we have access to biophysical methods to characterise receptor-VHH interactions, we lacked a way to characterise them functionally, which would probably provide the optimal criteria for selection of the crystallisation candidates.

Using 7 different nanobodies we obtained 157 hits, which largely exceeded our expectations. We focused mainly on the conditions which were as different as possible from the conditions under which the structure of receptor in complex with VHH15 was obtained. Manually, we reproduced more than 70 conditions selected to maximise diversity. The majority of them gave crystals. The synchrotron measurements confirmed that these were, apart from very few exceptions, protein crystals with a poor diffraction, ranging from ~30 to ~9 Å at most. We optimised all conditions that yielded crystals but this did not improve their diffraction. Altogether we shot around 550 crystals.

The chemical compositions of the hits obtained were very divergent and we could not observe any clear pattern. Crystals grew at different pHs (5-10), using different organic and inorganic salts and PEGs (from 3350 - 10000) (see examples in (Fig. 21)). Changes in chemical composition of the mother liquor (type and amount of ingredients) did not improve the diffraction by our crystals and we focused mainly on physical parameters. From the classical methods used for diffraction improvement we tried: different growth temperatures, seeding, dehydration and growing under oil using microbatch crystallisation. Using recently developed methods we also tried to use CrystalDirect plates, which make it possible to shoot crystals without fishing, directly in the plate. This approach reduces possible manipulation damage but it is compatible only with room-temperature measurements. Except for the micro-batch method, all others listed led to crystals but did not affect diffraction. We collected data of crystals diffracting to 9 Å in the hope of further processing. We were able to determine the space group of crystals grown with two different VHHs but for none of them we were able to get a molecular replacement solution.

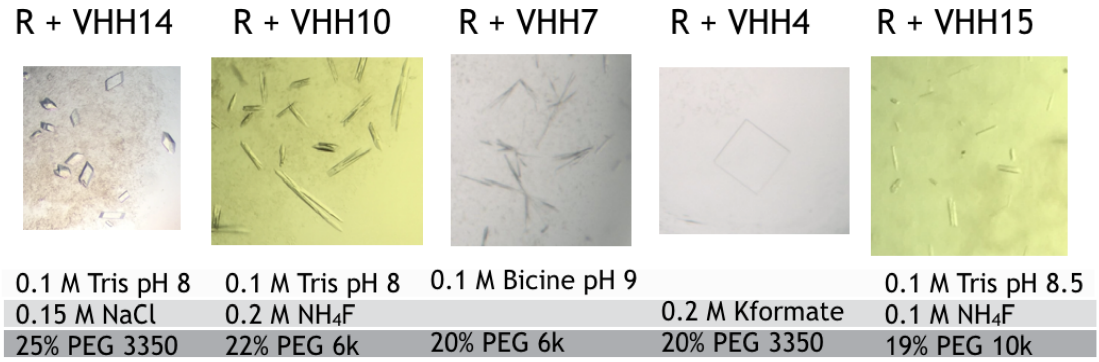

Figure 21 | Microscope images of crystals obtained under some selected conditions.

This schematic shows the variability in the crystal shape and also the broad range of conditions under which the crystals were obtained. We obtained crystals using different pH, inorganic and organic salts and also different PEG types.

4.2.1.3 The Effect of different detergents on m5-HT3RA stability

Neither the use of the nanobodies at our disposal nor the optimisation of crystallisation conditions led to X-ray diffraction of sufficient quality from any of the many crystals obtained. We thus concluded that larger changes were required and started to re-evaluate the sample preparation protocol. The choice of detergent influences solubility, stability and of course plays an important role during crystallisation. For instance, the crystal quality of the m5-HT3RA/VHH15 complex had been improved when Cymal-6 was used as a supplement to $C_{12}E_9$, possibly because Cymal-6 reduced the micelle size and thus favoured protein-protein contacts in the crystals. Consequently, we performed a new thermal stability detergent screen using NanoTemper's Prometheus and SEC (see 4.1.3). We observed a correlation between the length of the carbon tail and the protein stability (see below). Although detergents with longer carbon chains were better at stabilising the receptor, some of the shorter tail detergents stood out from the screen. Namely the Cymals and undecyl-maltoside (UDM), the latter being the detergent used for crystallography of the nicotinic α4β2 receptor *(Morales-Perez et al., 2016)*.

Figure 22 depicts thermal denaturation curves for the Cymal series of detergents, where an effect of the carbon tail length was observed, with $Tm_{(Cymal\text{-}5)} = 52\ °C < Tm_{(Cymal\text{-}6)} = 57\ °C < Tm_{(Cymal\text{-}7)} = 60\ °C < Tm_{(C_{12}E_9)} = 64\ °C$. The comparison of $C_{12}E_9$ and UDM revealed that UDM might also be a good candidate for crystallographic studies of 5-HT3RA. These detergents stabilise the receptor enough to be used for crystallography, while potentially enabling easier formation of protein-protein contacts.

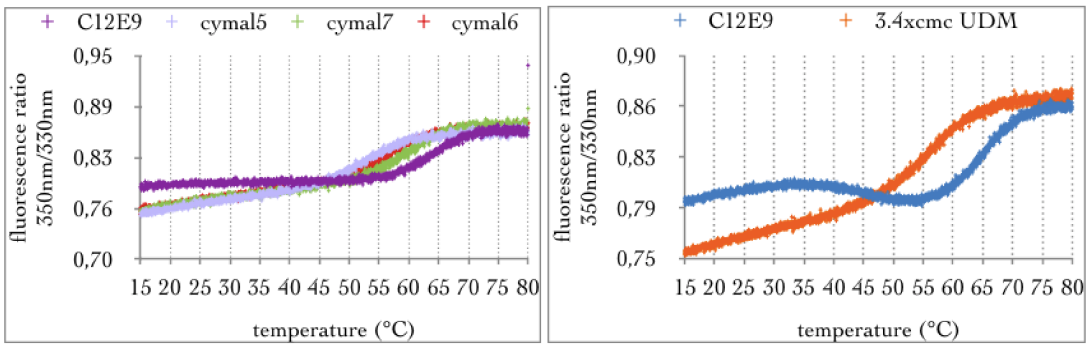

Figure 22 | The thermostability of the receptor after the addition of different detergents.

We screened multiple detergents on NanoTemper's Prometheus with the aim to find the shortest hydrophobic tail detergent, which would promote crystal contact without perturbing the stability of the receptor. The Cymal detergents and the UDM stood out from the screen.

Because of its similarity to DDM in which the receptor remains active and in view of the recently solved structure of the other Cys-loop receptor in this detergent, we decided to proceed with UDM. Moreover, the size exclusion chromatography profile of the m5-HT3R in presence of UDM as compared to $C_{12}E_9$ looked very encouraging (Fig. 23)

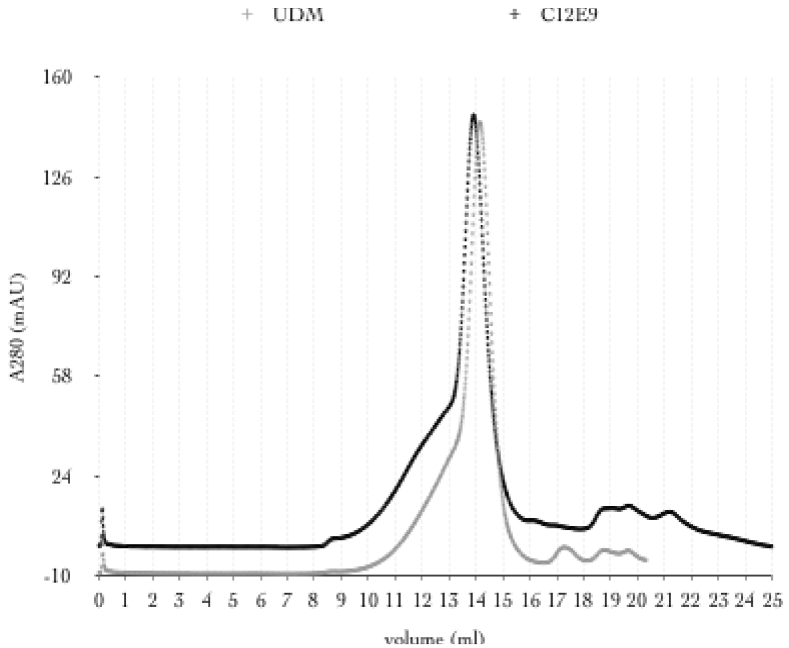

Figure 23 | The size exclusion chromatography profile of m-5HT3R in UDM as compared to $C_{12}E_9$.

The receptor was solubilised in $C_{12}E_9$, purified using its Strep-tag, deglycosylated and TEV protease treated prior to SEC on the column equilibrated in, and in running buffer containing the UDM detergent.

Based on our previous experience with the m5-HT3A receptor we set up he PEGs screen and surprisingly observed 5x more promising hits (objects rather than crystals) in the conditions where UDM was used compared to where $C_{12}E_9$ was used, even without the use of nanobodies. At this point, the cryo-EM started to provide early positive results and we decided to focus mainly on it and not to continue with crystallography.

4.2.1.4 Biochemical characterisation of the nanobodies

From all of the above-mentioned, it is clear that it is not possible to try extensively the combination of all approaches with all different nanobodies and all crystallisation conditions. The difficulties encountered emphasised the need for better biophysical characterisation of our nanobodies.

Looking at other examples of Cys-loop receptors crystallised with chaperones (either Fabs *(Hibbs and Gouaux, 2011)* or VHHs) we noted that in all successful cases there were 5 chaperones bound per receptor (one per subunit). Thus we sought for a method to determine the binding ratio between the receptor and nanobodies. We tested native electrophoresis for this purpose. The receptor alone and the receptor pre-incubated with VHH15, which binds in a 5 to 1 ratio in the crystal structure, were used as references. Early results indicated clearly the difference between these two samples but the resolution was not good enough. Thus, we turned to BlueNative electrophoresis and replaced the detergent with amphipol. This approach gave us an estimate of the binding ratio (Fig. 24).

For example, VHH4 is very closely related in sequence to VHH15 (97% sequence similarity / 6 point mutations), indicating that it should bind in the same ratio; indeed those two complexes migrate to the same position on the gel. Interestingly, preincubation with nanobody VHH10 does not seem to affect the receptor migration on the BlueNative electrophoresis gel and we were able to confirm the lack of this nanobody in the corresponding crystals by SDS PAGE (data not shown).

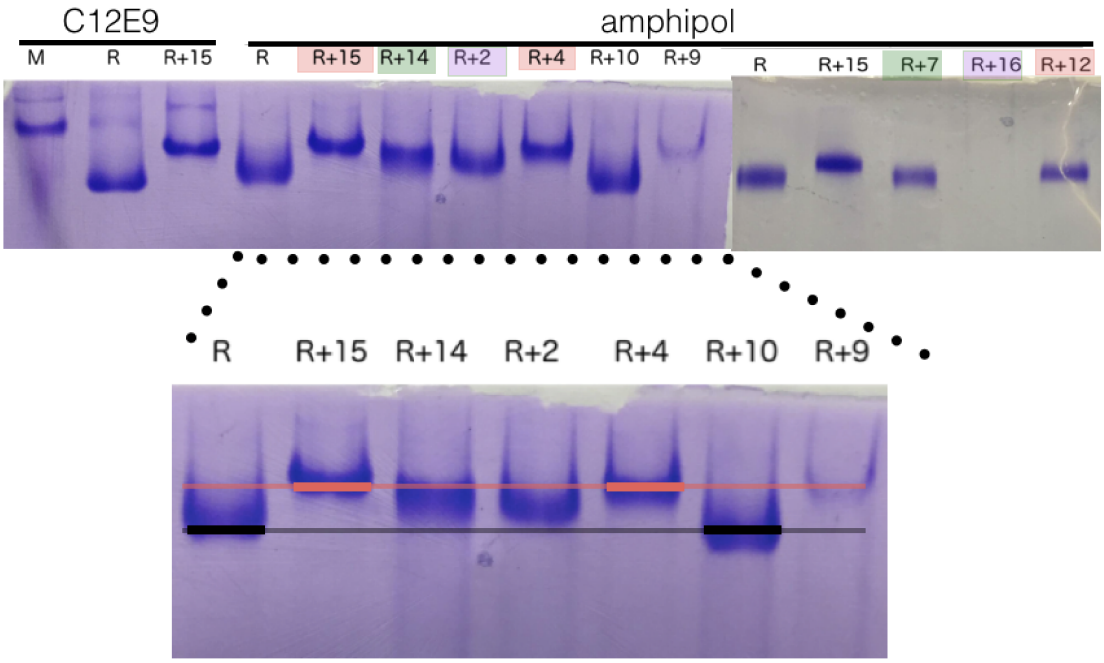

Figure 24 | BlueNative electroforetograms of m5-HT3RA in amphipol in the presence of different nanobodies.

Migration of the receptor incubated with nanobodies VHH15 and VHH4 (red line) corresponds to the same number of nanobodies bound to the receptor. Nanobody VHH10 does not seem to be present in the complex and thus does not change its migration under native conditions.

Another important parameter influencing the stability of the complex is the binding affinity of the antibody to the receptor. We performed labeled microscale thermophoresis and we were able to demonstrate that this method is not appropriate in our case (extensive trials, results not shown). The conditions of the protein labeling led to m5-HT3R denaturation. The measurement obtained using the non-precipitated fraction of labeled protein gave an uninterpretable binding isotherm. Surface plasmon resonance seems to be a good alternative for assessing protein-protein interactions but, as we know from the trial with VHH15, the single cycle kinetics is the only mode possible, somehow complicating data interpretation.

Finally, we lacked easily accessible functional tests for the elucidation of the nanobody effect on the protein stability. Functional tests would be probably the best indication of stability when looking for the nanobody stabilising the receptor in another conformation than VHH15, which acts as an antagonist. Some of the experiments I performed on the expression optimisation were reported in a case study in Membrane Protein Structure and Function Characterization book *(Hassaine et al., 2017)*.

5 Electron microscopy

Currently, electron microscopy is finding its place next to the other near-atomic resolution structural determination methods, such as X-ray crystallography. It is about 70 years ago when the first biological sample was imaged using EM and since then a huge amount of progress was achieved. The electrons being scattered by the air required the evacuation of the microscope column and thus the sample also needed to be dehydrated, which caused the limited contrast of the images obtained - micrographs. This introduced the need for a contrast increase and that's how negative staining EM appeared *(Huxley and Zubay, 1961)*. In negative staining, the electron-dense solution, mostly uranyl acetate, surrounds the specimen being observed and increases the contrast. Passing through the imaging of the 2D crystals kept dehydrated in the glucose solution, this led to a resolution of about 7 Å *(Henderson and Unwin, 1975)*, but the real breakthrough came with the routine use of sample freezing and the introduction of the cryo-stage into the microscope. That was the beginning of the cryo-EM method as we know it today. Nowadays, the sample in aqueous solution is rapidly frozen by the liquid ethane, allowing formation of the amorphous solid phase instead of crystalline ice, which had resulted in biological sample degradation in the past.

5.1 Electron microscopy - material and methods

5.1.1 Negative stain EM of m5-HT3RA

As an initial quality control we performed negative-staining transmission electron microscopy using the electron microscopy platform of IBS. Purified sample (around 1 mg/mL) was deposited on a glow-discharged carbon grid and stained with uranyl acetate pH 7. Images were taken with a Tecnai12 Microscope (FEI) operating at 120 kV, a LaB6 electron source and an Orius 1000 GATAN camera.

5.1.2 Cryo-EM of the m5-HT3RA

During the cryo-EM sample optimisation we performed multiple tests. Samples of different concentrations were used, starting from 0.5 up to 24 mg/mL. We used different commercially available grids. Samples were frozen using a variety of blotting time lengths. Changing the biochemical sample preparation we went back to the optimisation of grid preparation and fine tuned the conditions for all biochemically divergent

samples. The typical protein concentration used in amphipol or in detergent was around 10 mg/mL and about 3.5 mg/mL, respectively. Samples were deposited on the glow-discharged carbon grids and frozen by FEI Vitrobot in liquid ethane. Samples were stored under liquid nitrogen until being imaged. Imaging was completed either at our institute on the EM platform using Tecnai G2 Polara cryo-transmission EM with a 300 keV field emission gun (FEG) equipped with a K2 Gatan camera, or in the C-CINA scientific group in Basel on the KRIOS cryo-TEM with a 80-300 keV FEG, Gatan Quantum-LS Energy Filter (GIF) with a Gatan K2 Summit direct electron detector. Particle picking was carried out using Dr. Kai Zhang's Gautomatch and the data treatment was done using Relion software *(Scheres, 2012)*.

5.2 Electron microscopy - results

The Cys-loop receptors are relatively good candidates to be studied by cryo-EM because of their size, their five-fold symmetry and the pre-existence of models (structures solved by X-ray crystallography). The first structure of a Cys-loop receptor ever solved was done by cryo-EM and it was the structure of the nAChR from the electric organ of the Torpedo fish *(Miyazawa et al., 2003)*. At the time we started working on the 5-HT3 project, cryo-EM had already been successfully applied to the GlyR *(Du et al., 2015)*, providing insights into the open, closed and desensitised structures of this receptor.

In my hands, the X-ray crystallization trials did not lead to structures of other conformational states in addition to that already known. Encouraged by the structure of TPRV1, a membrane protein, whose structure was solved at 3.4 Å resolution using cryo-EM *(Cao et al., 2013; Liao et al., 2013)*, we decided to use electron microscopy as a complementary method (and as time passed by, as our main structural method).

5.2.1 Initial trials and optimisation

In our early microscopic trials, a few years back, we used the 5-HT3 receptor solubilised in amphipol. Our/the naive rationale was of a dual nature: the pioneering study of TRPV1 had proven the usefulness of amphipols in structural studies (finally), and microscopists advised us to avoid the presence of detergent during the freezing process. We adapted the exchange of detergent for amphipol as described in section 3.1.5.2. We could obtain a homogeneous pentameric receptor after size-exclusion chromatography (Fig. 25).

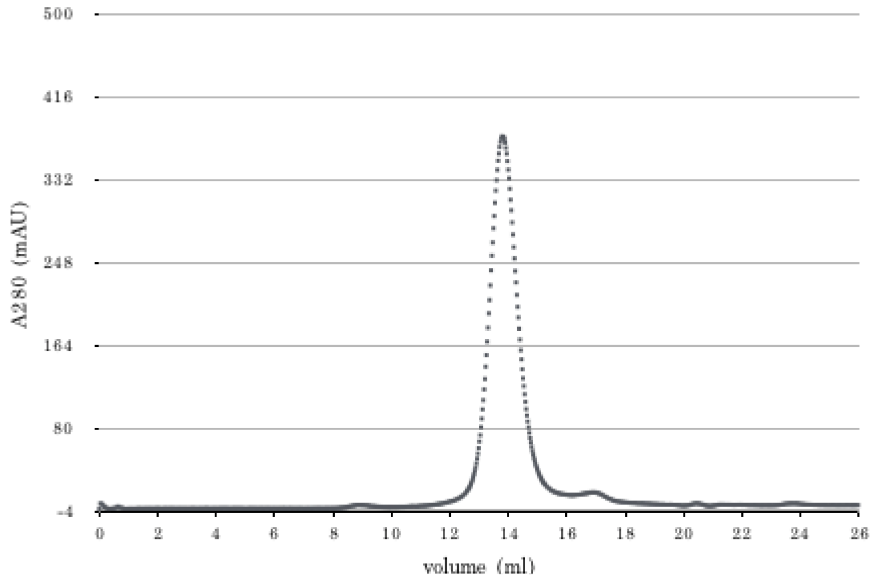

Figure 25 | Size exclusion chromatography profile of m5-HT3A receptor after the amphipol exchange, using Superose 6 column.

We observe a symmetric peak of the pentameric receptor (verified by EM) at around 13.5 mL, unshifted compared to the protein-detergent complex.

Apart from this change in tensio-active, we first kept the protein preparation procedure similar to that for the crystallographic sample, reasoning that if it could crystallise, the protein was of good quality. Thus we used receptor deglycosylated by PNGase F and partially digested by trypsin leading to the removal of the Strep-tag and of the unstructured intracellular region. Negative stain microscopy in the presence of VHH15 nanobodies yielded good-looking micrographs, with side and top orientations of proteins, and almost no aggregation (Fig. 26A) Unexpectedly, when we proceeded to cryo-EM, we observed aggregation of the entire sample caused by the nanobodies, making it impossible to pick single particles (Fig. 26B). The first lesson learnt was thus that a good quality negative stain does not necessarily predict the quality of cryo-EM micrographs. Thus we decided to optimise the conditions directly by cryo-EM.

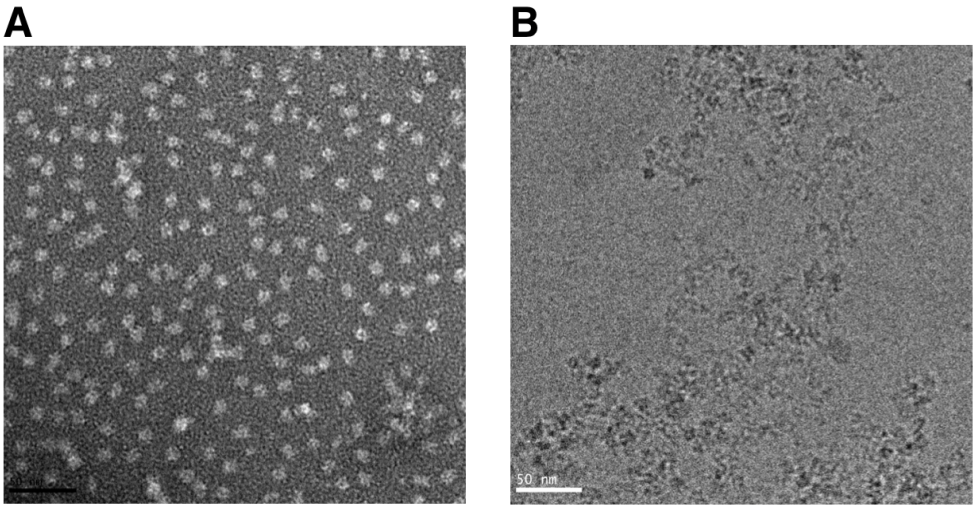

Figure 26 | Different behaviour of the biochemically identical sample (deglycosylated and trypsin-treated m5-HT3R with the VHH15 nanobody) influenced by the preparatory process for negative-stain EM (A) and cryo-EM (B).

A) On the micrograph from the negative stain microscopy we observed only slight aggregation, the sample is mostly homogenous and both top and side views are present. **B)** The cryo-EM micrograph depicts high aggregation of the sample with the majority of top views.

Early trials with the receptor in amphipol without nanobody present resulted in micrographs containing mostly one orientation of receptors: top views (Fig. 27A). In addition, it seemed that we had an aggregation problem, shown by the presence of 'darker' top views with higher contrast and 'prolonged' side views (Fig. 27B), which we hypothesised were head-to-head or head-to-tail dimers.

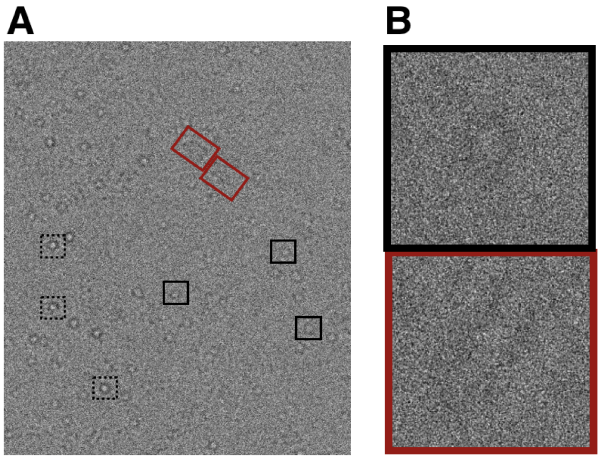

Figure 27 | Orientation and aggregation (dimerisation) problem observed on a representative micrograph of the sample in amphipol.

A) There are two groups of top views present, which differ in their contrast (black boxes vs dashed black boxes), as well as the prolonged side views (red box). **B)** A close-up of one top view (black) and one prolonged side view (red).

We screened different surfactants to solve the orientation and aggregation problems. We tested the more polar amphipol version A8-75 and observed greater aggregation while the orientation problem persisted (Fig. 28).

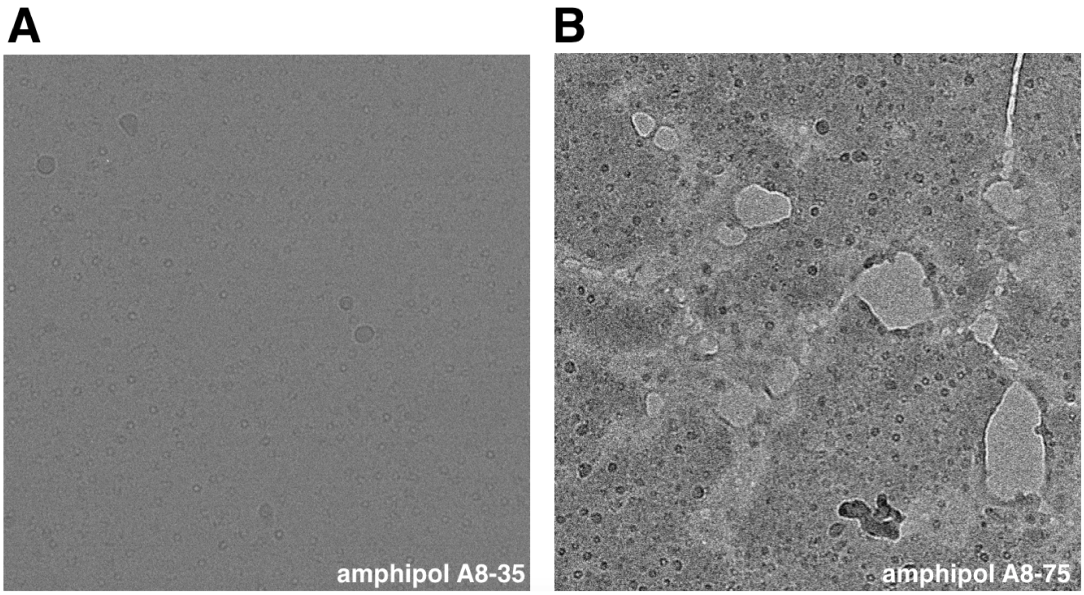

Figure 28 | Micrographs of m5-HT3RA showing the effect of the two different types of amphipol.
The presence of the charged amphipol A8-75 resulted in increased aggregation of the sample **(B)** and, compared to the sample in amphipol A8-35 **(A)**, neither did it solve the orientation problem.

As fluorinated detergents (F-TAC) had been used to rescue anisotropic orientations of membrane proteins on EM grids, we tested the effect of the addition of F-TAC. The addition of 0.2% F-TAC increased the proportion of side views of the receptor. Because 0.2% roughly correspond to the concentration required to saturate the air/water interface in a grid hole, one hypothesis is that F-TAC impact orientation via surface tension modification, and not via interaction with the protein or amphipols. A side effect of the addition of F-TAC was that fewer particles were present in the holes. We tested grids with a 2-5 nm layer of carbon on top of the holes to increase the number of particles, but this resulted in completely crowded unusable micrographs. We were also concerned that the carbon layer might preclude the acquisition of high-resolution data and decided to instead make changes to the protein concentration. Compensating the lower density of receptor by an increased starting concentration (up to ~20 mg/mL), we collected a dataset with this sample (5-HT3R-Apol-F-TAC) on the G2 Polara cryo-transmission EM with a 300 keV FEG equipped with a K2 Gatan camera but it yielded only a reconstruction of limited resolution, at about 8 Å. We were concerned that

conformational flexibility of the receptor might prevent us from reaching a better resolution and we thus collected a second dataset, using a receptor inhibited with 1 mM granisetron. The dataset (5-HT3R-Apol-F-TAC-granisetron) was collected on the Titan Krios microscope in the Center for Cellular Imaging and NanoAnalytics (C-CINA) in Basel. From 421 micrographs, ~125k particles were picked using the low-filtered model of the crystallographic structure. After several rounds of 2D classification, the best looking classes were put together and ~50k particles were used for 3D classification. The best class was further refined, trying the application of different masks, and the final resolution was ~7 Å (Fig. 29).

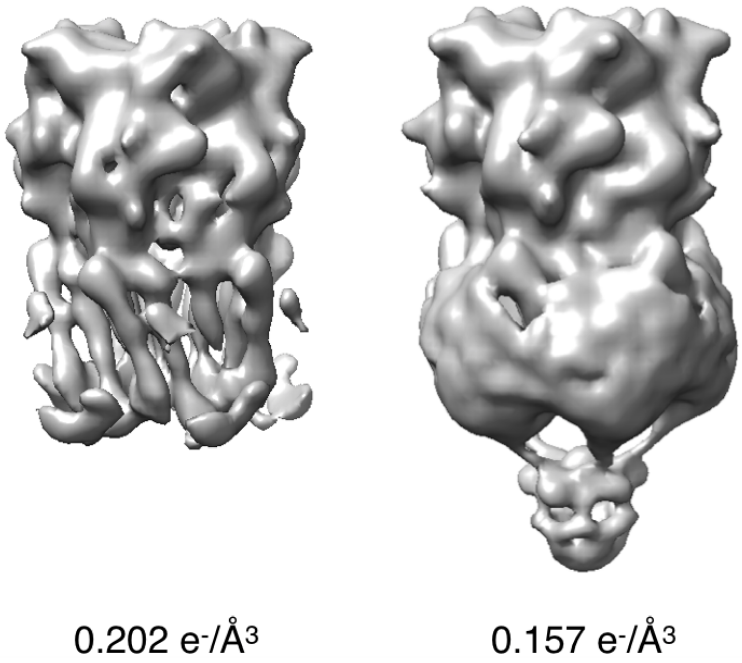

Figure 29 | Two different contouring procedures used to demonstrate the structural data quality of the m5-HT3RA in amphipol in the presence of 1 mM of the antagonist granisetron.

Apparently, the TMD is not as well resolved as the ECD. Moreover, the ICD structural information is only very limited.

One of the parameters, which influences the quality of the data collected is the ice thickness. In our case, the ice layer was probably too thick (as evidenced by the difficulty of seeing side views on raw images) to obtain the atomic resolution of the receptor. Apart from the nature of the particles themselves, the composition of the buffer composition also influences ice thickness. The salt concentration, together with the type of tensio-active molecule used, can be crucial. We thus decreased the salt concentration by a factor two but were limited by the relatively high concentration of F-TAC (0.2 %).

We therefore took a step back and returned to the testing of surfactants, focusing on detergents at this time. Specifically, we tried 0.05% DDM, 0.1% MNG3 and 0.01% $C_{12}E_9$. When using DDM or MNG3, the receptor was purified in $C_{12}E_9$ and we exchanged detergents during the final SEC. According to the SEC profiles, the receptor was perfectly homogenous in the presence of all detergents. Although both alternative detergents, DDM and MNG3, seemed to at least partially solve the orientation problem, they caused significant aggregation of the receptor (Fig. 30).

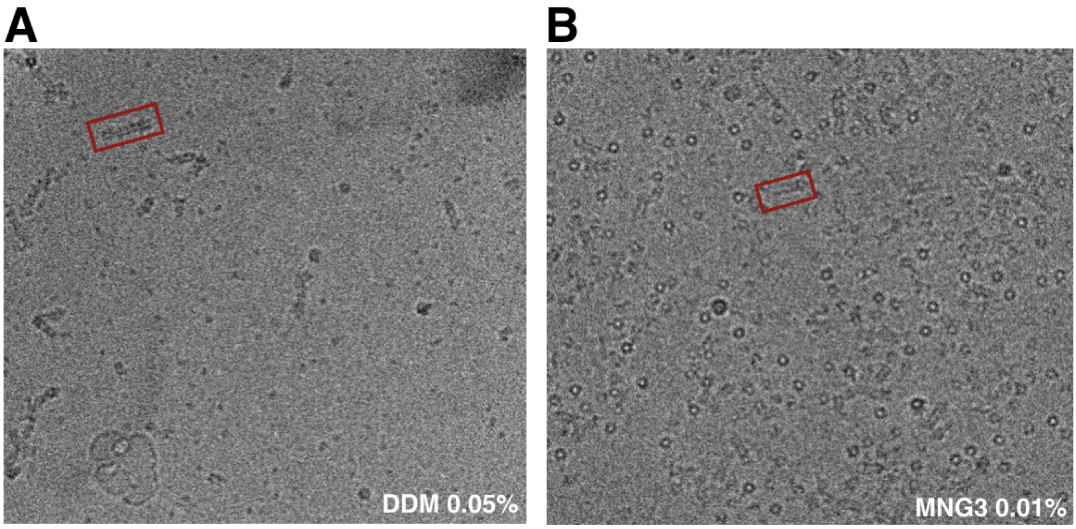

Figure 30 | Two different contouring used to demonstrate the structural data quality of the m5-HT3RA in amphipol in the presence of 1mM of the antagonist granisetron.

The use of alternative detergents for cryo-EM studies of the m5-HT3RA. Both detergents caused significant aggregation of the receptor (red boxes). Interestingly, in 0.05% DDM, the orientation switched from top views to almost exclusively side views. Even though multiple orientations were present when 0.01% MNG 3 was used, the aggregation persisted.

In the end, the detergent $C_{12}E_9$ was thus shown to be the best choice. It enabled the observation of multiple orientations of protein on the grid and we solved the aggregation problem, which occurred during the freezing step, by omission of the limited digestion (using trypsin) step, which was routinely used for crystallographic studies. Additionally, we retained the disordered intracellular domain of the protein in the hope that its presence will prevent aggregation. To mimic the natural conditions as closely as possible, we used lipid additives (0.01% phosphatidic acid, 0.01% cholesterol hemisuccinate, 0.01% brain phosphatidylcholine, Avanti Polar lipids). After testing a range of grids, we decided to use the Cu-Rh grids, which resulted in good sample quality with the required amount and distribution of particles (Fig. 31). These optimised conditions were a good starting point for performing structural studies.

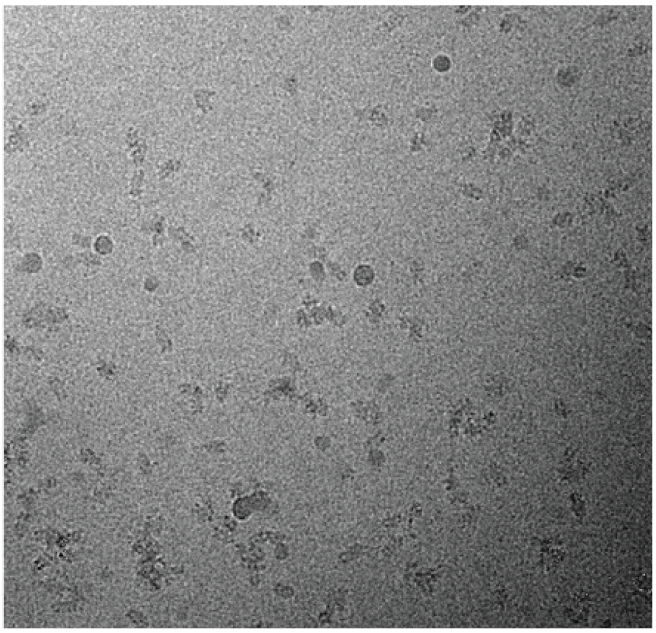

Figure 31 | The representative micrograph of the m-5HT3R after the final sample and the grid preparation optimisation.

The deglycosylated and TEVtreated m-5HT3R in C12E9 detergent supplemented with lipids (0.01% phosphatidic acid, 0.01% cholesterol hemisuccinate, 0.01% brain phosphatidylcholine) shows multiple particle orientations and low aggregation.

5.2.2 The gating mechanism of the m5-HT3RA (enclosed publication)

In the last decade, from the appearance of the first ELIC structure (and even before) until today, huge efforts have been made to elucidate the gating mechanism(s) of Cys-loop receptors. The "steady state" structure-to-function interpretation remains the only method available for this purpose. To date, there are only few receptors whose structures have been solved in multiple conformational states, which enables us to understand their complex gating mechanism. Specifically, these are the structures of the WT GLIC receptor, the GluCl receptor, the engineered GlyR structures and the m5-HT3R structures published in parallel. Here I present our recently published data on the 5-HT3R. Four structurally distinct states of 5-HT3RA provide, for the first time, insights into the gating mechanism of the cation-selective pLGIC. To get the most out of the structures obtained, substituted cysteine accessibility mutagenesis (SCAM) and voltage-clamp fluorometry (VCF) were performed to identify the residues lining the channel and involved in local conformational changes. Moreover, in collaboration with F. Dehez and C. Chipot (CNRS, Nancy, France), we performed molecular dynamics

simulation studies to further characterise the ion permeation of the channel. Combining the structural and functional studies, we propose a functional interpretation of all of the four structures obtained, widening our knowledge of the gating mechanism (see enclosed publication that follows (pages 77 – 98)).

For the sake of completeness I would like to note that the 5-HT3RA open pore and agonist-activated closed pore structures solved by cryo-EM were published independently by Basak and co-workers *(Basak et al., 2018b)* and the structural comparison follows the enclosed publication with our results and can be found in the section 5.3.

LETTER

https://doi.org/10.1038/s41586-018-0672-3

Conformational transitions of the serotonin 5-HT_3 receptor

Lucie Polovinkin[1], Ghérici Hassaine[2], Jonathan Perot[1], Emmanuelle Neumann[1], Anders A. Jensen[3], Solène N. Lefebvre[4], Pierre-Jean Corringer[4], Jacques Neyton[1]*, Christophe Chipot[5,6,7], Francois Dehez[5,6], Guy Schoehn[1] & Hugues Nury[1]*

The serotonin 5-HT_3 receptor is a pentameric ligand-gated ion channel (pLGIC). It belongs to a large family of receptors that function as allosteric signal transducers across the plasma membrane[1,2]; upon binding of neurotransmitter molecules to extracellular sites, the receptors undergo complex conformational transitions that result in transient opening of a pore permeable to ions. 5-HT_3 receptors are therapeutic targets for emesis and nausea, irritable bowel syndrome and depression[3]. In spite of several reported pLGIC structures[4–8], no clear unifying view has emerged on the conformational transitions involved in channel gating. Here we report four cryo-electron microscopy structures of the full-length mouse 5-HT_3 receptor in complex with the anti-emetic drug tropisetron, with serotonin, and with serotonin and a positive allosteric modulator, at resolutions ranging from 3.2 Å to 4.5 Å. The tropisetron-bound structure resembles those obtained with an inhibitory nanobody[5] or without ligand[9]. The other structures include an 'open' state and two ligand-bound states. We present computational insights into the dynamics of the structures, their pore hydration and free-energy profiles, and characterize movements at the gate level and cation accessibility in the pore. Together, these data deepen our understanding of the gating mechanism of pLGICs and capture ligand binding in unprecedented detail.

A decade after the structure of the *Torpedo marmorata* nicotinic acetylcholine receptor[10] (nAChR), the set of known pLGIC structures is rapidly expanding and reflects the diversity of this protein family. The structures share a conserved architecture, in which subunits are arranged around a central five-fold pseudo-symmetry axis. Together they have clarified details of ligand binding, selectivity and allosteric modulation. They have also revealed a complex landscape of conformations, raising questions of how to relate structures to the wealth of data that established the existence of multiple agonist-bound preactive intermediate states[11–13], of distinct open states[14] and of multiple desensitized states[15].

Mouse homomeric 5-HT_{3A} receptors, with their entire intracellular domain (ICD), were solubilized with the detergent C12E9 and purified. We first performed cryo-electron microscopy (cryo-EM) in the presence of the potent antagonist tropisetron, and obtained a 4.5 Å structure (Fig. 1b, Extended Data Figs. 1, 2, Extended Data Table 1), hereafter referred to as T. T is globally similar to the structure previously solved by X-ray crystallography[5] (root mean square deviation (r.m.s.d.) of 0.6 Å), the pore of which was shown by molecular dynamics to be occluded[16]. Tropisetron fits in a peanut-shaped density present in the neurotransmitter pocket (Extended Data Fig. 3d–f). The ICD contains a region of about 60 residues, which is averaged out (also in the other reconstructions, see below) because of its intrinsic flexibility[1,2]. T resembles the 4.5 Å cryo-EM structure of the apo 5-HT_3 receptor[9] (r.m.s.d. of 1.15 Å), with small differences in the lipid-exposed helices M3, MX and M4.

We then sought to identify agonist-elicited conformations of the 5-HT_3 receptor, and performed cryo-EM imaging in the presence of serotonin. A first reconstruction presented heterogeneity in the membrane domain. Further focused 3D classification allowed two subsets of particles to be separated, which yielded reconstructions at 4.2 Å and 4.1 Å resolution, corresponding to two different conformations (Fig. 1b, Extended Data Fig. 4). The maps offer a variable level of information: most side chains in the extracellular domain are resolved, whereas some parts of the transmembrane domain (TMD) do not have side-chain information and some have limited information in the main chain position (Extended Data Figs. 4c, 5), reflecting the receptor dynamics. In the two refined structures, the extracellular domains (ECDs) have undergone an equivalent transition from the T state and serotonin could be modelled in the neurotransmitter site, whereas the TMDs differed markedly (Fig. 2, Extended Data Fig. 6). We call the first structure I1 for intermediate 1 and the second structure F for full, on the basis of the extent of movements compared to the inhibited state. I1 exhibits only limited displacements in the upper part of M1 and M2, and a rearrangement of the M2–M3 loop (Supplementary Video 1). F is characterized by a pronounced reorganization of the transmembrane helices, which can be described by a rigid-body movement of the four-helix bundle coupled to a rearrangement of M4 (and of M3 to a lesser extent) sliding along M1 and M2 (Supplementary Videos 2, 3). F also features a very dynamic ICD, beyond the intrinsically disordered region, in which model building was not possible even though the data showed incomplete densities for MX and M4 (Extended Data Fig. 4a–c).

Finally, we collected a dataset in the presence of serotonin and trans-3-(4-methoxyphenyl)-N-(pentan-3-yl)acrylamide (TMPPAA, a compound exhibiting agonist and positive allosteric modulator activity on the human receptor[17]), a combination that yields weakly desensitizing currents (Extended Data Fig. 1f). From this dataset, we reconstructed a 3.2 Å resolution structure (Extended Data Fig. 2d–g), which provides non-ambiguous side-chain information for nearly the entire receptor. The refined structure has an ECD conformation essentially equivalent to that of I1 and F. The membrane domain is similar to that of I1, albeit with a slightly more expanded top section and pore (Fig. 2). We call this structure I2 for intermediate 2.

Serotonin can be unambiguously positioned in the neurotransmitter site of I2. It fits tightly within its binding pocket (Extended Data Fig. 3a–c) in an orientation consistent with functional and binding studies[1]. Surrounded by obligatory aromatic residues (F199 and Y207 on the principal side, Y126 and W63 on the complementary side), it is positioned to form a cation-π interaction with W156 and hydrogen bonds with the main chain of S155 and Y64. The C loop is positioned moderately inward relative to the inhibited conformations, its position locked by a salt bridge between D202 and R65. A hallmark of allosteric activation is the subunit–subunit rearrangement (Extended Data Fig. 3d), which affects the site volume and geometry.

[1]CNRS, Université Grenoble Alpes, CEA, IBS, Grenoble, France. [2]Theranyx, Marseille, France. [3]Department of Drug Design and Pharmacology, Faculty of Health and Medical Sciences, University of Copenhagen, Copenhagen, Denmark. [4]Channel Receptors Unit, CNRS UMR 3571, Institut Pasteur, Paris, France. [5]Université de Lorraine, CNRS, LPCT, Nancy, France. [6]Laboratoire International Associé CNRS and University of Illinois at Urbana-Champaign, Vandoeuvre-les-Nancy, France. [7]Department of Physics, University of Illinois at Urbana-Champaign, Urbana, IL, USA. *e-mail: jacques.neyton@ibs.fr; hugues.nury@ibs.fr

RESEARCH LETTER

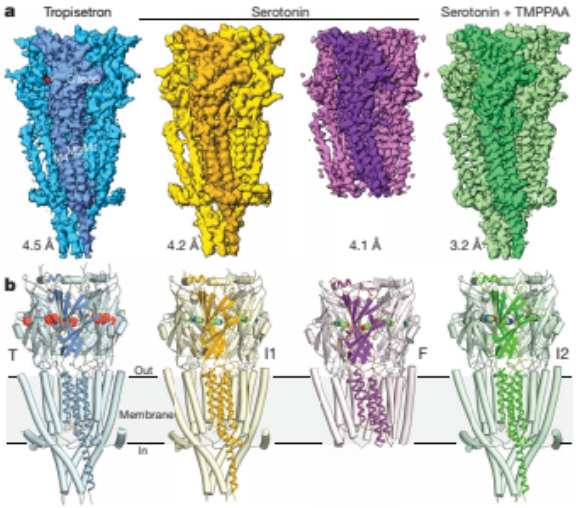

Fig. 1 | Three-dimensional reconstructions and structures of homomeric 5-HT$_{3A}$ receptor. a, **b**, Reconstructions (**a**) and structures (**b**) for: the tropisetron dataset (protein in blue and ligand in red), the serotonin and Ca^{2+} dataset (I1 in yellow, F in purple and ligand in green), and the serotonin and TMPPAA dataset (I2 and ligand in green). Resolutions are shown according to the Fourier shell coefficient 0.143 criterion.

TMPPAA has previously been proposed to bind to an allosteric site in the TMD[17], but there is no clearly interpretable density in our data to model the compound. We tested TMPPAA agonist activity on a set of around 45 single-point mutants of the human receptor, which collectively reveal that the drug binds between M4, M1 and M3 into an intra-subunit cavity skirted by lipids of the outer leaflet in the upper part of the TMD (Extended Data Fig. 7, Supplementary Table 1), where endogenous steroids bind to nAChRs[18]. More generally, several allosteric druggable sites have been identified in pLGICs, which bind diverse compounds including general anaesthetics such as propofol and flavourings such as citral or eucalyptol[3]. Allosteric sites in the 5-HT$_3$ receptor change in both shape and volume during transitions (Extended Data Figs. 3i, 7a).

At the ECD–TMD interface, a set of conserved residues that are essential for gating[19] form a structural motif that is common to all pLGIC structures, the location of which may correlate with the state of the channel[5]. This motif consists of charged residues (E53, D145, E186 and R218) sandwiched between conserved aromatic residues: W187 at the top and the 142-FPF-144 motif of the Cys loop, plus Y223 at the bottom (Extended Data Fig. 8). The FPF motif itself penetrates the transmembrane domain similar to a wedge; its position differs in each conformation. When superimposing structures on a TMD subunit, the wedge lies close to M2 in the tropisetron-bound structure and moves towards M4–M1 in the I1, I2 and F structures (which is possible because the conserved P230 allows the upper M1 to kink or straighten). A marked downward concerted movement of the wedge and of the β8–β9 loop (containing E186 and W187) occurs in the F structure, pushing on the M2–M3 loop, and may be responsible for the marked reorganization of the TMD observed in that state.

pLGIC pores are lined with side chains of residues from the five M2 helices. In direct agreement with results from substituted cysteine accessibility mutagenesis[1] (SCAM), our structures show that in all conformations, positions −1′, 2′, 6′, 9′, 13′, 16′, 17′ and 20′ of the M2 α-helix are exposed to the pore lumen (Fig. 3a). Positions 12′ and 15′, which are also accessible in SCAM, are partly exposed to solvent on the rear of the M2 helices. Superimposition of a single M2 helix underscores its flexibility at both ends; superimposition of the five M2 helices highlights the crucial role of movements of the hydrophobic side chain at the 9′ position (Fig. 3b, c). Minimum pore diameter is often a key element in the assignment of experimental structures to physiological states. Pore profiles are compatible with closed hydrophobic gates (rings at positions 9′, 13′, 16′ and 17′) in the T and I1 structures, with an open channel in the F structure, whereas the I2 structure presents an intermediate profile. However, pore profiles are influenced by the resolution, symmetry and rotameric state of the side chains pointing into the pore lumen. Some positions, such as the key negative charge in −1′ are often poorly resolved in density maps, and are known to adopt alternate conformations[8,20]. Moreover, pore profiles are not informative about hydrophobicity, wetting or dynamics, which have key roles in permeability[21,22]. We performed molecular dynamics simulations to better characterize permeation. In the microsecond-long trajectories starting from the inhibited X-ray structure or from I1, no water or ions cross the pore, and the hydrophobic 9′, 13′ and 16′ rings establish a de-wetted hydrophobic gate that is tighter than in the starting structures (Fig. 3d, Extended Data Fig. 9). By sharp contrast, a simulation starting from F features an open pore that is accessible to ions and water throughout the trajectory (Supplementary Video 4). During the initial part of the simulations starting from I2, when the C_α atoms are positionally restrained, wetting and de-wetting events of the pore occur as if its conformation were on the open–closed verge (Extended Data Fig. 9). Wetting is linked to the presence of transiently hydrated grooves at the back of M2 helices, down to the polar residues Y11′–S12′, affecting the electrostatic landscape inside the pore. Wetting also correlates with rotation of L9′ out of the pore lumen. Once the geometric restraints are removed, the I2 pore relaxes to a closed conformation similar to that observed in the I1 trajectory. The absence of TMPPAA in the simulation may rationalize the closure. Potentials of mean force for the translocation of a K^+ ion reveal an insurmountable 12 kcal mol^{-1} barrier in the case of I1 (representative of closed hydrophobic gate conformations), and an essentially flat free-energy landscape in the case of F (Fig. 3e).

We asked whether the structures could be assigned to physiological states. T and F are straightforward to assign, whereas I1 and I2 are less so. T typifies an inhibited state, with resting-like ECD stabilized by tropisetron, and a closed pore, resembling the apo state. F represents an open state, with an activated ECD with bound serotonin, an activated TMD and a wide open pore. Two assignments are possible for the closely related I1 and I2 conformations (Fig. 4a). In a first scheme, I1 exemplifies a serotonin-bound, pre-active closed state, in which the ECD and the ECD–TMD interface—but not the TMD—have undergone a transition. This is consistent with single-channel analysis of the 5-HT$_3$ receptor, which yields kinetic models in which opening can occur from a ligand-bound pre-active state[14]. In a second scheme, I1 represents a closed desensitized state that occurs downstream from the open state. In both schemes, I2 is best described as in a state close to I1 (that is, close to either pre-active or desensitized) wherein the slightly wider pore promotes wetting, which could enable ion passage or merely favour the switch to a fully open state, consistent with the TMPPAA-induced modulation.

A distinctive feature of the second scheme is that the activation gate, consisting of rings of hydrophobic residues in the upper pore, would open in the active state and close in the desensitized state. This implies a marked movement of the upper pore during desensitization, and no ion access from the extracellular compartment to the lower pore in the desensitized state. Functional experiments on anionic receptors indicate that they have distinct activation and desensitization gates, the latter being located at the cytoplasmic end of the pore[23]. Moreover, structures of the GABA$_A$ receptor β3 homopentamer and of the α4β2 nAChR, with pores constricted at positions −2′ and −1′, have been assigned to desensitized states[6,8]. These receptors, however, were engineered close to the constriction, a feature that can alter desensitization in 5-HT$_3$ receptors[24].

To challenge the two schemes, we measured the movement of the gate region and the accessibility of the pore to organic cations. First, we

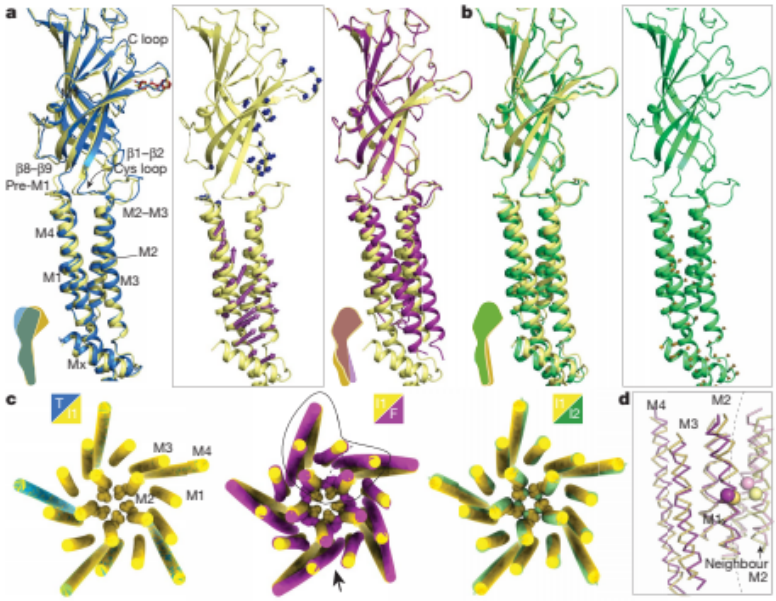

Fig. 2 | Transitions between the tropisetron-bound, the serotonin-bound, and the serotonin and TMPPA-bound states. a, View parallel to the membrane of one subunit of the serotonin-bound conformation I1 (yellow) overlaid with the tropisetron-bound conformation (blue, TMD superposition, left) or with the serotonin-bound conformation F (purple, ECD superposition, right). Inset, vectors indicate the local amplitude of movements, sampled on C_α atoms (T to I1 in blue, I1 to F in purple). **b**, Overlay of the I1 (yellow) and the serotonin and TMPPAA-bound I2 (green) conformations (left); vector representations of the I1 to I2 transition (ECD superposition). **c**, Pairwise overlays of the TMD illustrating transitions at the quaternary level. Structures were superimposed on the ECD pentamer. L9′ (L260) residues are shown as spheres. The line and arrow on the middle overlay indicate the region depicted in **d** and the orientation of the view, respectively. **d**, Tertiary reorganization within a subunit TMD. Overlay in ribbon representation of I2 and F with L260 C_α as spheres (TMD superposition within a single subunit). Note the vertical shift of M3–M4 relative to M1–M2, distortions on the extracellular halves of M1–M2, and interface re-arrangement with the neighbouring subunit helices (on the right of the dotted line).

used voltage-clamp fluorometry (VCF) to probe the local conformational changes in the upper pore at the 19′ position[25,26] (Extended Data Fig. 10). We labelled S19′C mutants, expressed at the surface of *Xenopus laevis* oocytes, with 5-carboxytetramethylrhodamine methanethiosulfonate (MTS-TAMRA). Transient stimulation with serotonin elicited simultaneous changes in current and fluorescence with parallel rise

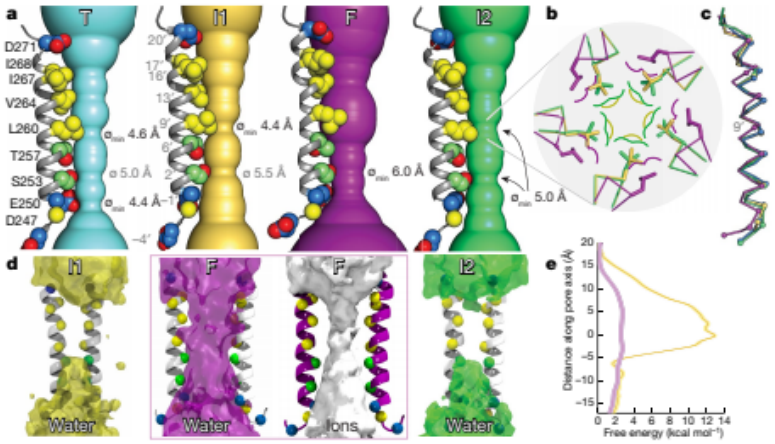

Fig. 3 | Geometry, wetting and energy landscape of the transmembrane pore. a, Static pore geometry; the accessible pathway through the pore is represented as a solid surface for each structure. Diameters (∅) of the constriction zones are noted. One M2 helix is depicted as cartoon with pore-exposed side chains as spheres (polar in green, hydrophobic in yellow, charged in blue). The view is parallel to the plane of the membrane. **b**, Zoom on the hydrophobic gate constriction, formed at the level of L260 (sticks), which has a small movement backward in the I2 state and rotates outwards in the F state. Coloured lines indicate molecular surfaces. The view is perpendicular to the membrane plane. **c**, Superposition of one M2 helix in the four conformations. **d**, Water densities of the pore region during the unrestrained part of simulations. Densities are depicted as transparent surfaces at the same contouring level. The density for K^+ ions is also included for the F trajectory featuring an open pore. **e**, Potentials of mean force of K^+ ions as a function of the position along the pore axis.

RESEARCH LETTER

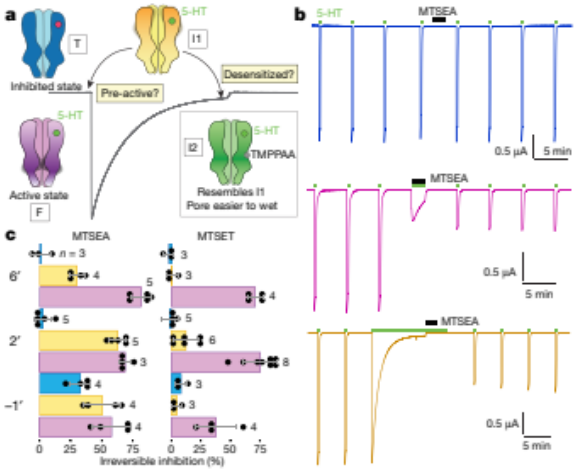

Fig. 4 | Putative molecular mechanisms of operation. a, T (blue) represents an inhibited state, stabilized by tropisetron (red circle). I1 (yellow) represents either a closed pre-active serotonin-bound (green circle) state or a desensitized state. F (purple) represents an open active state. The grey line illustrates the electrical response to serotonin recorded in an oocyte expressing 5-HT_{3A} receptors. **b**, Recordings of MTSEA (1mM) modification on serotonin-evoked current in the S2′C mutant. MTSEA is applied in the resting (blue), the desensitized (orange), or active (purple) state. The protocol includes 10-s test serotonin applications before and after 2-min MTSEA modification. **c**, Changes in current after MTSEA (1 mM) or MTSET (1 mM) modification, for −1′C, S2′C and T6′C mutants, in the resting (blue), active (purple) or desensitized (yellow) state.

and decay, whereas prolonged (7-min) exposure to serotonin resulted in similar signals at the onset, followed by a slow decay for the current signal without a change in fluorescence. Both signals returned to baseline when serotonin was removed. The VCF results argue against the second scheme, because the probe environment changes upon activation but not during desensitization. Second, we performed SCAM in the resting (absence of ligand), open (during transient serotonin application) and desensitized (after prolonged serotonin application) states (Fig. 4b). MTSEA (2-aminoethyl methanethiosulfonate) and MTSET (2-2-(trimethylammonium)ethyl methanethiosulfonate) are organic cations that react with free cysteines through their methanethiosulfonate moiety. The aminoethyl head group of MTSEA is small, which enables it to access narrow spaces. MTSEA is, however, also known to cross membranes in its uncharged form. Application of 1 mM extracellular MTSEA in the resting state yielded no modification of currents in T6′C and S2′C mutants but inhibited currents (by 32%) in E1′C mutants (Fig. 4c). In the resting state, the compound can probably access position −1′ from the internal compartment, but it is unable to access the 2′ or 6′ positions. Similar applications in the open state produced irreversible inhibitions at 6′, 2′ and −1′ positions (82%, 69% and 58%, respectively). MTSEA can therefore reach 6′ and 2′ from the extracellular compartment in the open state, consistent with previous studies[1] and with the opening of the activation gate in F. Applications of extracellular MTSEA in the desensitized state also produced irreversible inhibitions at 6′, 2′ and −1′ positions (30%, 63% and 50%, respectively). From these results, we infer that positions 6′ and 2′, located below the hydrophobic gate seen in T and I1, are accessible from the extracellular side in the desensitized state. No conclusions can be drawn for position −1′, as its labelling in the resting state precludes further interpretation. The results suggest that the activation gate is open in the desensitized conformation(s). MTSET possesses a bulkier trimethylammonium headgroup and cannot cross membranes. We observed that MTSET labels cysteine mutants at 6′, 2′ and −1′ positions when applied in the open state (71%, 75% and 46%, respectively). Application of MTSET in the desensitized state yielded a small variable inhibition at 2′ (12 ± 10%) and none at 6′, indicating that these positions are more accessible for MTSEA than for the bulkier MTSET. On the basis of these results, we favour the scheme in which I1 is assigned to a pre-active state. Nevertheless, desensitization is a complex process involving several distinct states[15], and we cannot rule out the possibility that I1 represents a desensitized state.

The challenge of matching structures to states without ambiguity transcends the present study and pertains to the whole field of pLGIC structures[2,27,28]. This challenge arises from diverse factors: limited resolution, putative influence of detergent, crystal packing and receptor engineering, and the possibility that ensembles of multiple related conformations are necessary to properly depict a physiological state. Bearing in mind the ambiguities on state assignment, we compared the 5-HT_3 transitions to those observed for the *Gloeobacter violaceus* receptor (GLIC)[4], the worm glutamate-gated receptor (GluCl)[29] and the glycine α1 receptor (GlyR)[7]. Common agonist-induced features emerge, such as a global twist, quaternary reorganization of the ECD, rearrangement of the interface between domains involving the conserved sandwich motif, and local movements of the upper TMD. Differences also appear: the extent of TMD reorganization seen in F, with M4 sliding on other helices, is not observed in the other receptors; the ECD reorganization is well-described as 'un-blooming'[4] for GLIC and GluCl, but not for the 5-HT_3 and glycine receptors. The open pore of F is wider than that of GLIC and narrower than that of GlyR. Bacterial, animal anionic and animal cationic channels may have evolved distinct sets of conformations for a given physiological state, as they belong to separate branches of the pLGIC family. Our 5-HT_3 receptor structures highlight several transitions in the cationic branch. They also contribute to knowledge on other important aspects of pLGIC research that are only alluded to in this report, such as the role of M4 in gating, the pharmacology of allosteric sites and ICD dynamics. Further work with better resolution, structures of mutant receptors and structures of receptors in complex with other ligands will complement and increase mechanistic insights, but knowledge of this area may nevertheless remain incomplete until kinetic structural experiments come of age.

Online content

Any methods, additional references, Nature Research reporting summaries, source data, statements of data availability and associated accession codes are available at https://doi.org/10.1038/s41586-018-0672-3.

Received: 7 February 2018; Accepted: 7 September 2018;
Published online: 31 October 2018

1. Thompson, A. J., Lester, H. A. & Lummis, S. C. R. The structural basis of function in Cys-loop receptors. *Q. Rev. Biophys.* **43**, 449–499 (2010).
2. Nemecz, Á., Prevost, M. S., Menny, A. & Corringer, P.-J. Emerging molecular mechanisms of signal transduction in pentameric ligand-gated ion channels. *Neuron* **90**, 452–470 (2016).
3. Sparling, B. A. & DiMauro, E. F. Progress in the discovery of small molecule modulators of the Cys-loop superfamily receptors. *Bioorg. Med. Chem. Lett.* **27**, 3207–3218 (2017).
4. Sauguet, L. et al. Crystal structures of a pentameric ligand-gated ion channel provide a mechanism for activation. *Proc. Natl Acad. Sci. USA.* **111**, 966–971 (2014).
5. Hassaïne, G. et al. X-ray structure of the mouse serotonin 5-HT_3 receptor. *Nature* **512**, 276–281 (2014).
6. Miller, P. S. & Aricescu, A. R. Crystal structure of a human $GABA_A$ receptor. *Nature* **512**, 270–275 (2014).
7. Du, J., Lü, W., Wu, S., Cheng, Y. & Gouaux, E. Glycine receptor mechanism elucidated by electron cryo-microscopy. *Nature* **526**, 224–229 (2015).
8. Morales-Perez, C. L., Noviello, C. M. & Hibbs, R. E. X-ray structure of the human α4β2 nicotinic receptor. *Nature* **538**, 411–415 (2016).
9. Basak, S. et al. Cryo-EM structure of 5-HT_{3A} receptor in its resting conformation. *Nat. Commun.* **9**, 514 (2018).
10. Unwin, N. Refined structure of the nicotinic acetylcholine receptor at 4 Å resolution. *J. Mol. Biol.* **346**, 967–989 (2005).
11. Mukhtasimova, N., Lee, W., Wang, H. & Sine, S. Detection and trapping of intermediate states priming nicotinic receptor channel opening. *Nature* **459**, 451–454 (2009).
12. Lape, R., Colquhoun, D. & Sivilotti, L. G. On the nature of partial agonism in the nicotinic receptor superfamily. *Nature* **454**, 722–727 (2008).
13. Menny, A. et al. Identification of a pre-active conformation of a pentameric channel receptor. *eLife* **6**, e23955 (2017).
14. Corradi, J., Gumilar, F. & Bouzat, C. Single-channel kinetic analysis for activation and desensitization of homomeric 5-HT_{3A} receptors. *Biophys. J.* **97**, 1335–1345 (2009).
15. Sakmann, B., Patlak, J. & Neher, E. Single acetylcholine-activated channels show burst-kinetics in presence of desensitizing concentrations of agonist. *Nature* **286**, 71–73 (1980).
16. Trick, J. L. et al. Functional annotation of ion channel structures by molecular simulation. *Structure* **6**, 2207–2216 (2016).
17. Gasiorek, A. et al. Delineation of the functional properties and the mechanism of action of TMPPAA, an allosteric agonist and positive allosteric modulator of 5-HT_3 receptors. *Biochem. Pharmacol.* **110–111**, 92–108 (2016).
18. Jin, X. & Steinbach, J. H. A portable site: a binding element for 17β-estradiol can be placed on any subunit of a nicotinic α4β2 receptor. *J. Neurosci.* **31**, 5045–5054 (2011).
19. Mukhtasimova, N. & Sine, S. M. Nicotinic receptor transduction zone: invariant arginine couples to multiple electron-rich residues. *Biophys. J.* **104**, 355–367 (2013).
20. Cymes, G. D. & Grosman, C. The unanticipated complexity of the selectivity-filter glutamates of nicotinic receptors. *Nat. Chem. Biol.* **8**, 975–981 (2012).
21. Zhu, F. & Hummer, G. Drying transition in the hydrophobic gate of the GLIC channel blocks ion conduction. *Biophys. J.* **103**, 219–227 (2012).
22. Aryal, P., Sansom, M. S. P. & Tucker, S. J. Hydrophobic gating in ion channels. *J. Mol. Biol.* **427**, 121–130 (2015).
23. Gielen, M., Thomas, P. & Smart, T. G. The desensitization gate of inhibitory Cys-loop receptors. *Nat. Commun.* **6**, 6829 (2015).
24. McKinnon, N. K., Bali, M. & Akabas, M. H. Length and amino acid sequence of peptides substituted for the 5-HT_{3A} receptor M3M4 loop may affect channel expression and desensitization. *PLoS ONE* **7**, e35563 (2012).
25. Pless, S. A., Dibas, M. I., Lester, H. A. & Lynch, J. W. Conformational variability of the glycine receptor M2 domain in response to activation by different agonists. *J. Biol. Chem.* **282**, 36057–36067 (2007).
26. Dahan, D. S. et al. A fluorophore attached to nicotinic acetylcholine receptor βM2 detects productive binding of agonist to the αδ site. *Proc. Natl Acad. Sci. USA* **101**, 10195–10200 (2004).
27. daCosta, C. J. B. & Baenziger, J. E. Gating of pentameric ligand-gated ion channels: structural insights and ambiguities. *Structure* **21**, 1271–1283 (2013).
28. Gonzalez-Gutierrez, G., Wang, Y., Cymes, G. D., Tajkhorshid, E. & Grosman, C. Chasing the open-state structure of pentameric ligand-gated ion channels. *J. Gen. Physiol.* **149**, 1119–1138 (2017).
29. Hibbs, R. E. & Gouaux, E. Principles of activation and permeation in an anion-selective Cys-loop receptor. *Nature* **474**, 54–60 (2011).

Acknowledgements We acknowledge access to the C-CINA and ESRF Krios microscopes, and thank M. Chami, L. Kovacik, H. Stahlberg, G. Effantin, E. Kandiah and M. Hons for support. We thank L. Estrozi, M. Bacia, G. Effantin and A. Desfosses for advice on cryo-EM; the Vivaudou and Moreau laboratories for providing high-quality oocytes and help with electrophysiology; members of the Nury laboratory, M. Gielen and E. Pebay-Peyroula for discussions. The work was funded by the Marie Curie CIG NeuroPenta and ERC Starting grant 637733 (to H.N.). It used the platforms of the Grenoble Instruct-ERIC Center (ISBG: UMS 3518 CNRS-CEA-UGA-EMBL) with support from FRISBI (ANR-10 INSB-05-02) and GRAL (ANR-10-LABX-49-01) within the Grenoble PSB. The electron microscopy facility is supported by the Rhône-Alpes Region, the FRM, the FEDER and the GIS-IBISA.

Reviewer information *Nature* thanks S. Sine, A. Sobolevsky and the other anonymous reviewer(s) for their contribution to the peer review of this work.

Author contributions L.P., J.P. and G.H. performed sample preparation. L.P., H.N, E.N. and G.S. optimized and collected microscopy data. L.P. and H.N. built the models. F.D. and C.C. conducted molecular dynamics simulations. J.N. performed electrophysiology experiments. S.N.L. and P.-J.C. performed VCF experiments. A.A.J. performed FLIPR experiments. All authors extensively discussed the data, H.N. and J.N. wrote the manuscript with inputs from all authors.

Competing Interests G.H. is employed by Theranyx. The remaining authors declare no competing interests.

Additional information
Extended data is available for this paper at https://doi.org/10.1038/s41586-018-0672-3.
Supplementary information is available for this paper at https://doi.org/10.1038/s41586-018-0672-3.
Reprints and permissions information is available at http://www.nature.com/reprints.
Correspondence and requests for materials should be addressed to J.N. or H.N.
Publisher's note: Springer Nature remains neutral with regard to jurisdictional claims in published maps and institutional affiliations.

RESEARCH LETTER

METHODS

No statistical methods were used to predetermine sample size. The experiments were not randomized. The investigators were not blinded to allocation during experiments and outcome assessment.

Protein expression. The wild-type mouse 5-HT_{3A} receptor was expressed in a stable, inducible cell line derived from HEK T-REx 293 cells (Thermo Fisher), as previously described[5,30,31]. The cells were cultured in suspension in flasks in an orbital incubator (typical culture size, 5 l). The protein expression was induced when cells reached 2×10^6 cells/ml. Valproic acid was added one day later and cells were cultured for one more day. Cells were then pelleted by low-speed centrifugation, frozen and stored at −80°C.

Protein purification. In a typical purification batch, 20 g of cells were resuspended in buffer A (10 mM HEPES pH 7.4, 1 mM EDTA, antiprotease cocktail; 10 ml buffer per gram of cells) mechanically lysed (Ultraturrax T20, 6 × 30 s) and membranes were collected by ultracentrifugation (100,000*g* for 1 h). All steps were carried out at 4 °C. Membranes were resuspended in buffer B (50 mM Tris pH 8, 500 mM NaCl, antiprotease cocktail, 25 ml buffer per gram of membrane) and the solution was supplemented with 0.15% of C12E9 for solubilisation using gentle stirring (1.5 h). The insoluble material was removed by ultracentrifugation (100,000*g* for 45 min). Solubilized proteins were purified by affinity chromatography using gravity flow Strep-Tactin resin (IBA, typically 25 ml resin), eluted in buffer C (50 mM Tris pH 7.5, 125 mM NaCl, 0.01% C12E9) and concentrated to ~0.5 mg/ml using Millipore 100-kDa cut-off filters. The purification tag was cleaved, and carbohydrates were digested by addition of 0.04 mg TEV protease and 0.1 mg PNGase F per 1 mg protein with gentle stirring overnight. The protein was further concentrated and then applied to a Superose 6 column (GE healthcare) equilibrated in buffer C.

Electron microscopy. The most homogeneous fractions of 5-HT_3 receptor following size-exclusion chromatography were concentrated to ~1.5 mg/ml (in the best cases, no concentration was required). The sample was mixed with lipids (0.01% phosphatidic acid, 0.01% cholesterol hemisuccinate, 0.01% brain phosphatidylcholine; Avanti Polar Lipids) and ligands: 2 mM tropisetron (Tocris), or 50 μM serotonin and 2 mM calcium (conditions known to promote fast desensitization[32,33]); or 30 μM serotonin and 100 mM TMPPAA (Sigma-Aldrich). Samples were incubated for 10–30 min on ice. 3.5 μl were deposited on a glow-discharged (30 mA, 50 s) Quantifoil copper-rhodium 1.2/1.3 grid, blotted for 10 s at force 0 using a Mark IV Vitrobot and plunge-frozen in liquid ethane. Between four and ten grids were screened during each data collection, as ice thickness varied between grids. Optimization was performed on an in-house Polara electron microscope. Datasets were recorded on Titan Krios electron microscopes with K2 cameras at C-CINA (Basel) or at the ESRF (Grenoble). Details of data collections are shown in Extended Data Table 1.

Image processing. At the Basel Krios microscope, the data collection was monitored online and good images were selected using Focus[34]; images were acquired in super-resolution mode and binned by Fourier-space cropping during the drift correction. At the ESRF Krios microscope, the counted mode was used. Drift was corrected with MotionCor2[35] and dose-weighted sums were used for subsequent processing, except for CTF correction, which was performed using GCTF[36] on non-dose-weighted sums. Picking was performed with Gautomatch (http://www.mrc-lmb.cam.ac.uk/kzhang/Gautomatch/) using average from 2D classes as templates. Subsequent steps were performed using Relion[37] on a GPU workstation. Typically, two rounds of 2D classifications with 20–30 classes were performed, followed by a round of 3D classification without imposing symmetry (3–6 classes) with a low-pass-filtered initial model of the receptor. Particles presenting five-fold symmetry were selected, submitted to 3D classifications (classifications and data processing are further described in Extended Data Figs. 2, 4) and the best sets of particles were subjected to 3D auto-refinement. In the post-processing step, a soft mask was calculated and applied to the two half maps before the Fourier shell coefficient (FSC) was calculated. Map sharpening (*B*-factor fixed at −100 $Å^2$ for I1 and F, automatic estimation for T and I2) was also performed in the post-processing step. We tried the Phenix auto-sharpen program[38], which improved only the F map. The quality of the final reconstructions is shown in Extended Data Fig. 5.

Model refinement and structure analysis. Refinement was performed with the Phenix suite[39]. Cycles of real-space refinement were performed using global minimization, rigid body fit and local rotamer fitting (and *B*-factor refinement in late stages), alternating with manual rebuilding in Coot[40]. NCS and secondary structure restraints were enabled. The 4 models comprise residues 10–307 and 426–460. T, I1 and I2 also have MX and MA residues 308–330 and 399–426, which—owing to flexibility—could not be built in F. Tropisetron (numbered 902) was placed in the orthosteric side of T, and serotonin (numbered 901) was placed in the site of I1, F and I2. The densities for serotonin in I1 and F enable the ligand to be placed in several equivalent orientations, and we used the unambiguous density in I2 to choose the same ligand pose in these 3 structures. The stereochemical properties of the final models, analysed with the Molprobity server (http://molprobity.biochem.duke.edu/), are reported in Extended Data Table 1. Pore profiles were plotted using HOLE[41], r.m.s.d. values were calculated with 'superpose' in the CCP4 suite[42]. Figures were prepared with the PyMOL Molecular Graphics System (Schrodinger), Chimera[43] or CueMol.

Molecular dynamics. Molecular assays were built for the four conformational states of 5-HT_3 described in the manuscript. For F, I1 and I2, we used the reported cryo-EM structures, whereas for the inhibited conformation we used the crystal structure (RCSB Protein Data Bank code (PDB): 4PIR) because of its higher resolution. The co-crystallized nanobodies were removed and the protein was modelled without serotonin. The five serotonins present in F, I1 and I2 structures were kept in the models. For I2, because no obvious densities were observed for TMPPAA, it was not represented in the model. The intracellular domain of the F conformation (not resolved in the cryo-EM density) was not included in the model.

Using the CHARMM-GUI web interface[44,45], each structure was embedded in a fully hydrated palmitoyl-oleyl-phosphatidylcholine (POPC) bilayer consisting of around 240 lipid units and about 30,000 for F and 42,000 water molecules for T, I1 and I2. K^+Cl^- (150 mM) was explicitly added to each system, while ensuring their electric neutrality. The all-atom CHARMM36 force field[46] and revision thereof for lipids[47] were used to describe the system and CMAP corrections were introduced for the protein[48]. For water, we used the TIP3P model[49]. A subset of mass of the heavy atoms of lipids, protein and serotonin were transferred on the hydrogens atoms to which they are bound, to reach a hydrogen mass of 3.024 Da. Using such a mass repartitioning scheme, the equation of motions can be integrated with a time step of up to 4 fs without modifying the dynamics and thermodynamics of the system[50].

All simulations were carried out with the NAMD package v.2.12[51]. Simulations were performed in the isothermal–isobaric ensemble at $T = 300$K and $P = 1$ atm with anisotropic scaling of the simulation cell[52], long-range electrostatic interactions were treated with the particle-mesh Ewald method[53], and short-range electrostatics and Lennard-Jones interactions were smoothly truncated. The equations of motion were integrated with a time step of 4 and 8 fs for short- and long-range forces, respectively, using the Verlet r-RESPA multiple time-step propagator[54]. Covalent bonds involving hydrogen atoms were constrained to their equilibrium length by means of the 'rattle/shake algorithm'[55,56] and the 'settle' algorithm was used for water[57]. For each system, a smooth equilibration along which the positions of the heavy atoms of the protein were restrained harmonically, was carried out for 60 ns. After releasing the restraints, the simulations were extended up to 1 μs. All analyses and molecular rendering were achieved with VMD[58]. Pore radii were inferred using the program HOLE[41].

The potentials of mean force underlying the translocation of a potassium ion in the I1 and F conformations of the 5-HT_3 receptor were determined using a multiple-walker version[59] of the adaptive biasing force algorithm[60]. For the I1 conformation, the reaction coordinate model was chosen as the Euclidian distance between the ion and the centre of mass of the protein, projected onto its longitudinal axis; that is, the *z*-direction of Cartesian space. In the case of the F conformation, a two-dimensional free-energy landscape was generated, exploring ion diffusion in the pore not only longitudinally by means of the aforementioned projected Euclidian distance, but also radially. The potential of mean force along the pore was recovered by integration of the marginal law in the radial direction. The reaction pathway was broken down into 14 and 12 windows for the I1 and F conformations, respectively. The free-energy landscapes were explored by four walkers, syncing gradients every 500 molecular-dynamics steps. The total simulation time for the I1 and F conformations amounted to 2.16 and 3.04 μs, respectively, wherein the last 0.8 μs was used to estimate the error bars associated with the potentials of mean force, based on an independent mapping of the free-energy landscape by the walkers.

Electrophysiology. Electrical recordings were obtained by two-electrode voltage-clamp (TEVC) on *Xenopus* oocytes expressing either wild-type or mutated homomeric mouse 5-HT_{3A} receptors. Mutants were obtained using the QuickChange Lightning (Stratagene) site-directed mutagenesis kit and oligonucleotides (Supplementary Table 2) to introduce point mutations into the pcDNA5/TO-m5-HT_{3A} plasmid. All the mutations were verified by sequencing.

Oocytes were prepared as previously reported[61] using procedures that conformed to European regulations for animal handling and experiments, and were approved by governmental services (authorization no. D 38 185 10 001 for the animal facility delivered by the Prefect of Isère) and the Institutional Ethics Committee (ethics approval N° 12-040 granted to C. Moreau by the Ethics Committee of Commissariat à l'Energie Atomique et aux Energies Alternatives). Difolliculated oocytes were injected with 30 nl plasmid DNA (1–10 ng/μl) coding for the desired 5-HT_{3A} subunit (subcloned into pcDNA5 vector). Microinjected oocytes were incubated for 1 to 5 days at 19 °C in Barth's solution (in mM: 1 KCl, 0.82 $MgSO_4$, 88 NaCl, 2.4 $NaHCO_3$, 0.41 $CaCl_2$, 16 HEPES, pH 7.4) supplemented with 100 U ml^{-1} penicillin and streptomycin.

Whole-cell TEVC recordings were obtained using an OC-725C Oocyte Clamp amplifier (Warner Instruments) at a constant holding potential of −50 mV.

Macroscopic currents were filtered at 1 kHz, digitized at 2 kHz with a Digidata 1440 analogue-to-digital interface and analysed with Clampfit (Molecular Devices). During the recordings, oocytes were constantly perfused with a 0 Ca-ND96 solution (containing in mM: 91 NaCl, 2 KCl, 1 $MgCl_2$, 5 HEPES, 1 EGTA, pH 7.4) at a rate of 1.3 ml/min, which allowed the application of serotonin and other compounds in a time range of seconds (20-fold concentration change of applied compounds in 5 s). Throughout this study, electrophysiological responses were induced by 10 μM serotonin (a saturating dose for all tested constructions, not shown) and peaked in less than 3 s. In all constructions tested, 10-min applications of serotonin induced almost complete desensitization (to less than 3% of the peak current with $t_{1/2}$ in the min range). Full recovery of desensitization was observed after washing serotonin for 10 min. Ca^{2+} ions are permeant through 5-HT_3 receptors[62]. Calcium was therefore carefully removed from the recording perfusion solution to avoid contamination of the serotonin-induced responses by endogenous oocyte current secondarily activated by Ca^{2+} ions entering the oocyte through the serotonin receptors.

MTSEA (2-aminoethyl methanethiosulfonate bromide) and MTSET (2-trimethylammonium-ethyl methanethiosulfonate bromide) were purchased from Interchim and prepared immediately before perfusion from stock solutions in water stored at −20 °C. The effect of MTS compounds on pore cysteine-mutants was studied using the following protocol: (i) checking stability of the response with a train of three to five applications of 10 μM serotonin for 10 s, every 5 min (I_{pre}); (ii) applying MTS compounds for 2 min at 1 mM, either in the absence of 5-HT (to probe cysteine accessibility in the resting state), simultaneously with 10 μM 5-HT (to probe the open state) or simultaneously with 10 μM 5-HT after a 10 min pre-application of 5-HT alone allowing for complete desensitization; (iii) following the effect of MTS compounds during a second set of five applications of 5-HT for 10 s every 5 min (I_{post}). Irreversible effects of MTS compounds were quantified by measuring I_{post} 25 min after removal of the MTS compound. The percentage of inhibition or potentiation was calculated as $(I_{pre}-I_{post})/I_{pre} \times 100$. MTS compounds (applied at 1 mM simultaneously with 10 μM serotonin) have no detectable effect on wild-type receptors (not shown).

Voltage-clamp fluorometry. VCF recordings were performed on *Xenopus* oocytes provided by Ecocyte Bioscience that were injected with 50 ng/μl plasmid DNA encoding for the mouse 5-HT_{3A} receptor S19′C mutant, after 2 to 6 days of expression in Barth solution at 17 °C. They were labelled with MTS-TAMRA (Toronto Chemicals) for 5 min at 17 °C in ND96 buffer without $CaCl_2$ containing 10 μM 5-hydroxytryptamine (5-HT), then rinsed and stored at 17 °C for up to 4 h before recording in ND96. Recording were made in a TEVC setup as described[13], adapted for fluorescence recording. In brief, recordings were made with a VCF dedicated chamber with only a fraction of the oocyte perfused and illuminated by a LED (coolLED PE-4000). Light was collected using a fluorescence microscope (Zeiss Axiovert135) equipped with a 40× objective (Plan Neofluar), a TRITC filter set and a photomultiplier tube (Hamamatsu Photonics). Recordings were made at −60 mV clamp, 500-Hz sampling rate with a 550-nm excitation wavelength. Data were filtered, corrected for baseline and photobleaching where necessary, and analysed using pClamp and Axograph. Dose–response curves were fitted using Prism to the Hill equation: $I/I_{max} = 1/(1 + (EC_{50}/[5\text{-HT}])^{nH})$ in which I is the response at a given [5-HT] (serotonin concentration), I_{max} is the maximal response, EC_{50} is half maximal effective concentration and nH is the Hill coefficient. Serotonin dose–response relations were shifted to the left with half-responses for fluorescence and current at 40 and 240 nM, respectively (the EC_{50} of the wild-type receptor is 800 nM).

Fluorescence imaging plate reader membrane potential blue assay. The agonist properties of 5-HT and TMPPAA (Sigma-Aldrich) were characterized at human wild-type or mutant 5-HT_{3A} receptors transiently expressed in tsA201 cells in the fluorescence imaging plate reader (FLIPR) membrane potential blue (FMP; fluoresence-based membrane potential) assay. The generation of some of the human 5-HT_{3A} mutants have previously been described[63]. Other mutants were constructed by introduction of point mutations into the h5-HT3A-pCIneo plasmid using Quikchange II XL site-directed mutagenesis (Stratagene) and oligonucleotides (TAG Copenhagen). The absence of unwanted mutations in all cDNAs created by PCR was verified by sequencing (Eurofins MWG Operon). The cells were cultured in Dulbecco's Modified Eagle Medium supplemented with penicillin (100 U/ml), streptomycin (100 mg/ml) and 10% fetal bovine serum in a humidified atmosphere of 5% CO_2 and 95% air at 37 °C. Cells (1.2×10^6) were split into a 6-cm tissue culture plate, transfected the following day with 4 μg cDNA (wild-type or mutant h5-HT3A-pCIneo) using Polyfect (Qiagen) as transfection reagent, and split into poly-D-lysine-coated black 96-well plates (8×10^4 cells per well) with clear bottom (BD Biosciences) the following day. After 20–24 h following transfection, the medium was aspirated, and the cells were washed with 100 μl Krebs buffer (140 mM NaCl, 4.7 mM KCl, 2.5 mM $CaCl_2$, 1.2 mM $MgCl_2$, 11 mM HEPES, 10 mM D-glucose, pH 7.4). Then 100 μl Krebs buffer supplemented with 0.5 mg/ml FMP assay dye (Molecular Devices) was added to each well, and the 96-well plate was assayed at 37 °C in a FLEXStation3 Benchtop Multi-Mode Microplate Reader (Molecular Devices) measuring emission (in fluorescence units (FU)) at 565 nm caused by excitation at 530 nm before and up to 90 s after addition of 33.3 μl assay buffer supplemented with agonist (5-HT or TMPPAA). The experiments were performed in duplicate at least three times for each agonist at all receptors. Concentration–response curves for the agonists were constructed based on the difference in the fluorescence units (rFU) between the maximal fluorescence recording made before and after addition of the agonists at different concentrations. The curves were generated by non-weighted least-squares fits using the program KaleidaGraph (Synergy Software).

Reporting summary. Further information on research design is available in the Nature Research Reporting Summary linked to this paper.

Data availability

Atomic coordinates of the four conformations have been deposited in the Protein Data Bank with accession numbers 6HIN, 6HIO, 6HIQ and 6HIS for conformations F, I1, I2 and T, respectively. The cryo-EM density maps have been deposited in the Electron Microscopy Data Bank with accession numbers EMD-0225, EMD-0226, EMD-0227 and EMD-0228 for conformations F, I1, I2 and T, respectively.

30. Hassaïne, G. et al. Large scale expression and purification of the mouse 5-HT_3 receptor. *BBA Biomembranes* **1828**, 2544–2552 (2013).
31. Hassaïne, G. et al. Expression, biochemistry, and stabilization with camel antibodies of membrane proteins: case study of the mouse 5-HT_3 receptor. *Methods Mol. Biol.* **1635**, 139–168 (2017).
32. Yakel, J. L., Lagrutta, A., Adelman, J. P. & North, R. A. Single amino acid substitution affects desensitization of the 5-hydroxytryptamine type 3 receptor expressed in *Xenopus* oocytes. *Proc. Natl Acad. Sci. USA* **90**, 5030–5033 (1993).
33. Hu, X.-Q. & Lovinger, D. M. Role of aspartate 298 in mouse 5-HT_{3A} receptor gating and modulation by extracellular Ca^{2+}. *J. Physiol. (Lond.)* **568**, 381–396 (2005).
34. Biyani, N. et al. Focus: The interface between data collection and data processing in cryo-EM. *J. Struct. Biol.* **198**, 124–133 (2017).
35. Zheng, S. Q. et al. MotionCor2: anisotropic correction of beam-induced motion for improved cryo-electron microscopy. *Nat. Methods* **14**, 331–332 (2017).
36. Zhang, K. Gctf: Real-time CTF determination and correction. *J. Struct. Biol.* **193**, 1–12 (2016).
37. Scheres, S. H. W. RELION: implementation of a Bayesian approach to cryo-EM structure determination. *J. Struct. Biol.* **180**, 519–530 (2012).
38. Terwilliger, T. C., Sobolev, O. V., Afonine, P. V. & Adams, P. D. Automated map sharpening by maximization of detail and connectivity. *Acta Crystallogr. D* **74**, 545–559 (2018).
39. Adams, P. D. et al. PHENIX: a comprehensive Python-based system for macromolecular structure solution. *Acta Crystallogr. D* **66**, 213–221 (2010).
40. Emsley, P., Lohkamp, B., Scott, W. G. & Cowtan, K. Features and development of Coot. *Acta Crystallogr. D* **66**, 486–501 (2010).
41. Smart, O. S., Neduvelil, J. G., Wang, X., Wallace, B. A. & Sansom, M. S. HOLE: a program for the analysis of the pore dimensions of ion channel structural models. *J. Mol. Graph.* **14**, 354–360 (1996).
42. Winn, M. D. et al. Overview of the CCP4 suite and current developments. *Acta Crystallogr. D* **67**, 235–242 (2011).
43. Pettersen, E. F. et al. UCSF Chimera—a visualization system for exploratory research and analysis. *J. Comput. Chem.* **25**, 1605–1612 (2004).
44. Jo, S., Kim, T., Iyer, V. G. & Im, W. CHARMM-GUI: a web-based graphical user interface for CHARMM. *J. Comput. Chem.* **29**, 1859–1865 (2008).
45. Wu, E. L. et al. CHARMM-GUI Membrane Builder toward realistic biological membrane simulations. *J. Comput. Chem.* **35**, 1997–2004 (2014).
46. MacKerell, A. D. et al. All-atom empirical potential for molecular modeling and dynamics studies of proteins. *J. Phys. Chem. B* **102**, 3586–3616 (1998).
47. Klauda, J. B. et al. Update of the CHARMM all-atom additive force field for lipids: validation on six lipid types. *J. Phys. Chem. B* **114**, 7830–7843 (2010).
48. Best, R. B. et al. Optimization of the additive CHARMM all-atom protein force field targeting improved sampling of the backbone ϕ, ψ and side-chain $\chi 1$ and $\chi 2$ dihedral angles. *J. Chem. Theory Comput.* **8**, 3257–3273 (2012).
49. Jorgensen, W. L., Chandrasekhar, J., Madura, J. D., Impey, R. W. & Klein, M. L. Comparison of simple potential functions for simulating liquid water. *J. Chem. Phys.* **79**, 926–935 (1983).
50. Hopkins, C. W., Le Grand, S., Walker, R. C. & Roitberg, A. E. Long-time-step molecular dynamics through hydrogen mass repartitioning. *J. Chem. Theory Comput.* **11**, 1864–1874 (2015).
51. Phillips, J. C. et al. Scalable molecular dynamics with NAMD. *J. Comput. Chem.* **26**, 1781–1802 (2005).
52. Feller, S. E., Zhang, Y., Pastor, R. W. & Brooks, B. R. Constant pressure molecular dynamics simulation: the Langevin piston method. *J. Chem. Phys.* **103**, 4613–4621 (1995).
53. Darden, T., York, D. & Pedersen, L. Particle mesh Ewald: an *N*·log(*N*) method for Ewald sums in large systems. *J. Chem. Phys.* **98**, 10089–10092 (1993).
54. Tuckerman, M., Berne, B. J. & Martyna, G. J. Reversible multiple time scale molecular dynamics. *J. Chem. Phys.* **97**, 1990–2001 (1992).
55. Ryckaert, J.-P., Ciccotti, G. & Berendsen, H. J. C. Numerical integration of the cartesian equations of motion of a system with constraints: molecular dynamics of *n*-alkanes. *J. Comput. Phys.* **23**, 327–341 (1977).
56. Andersen, H. C. Rattle: A 'velocity' version of the shake algorithm for molecular dynamics calculations. *J. Comput. Phys.* **52**, 24–34 (1983).

57. Miyamoto, S. & Kollman, P. A. Settle: an analytical version of the SHAKE and RATTLE algorithm for rigid water models. *J. Comput. Chem.* **13**, 952–962 (1992).
58. Humphrey, W., Dalke, A. & Schulten, K. VMD: visual molecular dynamics. *J. Mol. Graph.* **14**, 33–38 (1996).
59. Comer, J., Phillips, J. C., Schulten, K. & Chipot, C. Multiple-replica strategies for free-energy calculations in NAMD: multiple-walker adaptive biasing force and walker selection rules. *J. Chem. Theory Comput.* **10**, 5276–5285 (2014).
60. Comer, J. et al. The adaptive biasing force method: everything you always wanted to know but were afraid to ask. *J. Phys. Chem. B* **119**, 1129–1151 (2015).
61. Moreau, C. J., Niescierowicz, K., Caro, L. N., Revilloud, J. & Vivaudou, M. Ion channel reporter for monitoring the activity of engineered GPCRs. *Methods Enzymol.* **556**, 425–454 (2015).
62. Yang, J. Ion permeation through 5-hydroxytryptamine-gated channels in neuroblastoma N18 cells. *J. Gen. Physiol.* **96**, 1177–1198 (1990).
63. Trattnig, S. M. et al. Discovery of a novel allosteric modulator of 5-HT_3 receptors: inhibition and potentiation of Cys-loop receptor signaling through a conserved transmembrane intersubunit site. *J. Biol. Chem.* **287**, 25241–25254 (2012).
64. Suryanarayanan, A. et al. The loop C region of the murine 5-HT_{3A} receptor contributes to the differential actions of 5-hydroxytryptamine and *m*-chlorophenylbiguanide. *Biochemistry* **44**, 9140–9149 (2005).
65. Yan, D., Schulte, M. K., Bloom, K. E. & White, M. M. Structural features of the ligand-binding domain of the serotonin 5HT_3 receptor. *J. Biol. Chem.* **274**, 5537–5541 (1999).
66. Ruepp, M.-D., Wei, H., Leuenberger, M., Lochner, M. & Thompson, A. J. The binding orientations of structurally-related ligands can differ; a cautionary note. *Neuropharmacology* **119**, 48–61 (2017).
67. Kesters, D. et al. Structural basis of ligand recognition in 5-HT_3 receptors. *EMBO Rep.* **14**, 49–56 (2013).
68. Hibbs, R. E. et al. Structural determinants for interaction of partial agonists with acetylcholine binding protein and neuronal α7 nicotinic acetylcholine receptor. *EMBO J.* **28**, 3040–3051 (2009).
69. Spurny, R. et al. Pentameric ligand-gated ion channel ELIC is activated by GABA and modulated by benzodiazepines. *Proc. Natl Acad. Sci. USA* **109**, E3028–E3034 (2012).
70. Delbart, F. et al. An allosteric binding site of the α7 nicotinic acetylcholine receptor revealed in a humanized acetylcholine-binding protein. *J. Biol. Chem.* **293**, 2534–2545 (2018).
71. Steward, L. J. et al. Importance of phenylalanine 107 in Agonist recognition by the 5-hydroxytryptamine$_{3A}$ receptor. *Mol. Pharmacol.* **57**, 1249–1255 (2000).
72. Purohit, P. & Auerbach, A. Acetylcholine receptor gating at extracellular transmembrane domain interface: the 'pre-M1' linker. *J. Gen. Physiol.* **130**, 559–568 (2007).
73. Lee, W. Y. & Sine, S. M. Principal pathway coupling agonist binding to channel gating in nicotinic receptors. *Nature* **438**, 243–247 (2005).
74. Hu, X.-Q., Zhang, L., Stewart, R. R. & Weight, F. F. Arginine 222 in the pre-transmembrane domain 1 of 5-HT_{3A} receptors links agonist binding to channel gating. *J. Biol. Chem.* **278**, 46583–46589 (2003).

LETTER RESEARCH

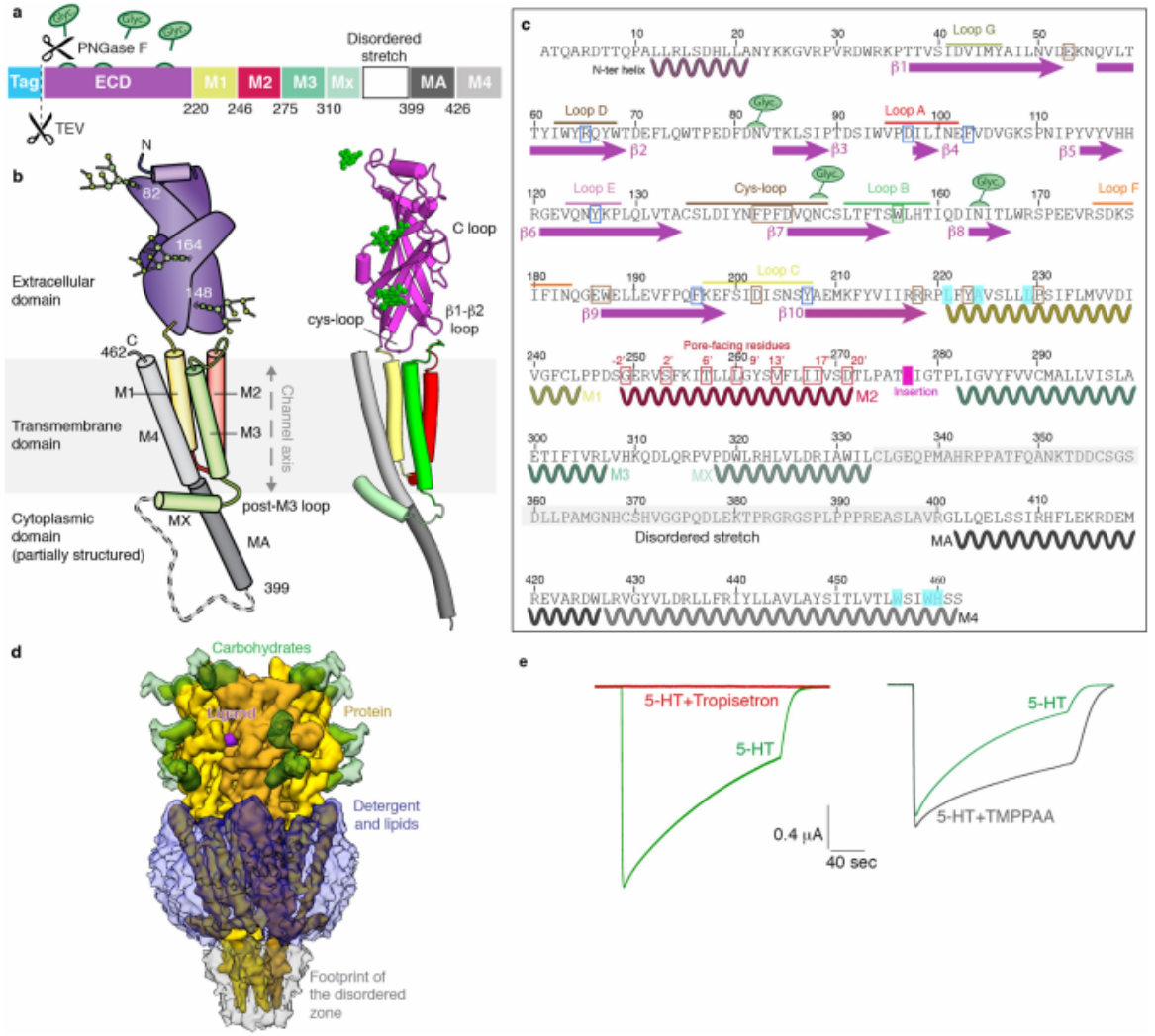

Extended Data Fig. 1 | 5-HT$_3$ receptor topology and sequence. **a**, Schematic of the full-length 5-HT$_3$ receptor. The colour code is the same for all panels. Scissors indicate the enzymatic treatments used during purification: purification tag removal using TEV protease, and partial removal of carbohydrates using PNGase F. **b**, Topology scheme and structure of one subunit of the 5-HT$_3$ receptor. **c**, Sequence and numbering of the mouse 5-HT$_{3A}$ receptor used in the present study. Secondary structures and important loops are indicated. Neurotransmitter site binding loops are highlighted. Important residues discussed in the study are boxed (pore-facing in red, sandwich motif in brown and neurotransmitter site in blue). Cyan highlights residues important for TMPPAA potency. Glycosylation sites are depicted in green. The mouse receptor used for this study is a variant compared to the consensus sequence as it contains an alanine insertion in the M2–M3 loop, which is highlighted by the pink box. Notably, this insertion is present in the consensus human receptor sequence. This panel is adapted from ref. [5]. **d**, A typical unmasked reconstruction, with different density levels overlaid depicting the protein itself (yellow), ligands (purple), linked glycans (green), the detergent-lipid belt (transparent purple) and the footprint of the disordered zone (transparent grey). **e**, Currents induced in *Xenopus* oocytes expressing the mouse 5-HT$_{3A}$ receptor by a 3-min application of 10 μM serotonin (green traces), co-application of 10 μM serotonin and 100 nM tropisetron (following a 5-min pre-application of tropisetron, red trace), co-application of 10 μM serotonin and 10 μM of TMPPAA (following a 5-min pre-application of TMPPAA, black trace). Current traces are representative of 3 independently repeated experiments.

RESEARCH LETTER

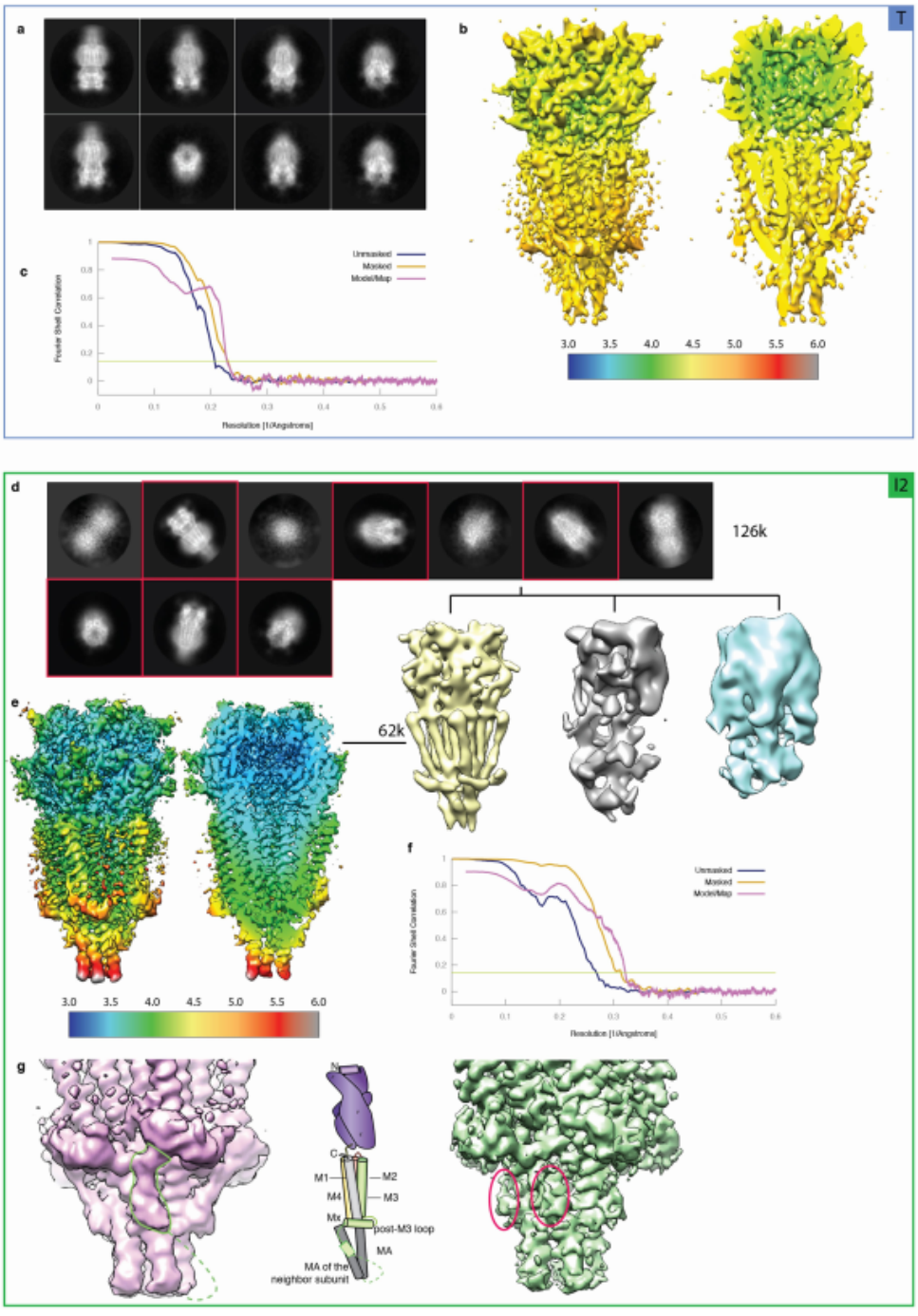

Extended Data Fig. 2 | See next page for caption.

Extended Data Fig. 2 | Electron microscopy and 3D reconstructions for the tropisetron dataset (T), and for the serotonin + TMPPAA dataset (I2). **a**, Tropisetron dataset (T). Selection of 2D class averages from the set of particles used for refinement of the tropisetron reconstruction. **b**, Three-dimensional reconstruction from the tropisetron dataset, filtered and coloured according to RELION local resolution. A global and a cut-through side view are shown. **c**, FSC curves for the density map before and after RELION post-processing, and between the model and the final map. **d**, Serotonin + TMPPAA dataset (I2). Selection of good 2D classes after one round of classification yields a set of 126,000 particles. One round of 3D classification with no symmetry imposed yields one class with pentameric symmetry, amounting to 62,000 particles. **e**, Unmasked unsharpened refined 3D reconstruction, filtered and coloured according to RELION local resolution. The colour range for resolution is similar to the equivalent representations for the other datasets in Extended Data Fig. 4c, allowing direct comparison. **f**, FSC curves for the density map before and after RELION post-processing, and between the model and the final map. **g**, Left, a non-sharpened map filtered at 3.9 Å resolution, obtained with a subset of 55,000 particles from the I2 dataset, selected after further 3D classification focused on the ICD. The hypothetical trajectory of the polypeptide chain after MX is bordered by a green line. No full connectivity can be visualized and the model was not built. The chain appears to descend abruptly after MX, and may interact with MA of the neighbouring subunit at the level of H411, where there is a clear density. Then it must link to the beginning of MA, but maps show no information how it may do so. The schematic representation highlights that this putative trajectory contacts MA on the neighbouring subunit close to residue H411. Right, the corresponding sharpened and masked reconstruction, showing that model building is not possible. The density of the disordered stretch closed to H411 is highlighted by the pink ellipses.

RESEARCH LETTER

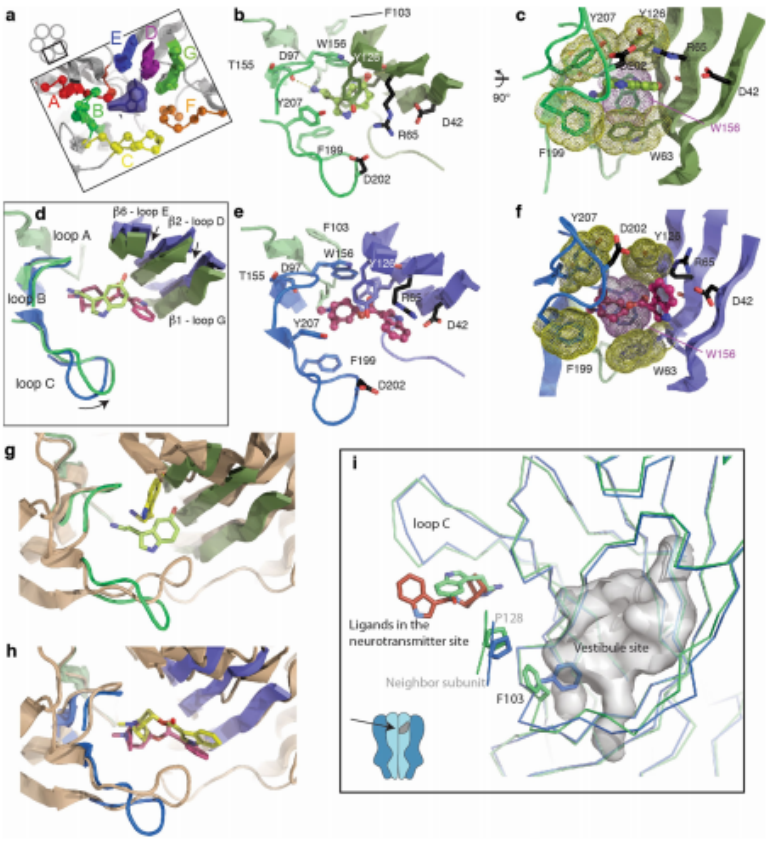

Extended Data Fig. 3 | Serotonin and tropisetron bound in the orthosteric site; the vestibule allosteric site. a, Organization of one of the five equivalent binding sites at the subunit interfaces in the ECD. Binding loops A–C are located on the principal subunit, and binding elements D–G are on the complementary subunit. The density around serotonin in the I2 reconstruction is shown as a transparent blue surface. **b**, **c**, Serotonin (ball-and-stick) in the orthosteric site in the I2 structure. Aromatic residues (dotted surfaces in **c**), hydrogen bonds with main chain atoms (dashed lines) and charged residues within salt-bridge distances (D202 on the principal side, R65 on the complementary side) are noted in two orthogonal views. Of note, mutants D202A[64] and R65A[65] exhibit impaired serotonin binding with increases of around 140-fold and 50-fold, respectively, in K_i (the equilibrium inhibitor constant) during competition assay for [^{3}H]-granisetron binding. **d**, Superimposition of tropisetron-bound T (blue) and serotonin-bound I2 (green) structures, highlighting loop C motion and quaternary reorganization with arrows (principal subunit superposition in this panel and in **g** and **h**; note complementary subunit β-strand shift). Serotonin (light green) and tropisetron (magenta) are represented as sticks. **e**, **f**, Tropisetron bound to the orthosteric site in the T structure. The bicyclic tropane moiety is sandwiched between W156 of loop B and Y207 of loop C, whereas the indole lies close to R65, W63 in loop D, D42 and I44 in loop G, and R169 in loop F. Functional exploration of the binding mode of tropisetron consistently showed that, among others, single mutations to cysteine of the aromatic residues W156, Y207 or W63 abolished binding[66]. To fit tropisetron, the side chain of R65 is pushed upward and in turn displaces the side chains of Y67 and W168, compared to the empty orthosteric site of the X-ray structure. Densities for these side chains are not well-resolved. The density for tropisetron is shown in Extended Data Fig. 5f. **g**, Superposition of the I2 structure with the crystal structure of a mutant acetylcholine binding protein (AChBP, wheat cartoon) in complex with serotonin[67] (yellow sticks) shows distinct binding modes. **h**, Superposition of the T structure with the crystal structure of AChBP (wheat cartoon) in complex with tropisetron (yellow sticks) shows a similar orientation of ligands but different interactions with the protein at loop C, D, E, F and G (not shown for clarity), consistent with the 3 orders of magnitude difference (0.7 versus 479 nM[68]) in K_d (dissociation constant). **i**, Overlay of the T and I2 structures (in blue and green, respectively) superimposed on a subunit ECD, showing the motion of F103 out of the vestibule site. The protein depicted as ribbon is viewed from inside the vestibule, and the intra-subunit cavity (in the I2 conformation) is represented as a grey surface. Acetate in GLIC, flurazepam in the bacterial homologue ELIC[69] or a drug fragment in α7-AChBP[70] bind to this cavity. A putative rationale for the strong effect of F103 mutants on serotonin EC_{50}[71], despite its absence of participation in the binding site, comes from the observation of its concerted motion with that of strands from the neighbouring subunit (around P128 and around P110; for clarity, the latter is not represented here). Therefore, the motion of F103 may participate in subunit–subunit quaternary reorganization, exemplifying the allosteric coupling between sites.

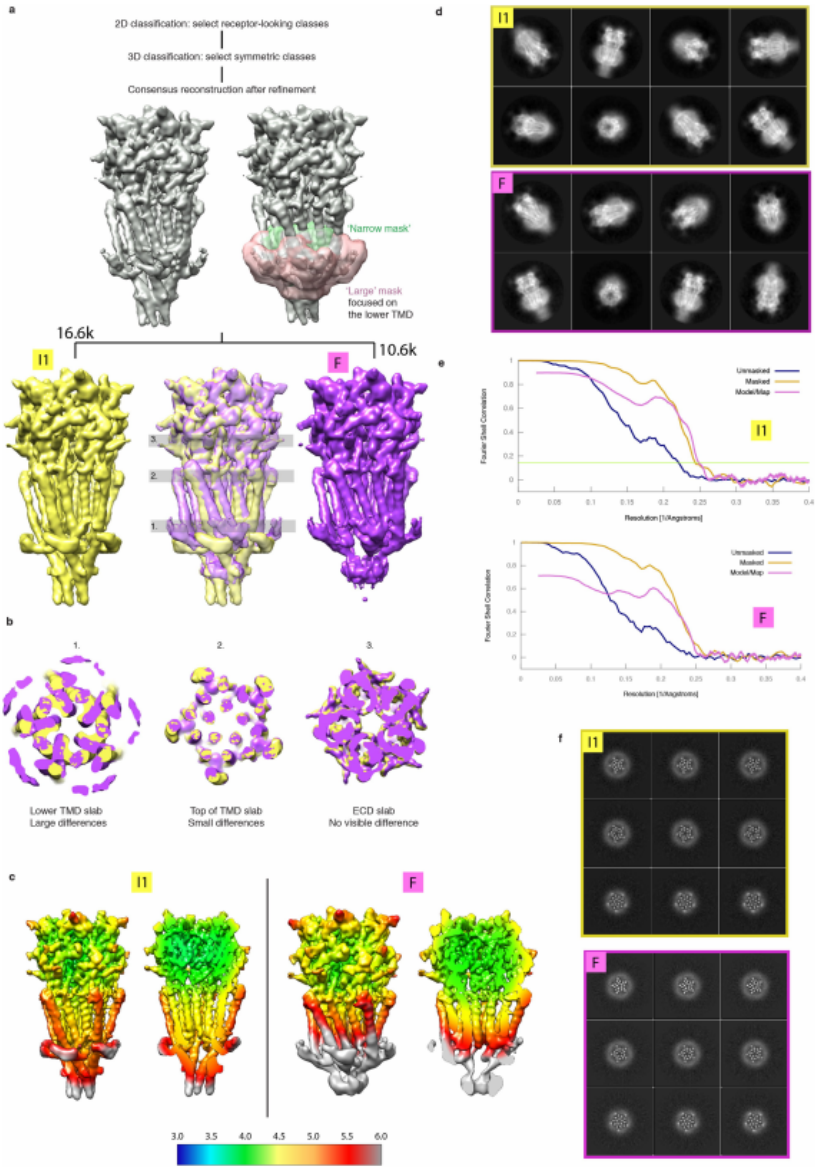

Extended Data Fig. 4 | See next page for caption.

RESEARCH LETTER

Extended Data Fig. 4 | Electron microscopy, classifications and 3D reconstructions for the serotonin dataset. a, Schematic of the data processing, with classical rounds of 2D and 3D classification yielding a consensus reconstruction seen parallel to the membrane plane (grey) where helices look like tubes of elliptic sections, indicating heterogeneity. Extensive classification trials, without alignment, with masks of various size covering the lower part of the TMD (shown in green and red) enable two conformations to be distinguished (yellow corresponding to the I1 structure, and purple corresponding to the F structure), representing the extreme positions of the helices in the consensus reconstruction. An overlay of the two reconstructions depicts the good superimposition of the ECD and the clear difference in the lower TMD. Grey rectangles indicate the positions of the slabs represented in **b**. All reconstructions shown are unmasked outputs of RELION 3D refinements. **b**, Slabs, viewed perpendicular to the membrane plane, from the intracellular side showing the overlay of the I1 and the F reconstructions. **c**, Reconstructions filtered and coloured according to RELION local resolution. A global and a cut-through side view are shown. **d**, Selection of 2D class averages from the set of particles used for refinement of the I1 and F reconstructions. **e**, FSC curves showing the unmasked and masked FSCs (before and after post-processing in RELION), and the model-to-map FSC. **f**, Selection of 'slice' views of the TMD of the final unmasked unsharpened reconstructions.

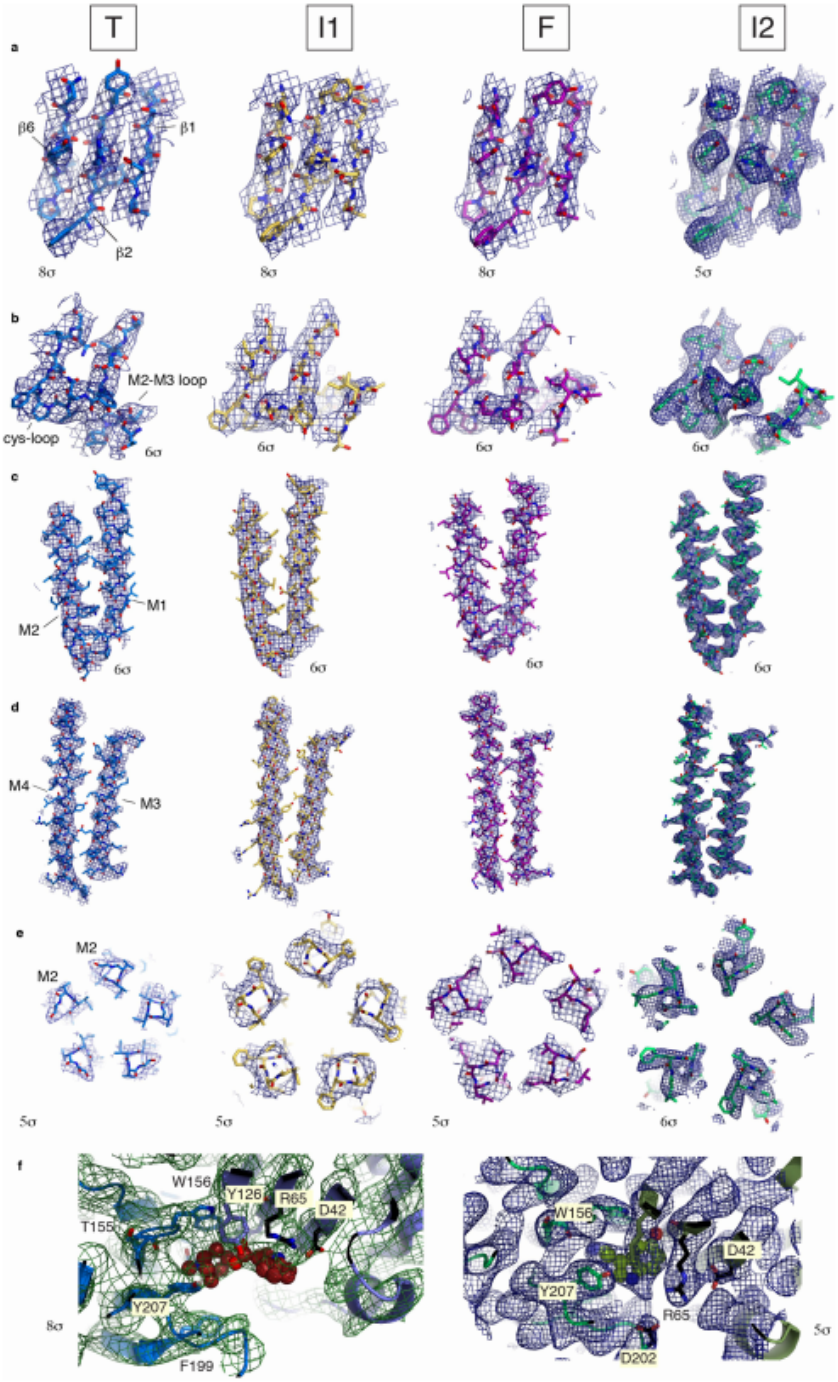

Extended Data Fig. 5 | Quality of the density maps in representative regions of the four 5-HT$_3$ receptor reconstructions. Densities in mesh representations overlaid with structures for the T (blue), I1 (yellow), F (purple) and I2 (green) reconstructions and structures, left to right, respectively, in each panel. Views **a**–**e** are approximately the same as those in extended data figure 4 of a previous publication of α1 GlyR[7]. **a**, Representative densities of the β-sheets in the ECD. **b**, Densities of the Cys loop and the M2–M3 loop. **c**, Densities of helices M1 and M2. **d**, Densities of M3 and M4. **e**, Densities of M2 at the level of L9′ (L260). **f**, Densities around the ligands tropisetron (in T) and serotonin (in I2). The 3.2 Å resolution of I2 permits unambiguous orientation of serotonin, and side chains of residues around the ligands are seen in densities. For tropisetron, given the limited 4.5 Å global resolution, the orientation of the ligand and the positions of surrounding side chain are less certain. The views are the same as in Extended Data Fig. 3b, e.

RESEARCH LETTER

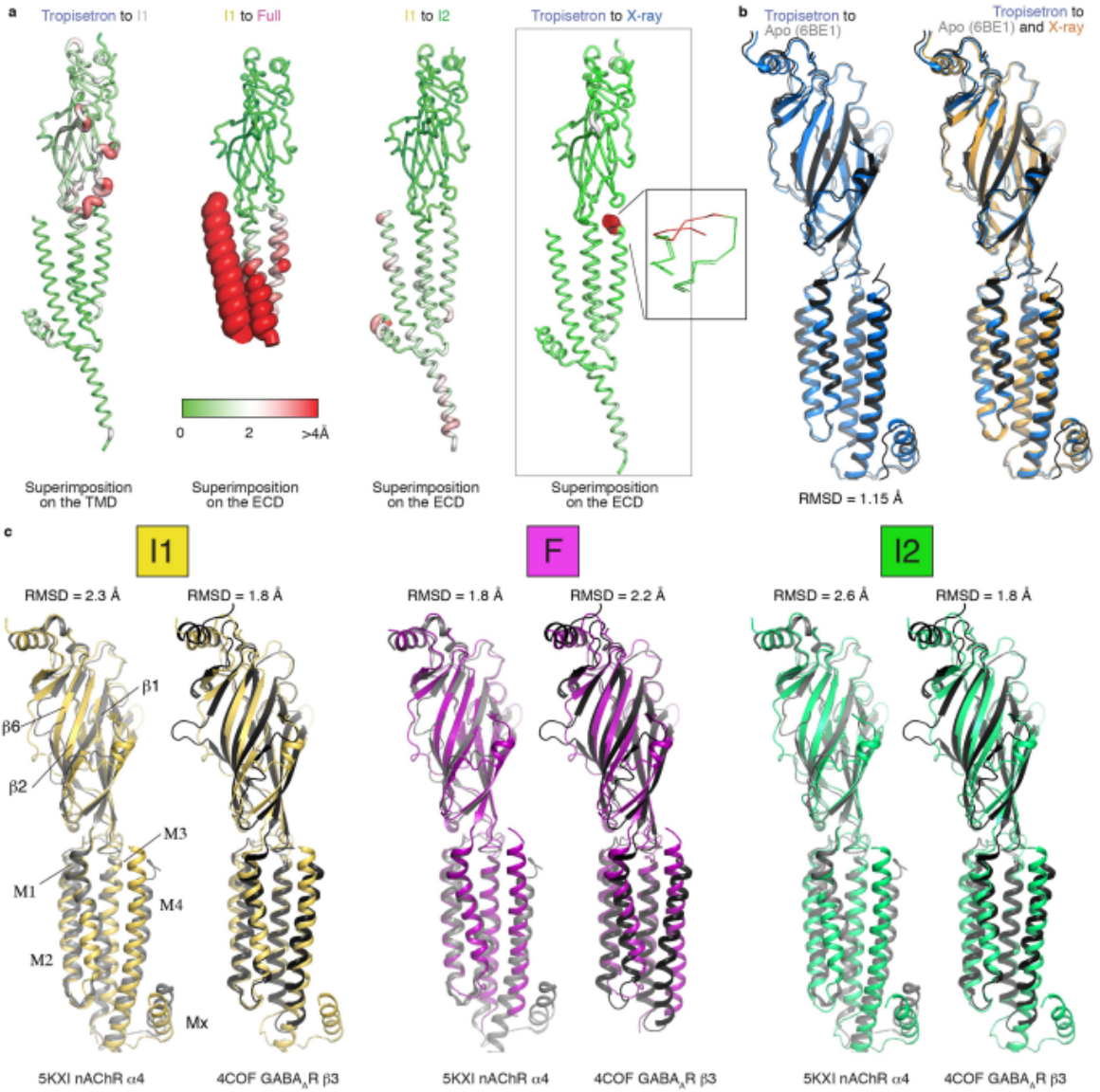

Extended Data Fig. 6 | Structural superpositions with the nAChR α4β2, the GABA$_A$ receptor β3 subunit and the apo 5-HT$_3$ receptor structures. **a**, Putty representations of pairwise deviations for the 5-HT$_3$ receptor conformations. The selection used for superimposition, and the two conformations used, are noted for each image. The colour code and tube thickness code are the same for all images. In the T versus X-ray image, the red zone corresponds to a loop that was not modelled in the X-ray structure. **b**, Superimposition of a 5-HT$_3$ receptor subunit in the inhibited T state (blue) and of a 5-HT$_3$ receptor subunit in the apo state (grey, PDB: 6BE1). Structures are globally similar with differences in the lipid-exposed helices M3, MX and M4, hypothetically a consequence of the different additives used—a lipid mixture in this study versus fluorinated fos-choline 8 for the apo structure. Superposition of the T structure (blue), the apo structure (grey) and the X-ray structure (orange). **c**, Superposition of a 5-HT$_3$ receptor subunit in the I1, I2 and F conformations with a nAChR α4 subunit (PDB: 5KXI, chain A) or a GABA$_A$ receptor β3 subunit (PDB: 4COF). C_α r.m.s.d. is noted. Comparison of superpositions with r.m.s.d. below 2 Å shows that in the case of F and nAChR α4 (middle, purple and grey), the domain-to-domain orientation is very similar and the extracellular halves of helices M1, M2, M3 superimpose very well, whereas clear deviations are present in their intracellular halves and at the level of M4 (r.m.s.d. without M4 drops to 1.6 Å). In the case of I1 and GABA$_A$ β3 (left, yellow and black), or I2 and GABA$_A$ β3 (right, green and black), differences are more distributed; deviations of the ECD indicate different domain-to-domain orientations, and in the TMD M1 and M3 superimpose quite well but M2 and M4 clearly differ.

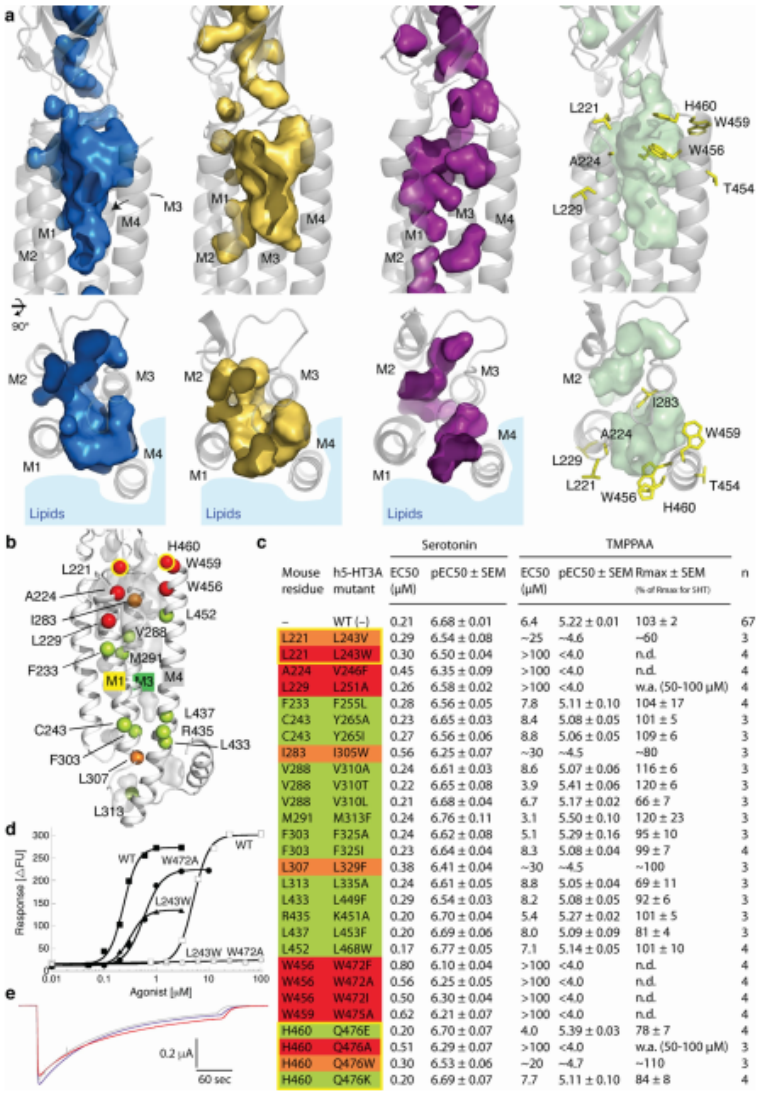

Mouse residue	h5-HT3A mutant	Serotonin EC50 (μM)	Serotonin pEC50 ± SEM	TMPPAA EC50 (μM)	TMPPAA pEC50 ± SEM	TMPPAA Rmax ± SEM (% of Rmax for 5HT)	n
–	WT (–)	0.21	6.68 ± 0.01	6.4	5.22 ± 0.01	103 ± 2	67
L221	L243V	0.29	6.54 ± 0.08	~25	~4.6	~60	3
L221	L243W	0.30	6.50 ± 0.04	>100	<4.0	n.d.	4
A224	V246F	0.45	6.35 ± 0.09	>100	<4.0	n.d.	4
L229	L251A	0.26	6.58 ± 0.02	>100	<4.0	w.a. (50-100 μM)	4
F233	F255L	0.28	6.56 ± 0.05	7.8	5.11 ± 0.10	104 ± 17	4
C243	Y265A	0.23	6.65 ± 0.03	8.4	5.08 ± 0.05	101 ± 5	3
C243	Y265I	0.27	6.56 ± 0.06	8.8	5.06 ± 0.05	109 ± 6	3
I283	I305W	0.56	6.25 ± 0.07	~30	~4.5	~80	3
V288	V310A	0.24	6.61 ± 0.03	8.6	5.07 ± 0.06	116 ± 6	3
V288	V310T	0.22	6.65 ± 0.08	3.9	5.41 ± 0.06	120 ± 6	3
V288	V310L	0.21	6.68 ± 0.04	6.7	5.17 ± 0.02	66 ± 7	3
M291	M313F	0.24	6.76 ± 0.11	3.1	5.50 ± 0.10	120 ± 23	3
F303	F325A	0.24	6.62 ± 0.08	5.1	5.29 ± 0.16	95 ± 10	3
F303	F325I	0.23	6.64 ± 0.04	8.3	5.08 ± 0.04	99 ± 7	4
L307	L329F	0.38	6.41 ± 0.04	~30	~4.5	~100	3
L313	L335A	0.24	6.61 ± 0.05	8.8	5.05 ± 0.04	69 ± 11	3
L433	L449F	0.29	6.54 ± 0.03	8.2	5.08 ± 0.05	92 ± 6	3
R435	K451A	0.20	6.70 ± 0.04	5.4	5.27 ± 0.02	101 ± 5	3
L437	L453F	0.20	6.69 ± 0.06	8.0	5.09 ± 0.09	81 ± 4	3
L452	L468W	0.17	6.77 ± 0.05	7.1	5.14 ± 0.05	101 ± 10	4
W456	W472F	0.80	6.10 ± 0.04	>100	<4.0	n.d.	4
W456	W472A	0.56	6.25 ± 0.05	>100	<4.0	n.d.	4
W456	W472I	0.50	6.30 ± 0.04	>100	<4.0	n.d.	4
W459	W475A	0.62	6.21 ± 0.07	>100	<4.0	n.d.	4
H460	Q476E	0.20	6.70 ± 0.07	4.0	5.39 ± 0.03	78 ± 7	4
H460	Q476A	0.51	6.29 ± 0.07	>100	<4.0	w.a. (50-100 μM)	3
H460	Q476W	0.30	6.53 ± 0.06	~20	~4.7	~110	3
H460	Q476K	0.20	6.69 ± 0.07	7.7	5.11 ± 0.10	84 ± 8	4

Extended Data Fig. 7 | TMPPAA binds to an allosteric site in the TMD. **a**, Cavities in surface mode for the T (blue), I1 (yellow), F (purple) and I2 (green) states. Note the re-arrangement of the cavities between states. The protein is depicted in cartoon, with sticks in the right panels for residues in which mutations impair the effect of TMPPAA. Noisy densities are found in the I2 reconstruction, in or close to the cavities, but they do not permit ligand modelling and could correspond to parts of a lipid or detergent molecule. **b**, Side view of the transmembrane domain of I2 with mutated positions depicted as green spheres (for residues for which mutations had negligible effect on TMPPAA potency), orange spheres (for residues for which mutations reduced TMPPAA potency substantially) or red spheres (for mutations that completely or almost completely eliminated TMPPAA activity at concentrations up to 100 μM). Yellow circles indicate residues for which different mutations produced different effects. **c**, Functional properties exhibited by serotonin and TMPPAA as agonists at 5-HT_{3A} receptors expressed in tsA201 cells in an FMP assay. The human 5-HT_{3A} receptor was used for these experiments, since TMPPAA evokes a more robust agonist response through this receptor than through mouse 5-HT_{3A} in this assay[17]. The colour code is similar to that in **b**. n.d., not determinable, w.a., weak activity. A complete table of data for all tested mutant receptors is shown in Supplementary Table 1. **d**, Concentration-response curves for serotonin (closed symbols) and TMPPAA (open symbols) tested as agonists at wild-type, W472A and L243W human 5-HT_{3A} receptors expressed in tsA201 cells, using the FMP assay. Data are from a single representative experiment determined in the same 96-well plate and are given as mean based on duplicate determinations. The experiment was repeated independently with similar results 3 times for the W472A and L243W receptors and 66 times for the wild-type receptor (*n* for wild-type and all mutant receptors are given in **c**). **e**, Loss of TMPPAA potency at the mouse W456A mutant receptor. Currents evoked by 10 μM serotonin (blue curve) or 10 μM serotonin plus 100 μM TMPPAA (red curve) are equivalent. The grey trace, obtained in an oocyte expressing wild-type receptors (response to 10 μM serotonin, normalized for the peak amplitude), shows that desensitization in wild-type and W456A mutant receptors is similar. Current traces are representative of 3 independently repeated experiments.

RESEARCH LETTER

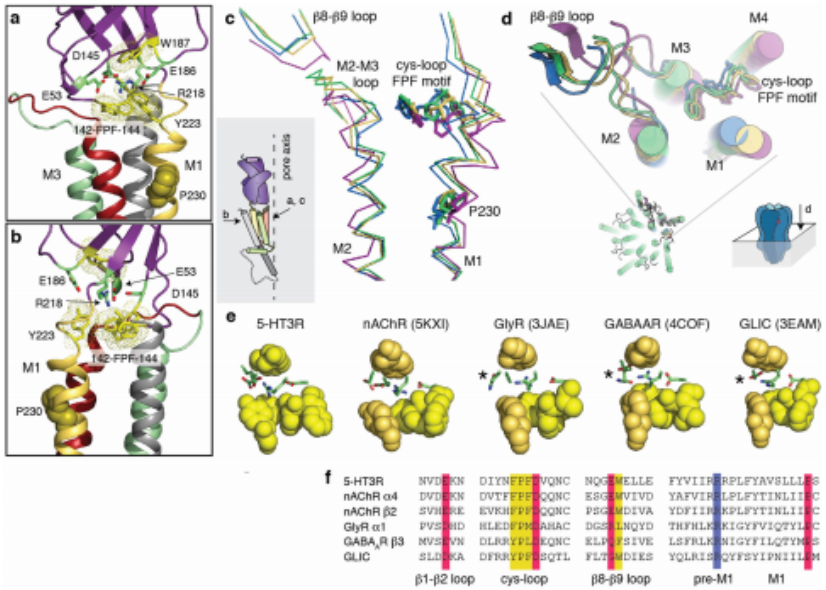

Extended Data Fig. 8 | Structural motif and reorganization at the ECD–TMD interface. a, **b**, Key interacting charged residues R218 (pre-M1, key in gating[72–74]), E53 (loop β1–β2), E186 (loop β8–β9, conserved only in cationic eukaryotic receptors) and D145 (Cys loop)—represented as purple sticks—are sandwiched between conserved essential aromatic residues (FPF motif of the Cys loop, W187 of β8–β9 and Y223 of M1), represented as yellow sticks and dots. Lower in the membrane, the strictly conserved P230—represented as spheres—enables M1 to kink. This structural organization is common to all pLGICs of known structure. Orientations of the views are indicated on the topology scheme. **c**, **d**, Side and top views depicting the concerted relative positions of the Cys-loop FPF 'wedge', represented as sticks, of transmembrane helices and of the β8–β9 loop. Compared to the inhibited structure, the wedge moves towards and pushes on M1 and also moves towards M4 in I1, I2 and F. F presents the biggest re-organization in this zone: M1, the M2–M3 loop and M3 follow the motion of the FPF motif, and M2 moves away from the pore axis (that is, to the back in the view in **c** and to the top in **d**). **e**, Conservation of the 'sandwich' structural motif in representative pLGIC structures. The aromatic top and bottom layers are represented as spheres (yellow, Cys loop; orange, β8–β9 loop and pre-M1 residue) whereas the central layer of charges is depicted as sticks. Note that in anionic receptors and GLIC, the charge of β8–β9 is absent (noted with a star). **f**, Sequence alignment of the motif residues in representative pLGIC structures.

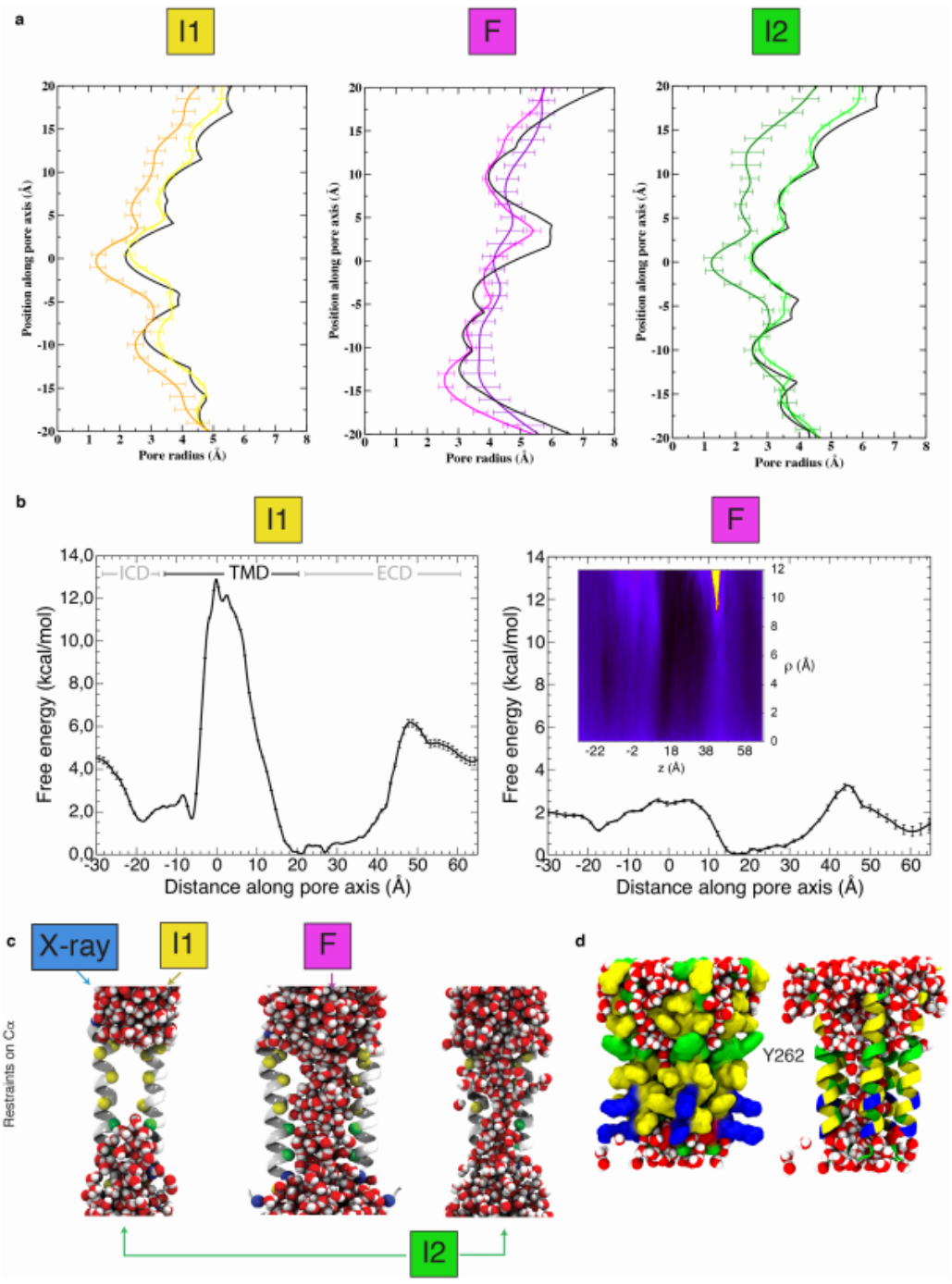

Extended Data Fig. 9 | See next page for caption.

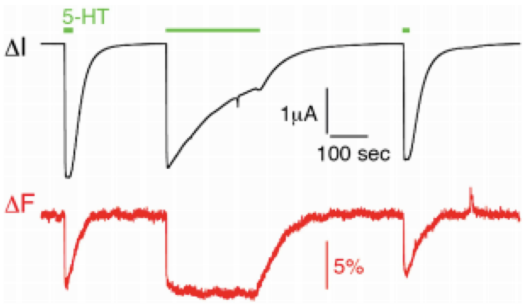

Extended Data Fig. 10 | Local motions in the pore probed by VCF. Representative serotonin-evoked simultaneous current and fluorescence recordings from oocytes expressing S19′C mutant receptors labelled with MTS-TAMRA. Similar traces were obtained in 3 independent experiments.

RESEARCH LETTER

Extended Data Table 1 | Statistics of 3D reconstructions and model refinement

	Tropisetron	Serotonin		Serotonin and TMPPAA
Data collection and processing				
Microscope	Krios@CCINA	Krios@CCINA		Krios@ESRF
Magnification	130,000	130,000		130,000
Voltage (kV)	300	300		300
Electron exposure (e-/Å^2)	~80	~60		~50
Defocus range (μm)	0.5-2.5	0.8-2.5		0.8-2.5
Pixel size (Å)	0.52	0.52		1.067
Symmetry imposed	C5	C5		C5
Number of images	~1500	~2000		~3000
Particles picked	160k	456k		250k
Symmetric-looking particles	133k	145k		62k
Particles refined	43,558	16,660	10,667	62,032
Refinement	T	I1	F	I2
Initial model used	4PIR	4PIR	4PIR	4PIR
Resolution (Å)	4.5	4.2	4.1	3.2
FSC threshold	0.143	0.143	0.143	0.143
Map sharpening B-factor (Å^2)	-247	-100	-100	-127
Model composition				
Non-hydrogen protein atoms	15,645	15,670	13,805	15,670
Protein residues	1,935	1,925	1,675	1,925
Ligands	585	415	415	415
B-factor (Å^2)				
protein	127	130	83	78
ligand	113	102	73	53
R.M.S devitions				
Bond lengths (Å)	0.008	0.009	0.009	0.006
Bond angles (°)	1.5	1.1	1.2	1.0
Validation				
Molprobity score	2.0	1.45	1.35	1.18
Clashscore	14.1	8.3	6.4	3.9
Poor rotamers (%)	0.3	0.2	0.3	0.3
Ramachandran plot				
Favored (%)	95.1	98.0	98.5	98.4
Allowed (%)	4.9	2.0	1.5	1.6
Disallowed (%)	0.0	0.0	0.0	0.0

5.3 Electron microscopy - discussion

pLGICs are prominent pharmacological targets, which are studied intensively, as illustrated by the number of structures solved during the last couple of years. However, these structures raise new questions and the detailed functional mechanism still remains shrouded by mystery. A comparison of the gating mechanism of 5-HT3RA with the mechanism elucidated for the other pLGICs (GluCl, GLIC and GlyR) is already discussed in our paper (e.g Extended Data Figures 6 and 8). Thus, in this section, I will focus on the direct comparison of the 5-HT3RA structures obtained by our group and independently by the group of Chakrapani, highlighting the main similarities and proposing reasons for potential differences.

In the following text I will keep the nomenclature of structures identical to that used in the original publications. To make it easier for the reader to become oriented in the nomenclature, I will also add the assigned functional state in brackets.

The mouse 5-HT3RA structures solved by cryo-EM were assigned to multiple physiological states, with various levels of confidence in the assignments. There is one apo resting state *(Basak et al., 2018a)*, one inhibited state (T) *(Polovinkin et al., 2018)*, one potentially pre-activated state plus one structurally closely related state (I1 and I2) *(Polovinkin et al., 2018)*, a open pore State 1 structure *(Basak et al., 2018a)* speculated to be non-conducting intermediate or a desensitized state, and two independent open pore structures (State 2 and F respectively) *(Basak et al., 2018b; Polovinkin et al., 2018).*

The assignment of the function is indeed more ambiguous for the receptors in the intermediate states where the ECD and ECD-TMD structures resemble the open state but where the pore remains closed. A structural comparison of the intermediate/desensitised structures shows that the I2 state resembles the independently obtained State 1 (agonist-bound non-conducting) to a greater degree, with a root-mean-square deviation (RMSD) of 1.1 Å, than the I1 state (pre-active state), with an RMSD of 1.6 Å (Fig. 32). Drawing conclusions from the RMSD comparison of the two independently obtained structures using different data processing and reaching only limited resolution is tricky. We can speculate that they might be very closely related, but regarding the RMSD differences among the structures of receptors from different families (e.g. comparison of the m-5HT3R to the GABAA subunit with the RMSD of 1.8 Å data shown in the enclosed publication (Extended data Fig 6., page 92) the option

that they represent distinct physiological states should not be neglected .

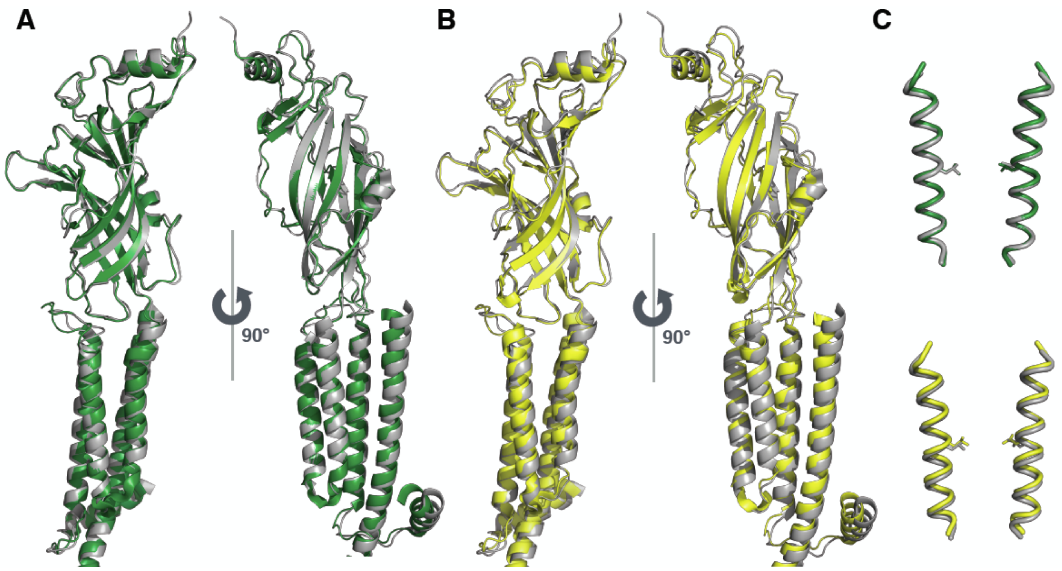

Figure 32 | A comparison of the I2 and I1 states to the potentially desensitised State 1 structure.

A. The I2 state (in green) aligned with State 1 (desensitised) (in grey). B. The I1 state (pre-active) (in yellow) aligned with the State 1 (desensitised) (in grey). The extracellular domains overlap closely. The top part of the M4 helix is tilted away in the State 1 structure together with the MX helix. The difference in RMSDs in A and B, when whole receptors were used for alignment, is 0.4 Å. Only the A subunits are shown. C. The M2 alignment shows the differences in the pore formation between the I2 state and State 1 (upper panel) and between the I1 and State 1 (lower panel). The M2 helices of the A and C subunits are shown with the L260 side chain indicated. The lower panel shows a slight offset of the bottom part of the M2 helix. All RMSDs were obtained using the "align" command in Pymol.

Unexpectedly, the biggest surprise comes from the comparison of the two open pore states: the F state and State 2. Unfortunately, the electron density maps are of comparable poor resolution at the level of the ICD in both cases, likely illustrating the ICD flexibility. In contrast to our competitors, we found the building of a structure into this part of the electron density map tricky and thus residues 311-425 were not built in the F state structure. For the purposes of overall structural alignment we use only the shortened version of the State 2 structure cut-down to correspond to the residues resolved in the F state. The overall structural alignment, with an RMSD of 1.9 Å, indicates significant differences. Interestingly, almost the same RMSD (2.0 Å) is observed between the open state F and the inhibited closed state T. Superimposition of the ECDs only shows that the conformation of the F state and of state 2 closely resemble each other with an RMSD of 1.1 Å.

Having a closer look at the binding site, the orientation of the serotonin is the same in both structures, making cation-π interaction with the W156 (Fig. 33). The inward motion of loop C in State 2 seems to be slightly less pronounced compared with the

F state when an alignment of the ECD is performed. Even though the relative distance (displacement) between the C loops of the apo and the open states solved by Basak et al. are similar to those of the inhibited state T and the open state F it seems that loop C stays further from loop G of the following subunit. It is difficult to judge the possible interaction between residues D202 and R65 in State 2 because of the poor density of the aspartate and the generally low resolution in this region.

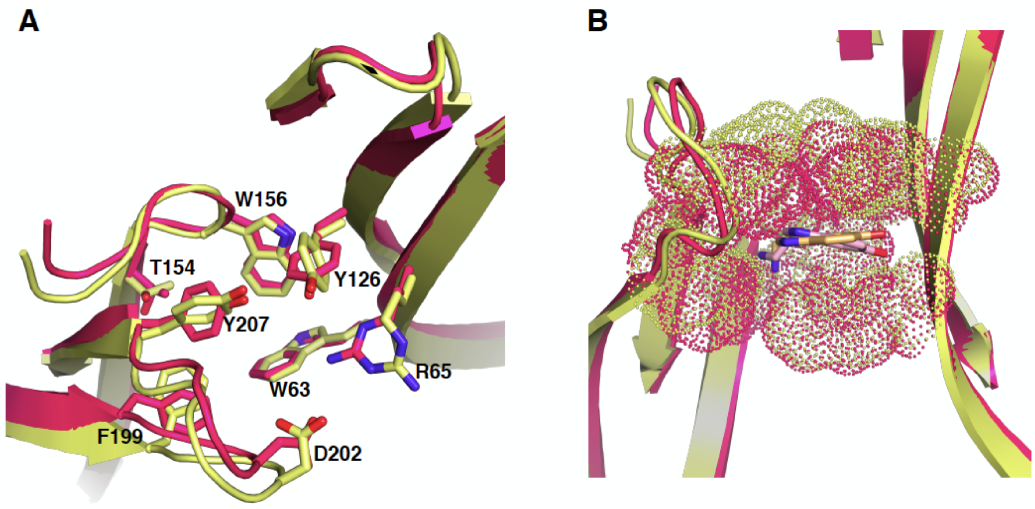

Figure 33 | Detailed view of the binding side of the two open structures, the F state (pink) and State 2 (yellow).

A) The side chains of the binding site residues. The serotonin is not shown for better comparison. **B)** The position of the serotonin position in the binding pocket. The dotted surface of the binding site side chain residues are shown. There is no large rearrangement of the ECD.

The poorly defined electron density map makes a more detailed comparison impossible also around the conserved Cys-loop region and in close proximity of R218 (important structural features triggering the gating mechanism). Thus it is not possible to draw any conclusions from the flipped side chain of W187 in the State 2 structure compared to all other structures of the receptor solved both by ourselves and by our competitors.

The most striking difference is a different arrangement of the M2 membrane helices, forming the pore, and of their immediate environment, which can be documented by an RMSD of 3.3 Å for the TMD region. Isolated TMD monomers superimpose with an RMSD of 2.1 Å, indicating that the subunit/subunit arrangement accounts for a large part of the differences between the F state and State 2. Accordingly, the interface areas in the TMD, measured using PISA, differ significantly, with ~1100 $Å^2$ buried for the F

state and only ~750 Å^2 for State 2. Comparing the pores, the one of State 2 is generally wider than the one of the F state. This difference is due to the positions of the M2 helices (Fig. 34). The helices start at about the same position on the intracellular site but then they diverge. This results in the ion pathways narrowing at different heights.

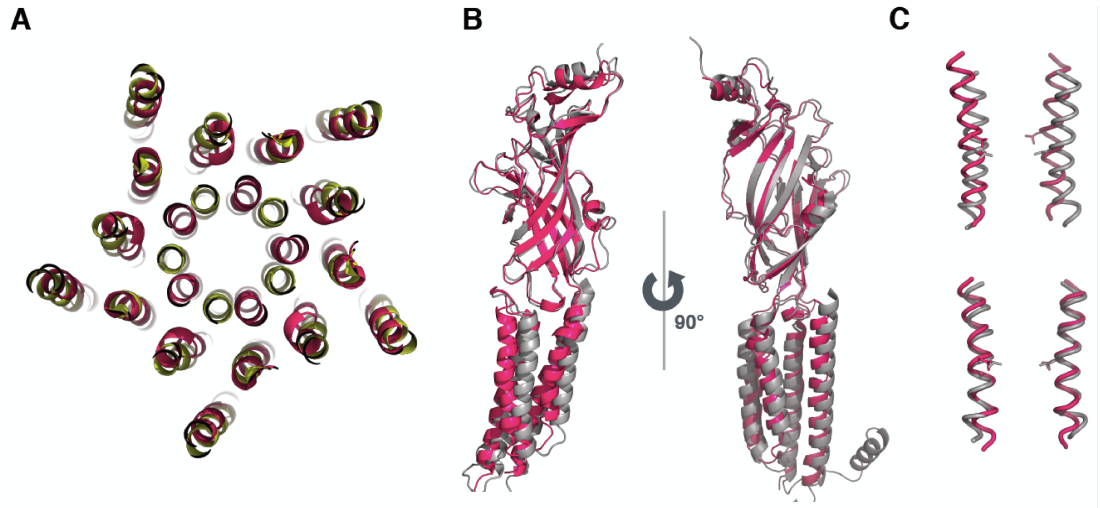

Figure 34 | The differences between the two open structures solved independently: the F state (pink) and State 2 (grey).

A) A cut parallel to the membrane at the extracellular side of the TMD. The translocation of the M2 helix at this position is significant. B. Even though the remaining helices generally overlap, the superimposition of the A subunits shows a more detailed difference in those two structures. The whole receptor was aligned for the comparisons shown in **(A)** and **(B)**, resulting in an RMSD value of 1.9 Å. **C)** A close-up of the pore forming M2 helices. The upper panel shows their relative positions after alignment of the entire structure and the lower panel shows an alignment of only the M2 helix. There is a widening of the bottom part of the M2 in the State 2 structure compared to the F state. The M2 helices of the A and C subunits are shown with the L260 side chain indicated.

Whereas the F state is largely open at the L9' (L260) activation gate, State 2, even though it is widely open, is actually narrowest at the level of this residue (Fig. 35). Compared to the F state, State 2 is significantly wider at the intracellular side of the transmembrane pore creating the vestibule. The pore radius of State 2 resembles that of the GlyR receptor solved by cryo-EM in the presence of glycine (open structure). This widely open pore conformation has brought some controversy *(Gonzalez-Gutierrez et al., 2017)* because the other open pore structures of pLGIC solved to date are narrower at the intracellular side. The structural studies of the mutated GLIC receptor together with molecular dynamics and electrophysiology studies further support the physiological relevance of the narrower open channel structures *(Gonzalez-Gutierrez et al., 2017)*.

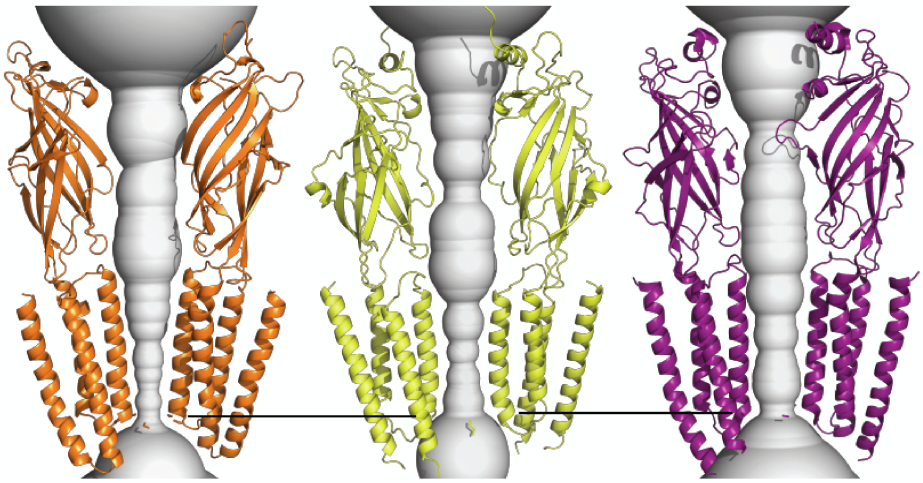

Figure 35 | The intracellular pore radius of GLIC (open), State 2 and the GlyRα1 (open) are compared.

It is clear that the state 2 pore (yellow) width at the lower TM2 position corresponds better to GlyRα1(purple) than to GLIC (orange). The side chains of the residues analogous to m5-HT3R's 249, 220 from GLIC and 265 from GlyRα1 are shown. For better clarity only the cartoon of the A and C subunits is shown, together with the eye guiding line indicating the level at which the comparison is being made.

Additionally, State 2 represents a less compact transmembrane helix bundle compared to the F state. The total volume of the State 2 TMD corresponds to 92.17 kÅ^3 (void 27.81 kÅ^3; VDW 64.36 kÅ^3) with a protein density of 0.698. The F state TMD total volume is 89.03 kÅ^3 (void 26.29 kÅ^3; VDW 62.73 kÅ^3) with a protein density of 0.705. All data were calculated by ProteinVolume v1.3 *(Chen and Makhatadze, 2015)*.

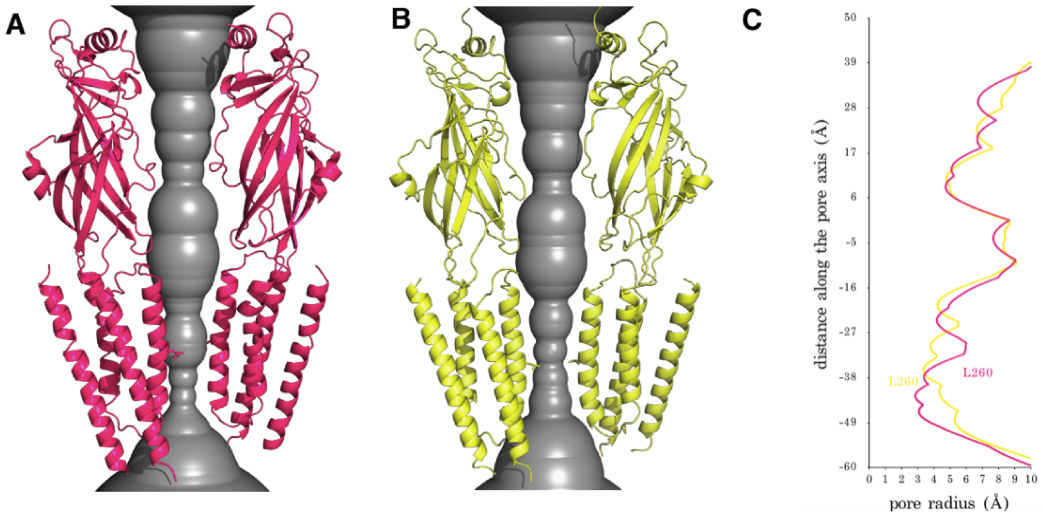

Figure 36 | The pore radius of the F state (pink) compared to that of State 2 (yellow).

A) and **(B)** show the difference in the ion channel constrictions. The pore radius size along the channel is shown by panel **(C)**. The F state structure is widely open at the gate residue L260, in contrast with State 2 where L260 is actually positioned in the narrowest part of the transmembrane pathway.

Another striking difference between the State 2 structure compared with the other conformational states of the receptor is the movement of the MX helix (Fig. 36A). This peripheral helix located on the intracellular side is in contact with the membrane in the structures of all the other states but is immersed into the membrane in the State 2 structure. This movement is in agreement with the F state that is seen on the alignment of the electron density maps of the F state and the I1 state (Fig. 36B).

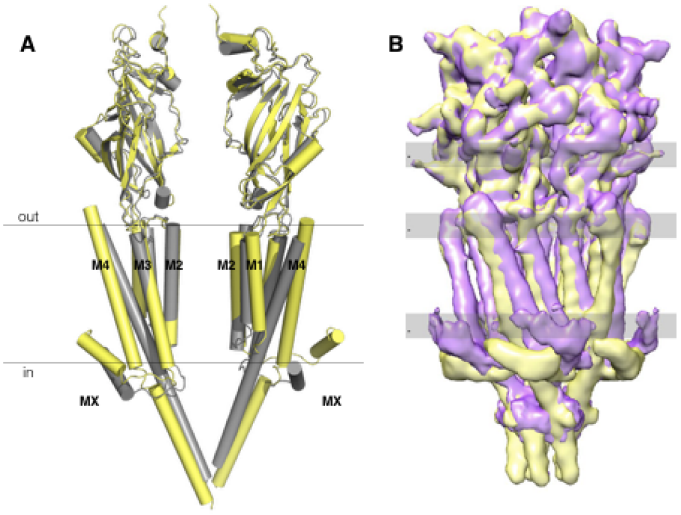

Figure 37 | A comparison of the MX helix position.

In **(A)**, the I1 state (pre-active) structure in grey compared to State 2 (open) in yellow and in **(B)** the pre-active state (yellow) compared to the F state in violet. The extensive movement of MX into the membrane in the State 2 and F (open) structures was observed. In **(A)** the I1 structure was used as a representative of all of the other structures, which have the MX oriented as a peripheral helix.

The C-terminal end of the MX helix moves ~10 Å along the normal to the membrane. Examples of helices that can enter the membrane exist *(Entova et al., 2018)*, and this motion might be part of the operation mechanism of the receptor. It might also be caused by the detergent environment.

The differences between those two open structures raise questions about their assignment to a physiological state. Multiple factors should be kept in mind. The F state and State 2 could potentially correspond to two different conformational states of the open receptor. The opening of the channel is a complex process complicated by the cooperativity of agonists acting at 5 orthosteric binding sites. The existence of multiple open forms has already been proposed for pLGIC *(Keramidas and Lynch, 2012)* and the concept was proven to be true for the single-channel study of the ELIC receptor *(Marabelli et al., 2015)* and for 5-HT3R *(Corradi et al., 2009)*. When comparing the two structures solved independently, it is thus extremely important to consider the

conditions under which they were obtained.

Therefore, the differences between the two open structures might be for physiological reasons (two distinct open states may actually exist) or due to the experimental conditions used. Firstly, the F state structure was solved in the presence of calcium cations which are known to affect the receptor conductivity. Secondly, pLGIC are known to be sensitive to their lipidic environment and here we are comparing a structure solved in the detergent $C_{12}E_9$ with added lipids (CHS, PA and PC) in the case of the F state and a structure solved in the presence of the same detergent and the addition of fluorinated Fos-choline 8 for State 2. Generally, the non-fluorinated fos-choline detergents are usually efficient in protein solubilisation but they should be used with caution because they might have destabilising and denaturing effect on certain proteins *(Chipot et al., 2018)*. In addition the fluorinated detergents might complicate interpretations since it was shown that they not only interact with ryanodine receptors but also it influences the conformational state of the protein (stabilisation of the closed conformation by the fluorinated octyl maltoside even after the application of strong agonist) through an unknown mechanism *(Willegems and Efremov, 2018)*.

Last but not least, there is an option that one of the structures is too far from biologically existing physiological state, and the result is an artefact.

For a long time, using detergents was the only way to extract membrane proteins from the lipid-bilayer (now, the recently developed SAM/DIBMA copolymers forming "native nanodiscs" may provide an alternative *(Dörr et al., 2014; Oluwole et al., 2017)*). Even though the detergent micelles do not reproduce the hallmarks of the lipid-bilayer environment, they remain the traditional choice for protein solubilisation, stabilisation in solution and thus also for structural studies.. Here I would like to sum up the effect of lipids on the pLGICs and how they might influence the structures (and not only those obtained by cryo-EM). The effect of amphipathic molecules, namely lipids and detergents, on the TMD of nAChRs was discussed in section 1.5.2.3 *(Fernández Nievas et al., 2008)* and the effect of different detergents and lipid additives on the purified 5-HT3R was shown in section 4.2.1.3 and at the end of this section. Interestingly, the 5-HT3R contains the sphingolipid binding motif at the extracellular part of the M1 helix *(Björkholm et al., 2014)*. But more generally, amphipathic molecules can have a great impact on the structure and/or function of pLGIC. They interact with the receptors in the allosteric binding site located in the upper and lower part of their TMD. Some lipids, included as additives or even being co-purified, were resolved in the pLGIC structures, suggesting tight interactions with the transmembrane helices *(Basak et al., 2017, 2018a;*

Bocquet et al., 2008; Chen et al., 2018) and suggesting possible regions of the receptor responsible for the lipid-driven modulation. In addition, mutagenesis of the interface between the outermost M4 helix and helices M1/M3 separated the pLGIC superfamily into two groups based on the compactness and tightness of this lipid-exposed region. GLIC, together with GlyR, the GABA receptor and GluCl, have extensive networks of interacting aromatic residues that form a densely packed M4-M1/M3 interface along the entire length of the M4 helix. In contrast, ELIC, the nAChR and the 5-HT3RA have fewer interactions in this region *(Therien and Baenziger, 2017)*. The Ala mutations of the aliphatic residues have have moderate or no effect as well as mutations of polar residues at the M4 - M1/M3 interface with exception of the M4 - M1 cation-π interactions which mutated abolish the ELIC functioning. Even though the aromatic side chain residues interactions are predominant in both, Ala mutations of single or both aromatic residues impair the GLIC whereas it has a little effect on the ELIC function. Those two groups, represented either by GLIC or by ELIC, should be potentially less or more prone to be influenced by changes in the surrounding lipid environment, respectively. Additionally the group to which the 5-HT3A belongs might undergo conformational changes more readily due to the weaker interactions.

The distorted GABA structures, imaged in detergent, show the gamma subunit collapsing into the pore and assymetric organisation of subunits the two different serotonin receptor structures in the open pore conformation could point to amphipathic molecules as a common denominator. But how does one choose detergents and lipids? Quite often the protein stability is measured prior to structural determination in order to get the most stable sample possible. This method, popularised by the Gouaux lab *(Gouaux et al., 2012),* has been used for GluCl, the GABA structure, and was probably used even for other structures. However, the generally intuitive idea that conditions, which result in the most thermostable proteins equal conditions where receptors are in a stable physiological state, may not be true in all cases. The artificial lateral pressure potentially created by the amphipathic molecules may result in non physiological tighter packing of the membrane domain helices, thus increasing the intramolecular interaction surface. Specifically, in the presence of an increased level of artificial interactions, the amount of energy needed to break them is higher. Finally, the higher thermal stability of proteins in amphipathic additives might reflect stronger non-native interactions and its maximisation might lead to false positive results. We tested the effect of different detergents on the protein stability and we can conclude that the detergents differ in their ability to stabilise the 5-HT3RA. Furthermore, in our hands the 5-HT3RA manifests the same thermal stability after the addition of lipid master mix (PA, CHS and brain PC; concentrations corresponding to our cryo-EM experiments) as it does in $C_{12}E_9$

(Fig. 38A) (measured by NanoTemper's Prometheus, experiment performed in agreement with the detergent screen described in 4.1.3). Interestingly, the addition of CHS during solubilisation by $C_{12}E_9$ affects the thermostability to a greater extent than addition of CHS just prior to measurement Fig. 38B) .

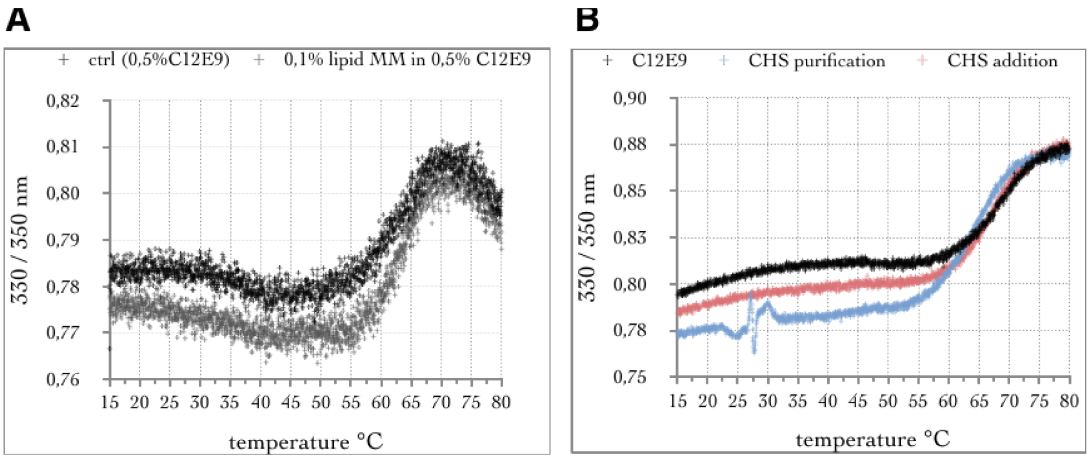

Figure 38 | The thermostability of the 5-HT3A receptor in the presence of lipid additives.

A) The addition of lipidic master mix added prior to the grid freezing (in grey). The black curve, serving as a control, shows the receptor stability after the addition of the detergent equivalent to that present in the lipidic master mix. The influence of the lipids is negligible when compared to the control sample. **B)** A comparison of the receptor thermostability when exposed to the CHS from the solubilisation step (blue) or just prior to measurement (red). The black curve is a control sample measured in the absence of CHS. The presence of the CHS during purification slightly decreases the thermal stability of the receptor.

6 Conclusion and perspectives

The objectives of my thesis were to obtain structure(s) of other conformational state(s) compared to the 2014 crystal structure and/or increase the resolution of the existing structure of 5-HT3RA (to enable for instance the unambiguous placement of ligands). We have shown that the 5-HT3RA can form crystals in a broad range of conditions (temperature, pH, salts, PEGs) using stabilising nanobodies and Cymal-6 as an additive. We failed to improve the poor diffraction of these crystals with many standard methods (cryoprotection, dehydration of crystals, on-plate measurements). Larger changes need to be implemented to improve the crystal quality. We have shown that changing the detergent might be critical step and we have selected the detergent UDM as a good candidate (section 4.2.1.2).

Starting with no prior experience of electron microscopy, we were able to gradually optimise the sample and the imaging conditions. In the end we obtained four structures of different conformations of the 5-HT3RA by cryo-EM, and could assign them to physiological states and propose a gating mechanism for this receptor compatible with SCAM and VCF experiments, which was also supported by molecular dynamics. The proposed gating mechanism shares some common features (quaternary reorganisation of the ECD, local movements in the ECD-TMD and the upper TMD region, general twist) and possesses some distinct ones compared to the mechanisms inferred for other pLGICs (in contrast to GLIC and GluCl the 5-HT3A and GlyR don't undergo the ECD un-blooming reorganisation, the pore radius of the 5-HT3RA lies in between those of the wider GlyR and the tighter GLIC pore, specific M4 sliding) *(Polovinkin et al., 2018)*. Finally, we compared our structures with the structures obtained by Chakrapani's group and noted a puzzling difference in the open pore structures (section 5.3).

The challenging dream to elucidate the gating mechanism of the pLGICs is becoming more and more realistic but together with a better understanding of the gating more questions are raised. Even though the pLGIC share some highly conserved sequences, specifically their overall architecture and general gating apparatus, their actual mechanism seems to differ. To generalise based on what we know about the gating mechanism of one family of receptors is no longer possible and conclusions generalised to the entire superfamily should be made with caution.

Structural studies like ours raise a lot of questions about their physiological relevance (as exemplified by a significant portion of the reviewer's comments to our paper) and they are sometimes still received with scepticism. The purified protein stability, biochemical environment and physical properties used in those studies are indeed not

ideal mimics of physiological conditions. Yet it is undeniable that structural studies performed after careful biochemistry deepen our understanding of how membrane proteins function.

A potentially controversial point is the assignment of a structure to a functional state. This assignment can be non-straightforward for all mechanistic proteins, which undergo certain conformational changes during their action. For pLGICs some classical criteria have emerged from the accumulated literature and are used to guide the functional labeling of structures: the position of the loop C, the overall channel radius, the width of the channel at the 9' position, the constriction at the selectivity filters, etc. Fortunately, the field is moving forward with more nuanced definitions of what is a closed/open pore, taking advantage of molecular dynamics. Not every structure to be solved can be easily categorised into the simple three-state model with a resting closed pore, an active open pore and a desensitised closed pore state. The structures of different pLGICs elucidated under a variety of conditions (presence/absence of ligand; use of stabilising nanobodies/Fabs; use of detergents, amphipol or nanodiscs) instead correspond to other classes (most of them known also from electrophysiology) like the apo-resting state, the ligand-bound resting state, or the ligand-bound pre-active state.

In summary, it is clear that the pLGIC field is missing time-resolved structural studies, ideally performed under native conditions. Amongst the methods currently available, this may be achievable using X-ray free electron laser (XFEL) measurements. For this purpose the development of photo-activatable ligands and easy growth of nanocrystal would need to be accomplished first. Both of those aspects, together with very limited availability of XFEL hardware, lower the probability of success using this method.

Considering the “available” methods and instruments, further structural studies by cryo-EM are of great interest. The potential influence of detergent, F-TAC and amphipol on 5-HT3RA could be deduced from structures solved in “membrane-like” conditions, using nanodiscs (or other type of discs). This will require the optimisation of the protocol for protein incorporation into the nanodiscs and possibly even require further rounds of grid preparation optimisation. The structures of the receptor in complex with an allosterically bound ligand (relatively straightforward), of the heteropentamer (requirement for sufficient amounts of the purified heteropentamer, which is more fragile compared to homopentamers) or of the protein with/without ICD in combination with/without the use of calcium in the presence of serotonin (in theory, only the structure without the ICD in the presence of calcium and serotonin is needed to compare with the structure already solved) might bring some insights into the protein pharmacology, functioning and assembly.

7 Bibliography

Abdel-Aziz, H., Windeck, T., Ploch, M., and Verspohl, E.J. (2006). Mode of action of gingerols and shogaols on 5-HT3 receptors: binding studies, cation uptake by the receptor channel and contraction of isolated guinea-pig ileum. Eur. J. Pharmacol. *530*, 136–143.

Alqazzaz, M., Thompson, A.J., Price, K.L., Breitinger, H.-G., and Lummis, S.C.R. (2011). Cys-loop receptor channel blockers also block GLIC. Biophys. J. *101*, 2912–2918.

Azami, J., Fozard, J.R., Round, A.A., and Wallis, D.I. (1985). The depolarizing action of 5-hydroxytryptamine on rabbit vagal primary afferent and sympathetic neurones and its selective blockade by MDL 72222. Naunyn. Schmiedebergs. Arch. Pharmacol. *328*, 423–429.

Baenziger, J.E., Morris, M.L., Darsaut, T.E., and Ryan, S.E. (2000). Effect of membrane lipid composition on the conformational equilibria of the nicotinic acetylcholine receptor. J. Biol. Chem. *275*, 777–784.

Baenziger, J.E., Domville, J.A., and Therien, J.P.D. (2017). The Role of Cholesterol in the Activation of Nicotinic Acetylcholine Receptors. Curr. Top. Membr. *80*, 95–137.

Barann, M., Linden, I., Witten, S., and Urban, B.W. (2008). Molecular actions of propofol on human 5-HT3A receptors: enhancement as well as inhibition by closely related phenol derivatives. Anesth. Analg. *106*, 846-57-table of contents.

Basak, S., Schmandt, N., Gicheru, Y., and Chakrapani, S. (2017). Crystal structure and dynamics of a lipid-induced potential desensitized-state of a pentameric ligand-gated channel. Elife *6*, 50151.

Basak, S., Gicheru, Y., Samanta, A., Molugu, S.K., Huang, W., Fuente, M. la de, Hughes, T., Taylor, D.J., Nieman, M.T., Moiseenkova-Bell, V., and Chakrapani, S. (2018a). Cryo-EM structure of 5-HT3A receptor in its resting conformation. Nat. Commun. *9*, 514.

Basak, S., Gicheru, Y., Rao, S., Sansom, M.S.P., and Chakrapani, S. (2018b). Cryo-EM reveals two distinct serotonin-bound conformations of full-length 5-HT3A receptor. Nature *563*, 270–274.

Basak, S., Gicheru, Y., Kapoor, A., Mayer, M.L., Filizola, M., and Chakrapani, S. (2019). Molecular mechanism of setron-mediated inhibition of full-length 5-HT3A receptor. Nat. Commun. *10*, 3225.

Beene, D.L., Brandt, G.S., Zhong, W., Zacharias, N.M., Lester, H.A., and

Dougherty, D.A. (2002). Cation−π Interactions in Ligand Recognition by Serotonergic (5-HT 3A) and Nicotinic Acetylcholine Receptors: The Anomalous Binding Properties of Nicotine †. Biochemistry *41*, 10262–10269.

Björkholm, P., Ernst, A.M., Hacke, M., Wieland, F., Brügger, B., and von Heijne, G. (2014). Identification of novel sphingolipid-binding motifs in mammalian membrane proteins. Biochim. Biophys. Acta *1838*, 2066–2070.

Blaus, B. (2014). Medical gallery of Blausen Medical 2014. WikiJournal Med. *1*.

Bloechl-Daum, B., Deuson, R.R., Mavros, P., Hansen, M., and Herrstedt, J. (2006). Delayed nausea and vomiting continue to reduce patients' quality of life after highly and moderately emetogenic chemotherapy despite antiemetic treatment. J. Clin. Oncol. *24*, 4472–4478.

Bocquet, N., Nury, H., Baaden, M., Le Poupon, C., Changeux, J.-P., Delarue, M., and Corringer, P.-J. (2008). X-ray structure of a pentameric ligand-gated ion channel in an apparently open conformation. Nature *457*, 111–114.

Bradley, P.B., Engel, G., Feniuk, W., Fozard, J.R., Humphrey, P.P., Middlemiss, D.N., Mylecharane, E.J., Richardson, B.P., and Saxena, P.R. (1986). Proposals for the classification and nomenclature of functional receptors for 5-hydroxytryptamine. Neuropharmacology *25*, 563–576.

Brejc, K., van Dijk, W.J., Klaassen, R. V, Schuurmans, M., van Der Oost, J., Smit, A.B., and Sixma, T.K. (2001). Crystal structure of an ACh-binding protein reveals the ligand-binding domain of nicotinic receptors. Nature *411*, 269–276.

Cao, E., Liao, M., Cheng, Y., and Julius, D. (2013). TRPV1 structures in distinct conformations reveal activation mechanisms. Nature *504*, 113–118.

Chang, C.C., and Lee, C.Y. (1963). Isolation of neurotoxins from the venom of bungarus multicinctus and their modes of neuromuscular blocking action. Arch. Int. Pharmacodyn. Ther. *144*, 241–257.

Chen, C.R., and Makhatadze, G.I. (2015). ProteinVolume: calculating molecular van der Waals and void volumes in proteins. BMC Bioinformatics *16*, 101.

Chen, Q., Wells, M.M., Arjunan, P., Tillman, T.S., Cohen, A.E., Xu, Y., and Tang, P. (2018). Structural basis of neurosteroid anesthetic action on GABAA receptors. Nat. Commun. *9*, 3972.

Cheng, Y. (2018). Membrane protein structural biology in the era of single particle cryo-EM. Curr. Opin. Struct. Biol. *52*, 58–63.

Chipot, C., Dehez, F., Schnell, J.R., Zitzmann, N., Pebay-Peyroula, E., Catoire, L.J., Miroux, B., Kunji, E.R.S., Veglia, G., Cross, T.A., and Schanda, P. (2018).

Perturbations of Native Membrane Protein Structure in Alkyl Phosphocholine Detergents: A Critical Assessment of NMR and Biophysical Studies. Chem. Rev. *118*, 3559–3607.

Coates, A., Abraham, S., Kaye, S.B., Sowerbutts, T., Frewin, C., Fox, R.M., and Tattersall, M.H. (1983). On the receiving end--patient perception of the side-effects of cancer chemotherapy. Eur. J. Cancer Clin. Oncol. *19*, 203–208.

Connolly, C.N., and Wafford, K.A. (2004). The Cys-loop superfamily of ligand-gated ion channels: the impact of receptor structure on function. Biochem. Soc. Trans. *32*, 529–534.

Corradi, J., Gumilar, F., and Bouzat, C. (2009). Single-Channel Kinetic Analysis for Activation and Desensitization of Homomeric 5-HT3A Receptors. Biophysj *97*, 1335–1345.

Cully, D.F., Vassilatis, D.K., Liu, K.K., Paress, P.S., Van der Ploeg, L.H., Schaeffer, J.M., and Arena, J.P. (1994). Cloning of an avermectin-sensitive glutamate-gated chloride channel from Caenorhabditis elegans. Nature *371*, 707–711.

daCosta, C.J.B., Medaglia, S.A., Lavigne, N., Wang, S., Carswell, C.L., and Baenziger, J.E. (2009). Anionic lipids allosterically modulate multiple nicotinic acetylcholine receptor conformational equilibria. J. Biol. Chem. *284*, 33841–33849.

daCosta, C.J.B., Dey, L., Therien, J.P.D., and Baenziger, J.E. (2013). A distinct mechanism for activating uncoupled nicotinic acetylcholine receptors. Nat. Chem. Biol. *9*, 701–707.

Dang, H., England, P.M., Farivar, S.S., Dougherty, D.A., and Lester, H.A. (2000). Probing the role of a conserved M1 proline residue in 5-hydroxytryptamine(3) receptor gating. Mol. Pharmacol. *57*, 1114–1122.

Davies, P.A., Pistis, M., Hanna, M.C., Peters, J.A., Lambert, J.J., Hales, T.G., and Kirkness, E.F. (1999). The 5-HT3B subunit is a major determinant of serotonin-receptor function. Nature *397*, 359–363.

Deiml, T., Haseneder, R., Zieglgänsberger, W., Rammes, G., Eisensamer, B., Rupprecht, R., and Hapfelmeier, G. (2004). Alpha-thujone reduces 5-HT3 receptor activity by an effect on the agonist-reduced desensitization. Neuropharmacology *46*, 192–201.

Derkach, V., Surprenant, A., and North, R.A. (1989). 5-HT3 receptors are membrane ion channels. Nature *339*, 706–709.

Dörr, J.M., Koorengevel, M.C., Schäfer, M., Prokofyev, A. V, Scheidelaar, S., van der Cruijsen, E.A.W., Dafforn, T.R., Baldus, M., and Killian, J.A. (2014). Detergent-free isolation, characterization, and functional reconstitution of a tetrameric K +channel:

The power of native nanodiscs. Proc. Natl. Acad. Sci. *111*, 18607–18612.

Doyle, D.A. (1998). The Structure of the Potassium Channel: Molecular Basis of K+ Conduction and Selectivity. Science (80-.). *280*, 69–77.

Du, J., Lü, W., Wu, S., Cheng, Y., and Gouaux, E. (2015). Glycine receptor mechanism elucidated by electron cryo-microscopy. Nature *526*, 224–229.

Duffy, N.H., Lester, H.A., and Dougherty, D.A. (2012). Ondansetron and Granisetron Binding Orientation in the 5-HT 3Receptor Determined by Unnatural Amino Acid Mutagenesis. ACS Chem. Biol. *7*, 1738–1745.

Efremov, R.G., Leitner, A., Aebersold, R., and Raunser, S. (2014). Architecture and conformational switch mechanism of the ryanodine receptor. 1–17.

Entova, S., Billod, J.-M., Swiecicki, J.-M., Martín-Santamaría, S., and Imperiali, B. (2018). Insights into the key determinants of membrane protein topology enable the identification of new monotopic folds. Elife *7*, 178.

Epstein, M., and Racker, E. (1978). Reconstitution of carbamylcholine-dependent sodium ion flux and desensitization of the acetylcholine receptor from Torpedo californica. J. Biol. Chem. *253*, 6660–6662.

Fakhfouri, G., Rahimian, R., Dyhrfjeld-Johnsen, J., Zirak, M.R., and Beaulieu, J.-M. (2019). 5-HT3 Receptor Antagonists in Neurologic and Neuropsychiatric Disorders: The Iceberg Still Lies beneath the Surface. Pharmacol. Rev. *71*, 383–412.

Fernández Nievas, G.A., Barrantes, F.J., and Antollini, S.S. (2008). Modulation of nicotinic acetylcholine receptor conformational state by free fatty acids and steroids. J. Biol. Chem. *283*, 21478–21486.

Fletcher, S., and Barnes, N.M. (1998). Desperately seeking subunits: are native 5-HT3 receptors really homomeric complexes? Trends Pharmacol. Sci. *19*, 212–215.

Gaddum, J.H., and Picarelli, Z.P. (1957). Two kinds of tryptamine receptor. Br. J. Pharmacol. Chemother. *12*, 323–328.

Gadsby, D.C. (2009). Ion channels versus ion pumps: the principal difference, in principle. Nat. Publ. Gr. *10*, 344–352.

Gao, Y., Cao, E., Julius, D., and Cheng, Y. (2016). TRPV1 structures in nanodiscs reveal mechanisms of ligand and lipid action. Nature 1–17.

Gill, C.H., Peters, J.A., and Lambert, J.J. (1995). An electrophysiological investigation of the properties of a murine recombinant 5-HT3 receptor stably expressed in HEK 293 cells. Br. J. Pharmacol. *114*, 1211–1221.

Gilmore, J., D'Amato, S., Griffith, N., and Schwartzberg, L. (2018). Recent advances

in antiemetics: new formulations of 5HT3-receptor antagonists. Cancer Manag. Res. *10*, 1827–1857.

Gonzalez-Gutierrez, G., Wang, Y., Cymes, G.D., Tajkhorshid, E., and Grosman, C. (2017). Chasing the open-state structure of pentameric ligand-gated ion channels. J. Gen. Physiol. *149*, 1119–1138.

Gouaux, M.H.R.H.E., Hibbs, R.E., and Gouaux, E. (2012). A Fluorescence-Detection Size-Exclusion Chromatography-Based Thermostability Assay for Membrane Protein Precrystallization Screening. Struct. Des. *20*, 1293–1299.

Grenningloh, G., Rienitz, A., Schmitt, B., Methfessel, C., Zensen, M., Beyreuther, K., Gundelfinger, E.D., and Betz, H. (1987). The strychnine-binding subunit of the glycine receptor shows homology with nicotinic acetylcholine receptors. Nature *328*, 215–220.

Gunthorpe, M.J., and Lummis, S.C. (2001). Conversion of the ion selectivity of the 5-HT(3a) receptor from cationic to anionic reveals a conserved feature of the ligand-gated ion channel superfamily. J. Biol. Chem. *276*, 10977–10983.

Gupta, D., Prabhakar, V., and Radhakrishnan, M. (2016). 5HT3 receptors: Target for new antidepressant drugs. Neurosci. Biobehav. Rev. *64*, 311–325.

Gurdon, J.B., Lane, C.D., Woodland, H.R., and Marbaix, G. (1971). Use of frog eggs and oocytes for the study of messenger RNA and its translation in living cells. Nature *233*, 177–182.

Halevi, S., McKay, J., Palfreyman, M., Yassin, L., Eshel, M., Jorgensen, E., and Treinin, M. (2002). The C. elegans ric-3 gene is required for maturation of nicotinic acetylcholine receptors. EMBO J. *21*, 1012–1020.

Halevi, S., Yassin, L., Eshel, M., Sala, F., Sala, S., Criado, M., and Treinin, M. (2003). Conservation within the RIC-3 gene family. Effectors of mammalian nicotinic acetylcholine receptor expression. J. Biol. Chem. *278*, 34411–34417.

Hargreaves, A.C., Lummis, S.C., and Taylor, C.W. (1994). Ca2+ permeability of cloned and native 5-hydroxytryptamine type 3 receptors. Mol. Pharmacol. *46*, 1120–1128.

Hassaine, G., Deluz, C., Li, X.-D., Graff, A., Vogel, H., and Nury, H. (2013). Large scale expression and purification of the mouse 5-HT3 receptor. BBA - Biomembr. *1828*, 1–9.

Hassaine, G., Deluz, C., Grasso, L., Wyss, R., Tol, M.B., Hovius, R., Graff, A., Stahlberg, H., Tomizaki, T., Desmyter, A., Moreau, C., Li, X.-D., Poitevin, F., Vogel, H., and Nury, H. (2014). X-ray structure of the mouse serotonin 5-HT3 receptor. Nature *512*, 276–281.

Hassaine, G., Deluz, C., Grasso, L., Wyss, R., Hovius, R., Stahlberg, H., Tomizaki, T., Desmyter, A., Moreau, C., Peclinovska, L., Minniberger, S., Mebarki, L., Li, X.-D., Vogel, H., and Nury, H. (2017). Expression, Biochemistry, and Stabilization with Camel Antibodies of Membrane Proteins: Case Study of the Mouse 5-HT3 Receptor. Methods Mol. Biol. *1635*, 139–168.

Henderson, R., and Unwin, P.N. (1975). Three-dimensional model of purple membrane obtained by electron microscopy. Nature *257*, 28–32.

Hewlett, W.A., Schmid, S.P., and Salomon, R.M. (2003). Pilot trial of ondansetron in the treatment of 8 patients with obsessive-compulsive disorder. J. Clin. Psychiatry *64*, 1025–1030.

Hibbs, R.E., and Gouaux, E. (2011). Principles of activation and permeation in an anion-selective Cys-loop receptor. Nature *474*, 54–60.

Higashi, H., and Nishi, S. (1982). 5-Hydroxytryptamine receptors of visceral primary afferent neurones on rabbit nodose ganglia. J. Physiol. *323*, 543–567.

Hilf, R.J.C., and Dutzler, R. (2008). X-ray structure of a prokaryotic pentameric ligand-gated ion channel. Nature *452*, 375–379.

Hodge, C.W., Kelley, S.P., Bratt, A.M., Iller, K., Schroeder, J.P., and Besheer, J. (2004). 5-HT(3A) receptor subunit is required for 5-HT3 antagonist-induced reductions in alcohol drinking. Neuropsychopharmacology *29*, 1807–1813.

Hodge, C.W., Bratt, A.M., and Kelley, S.P. (2008). Deletion of the 5-HT(3A)-receptor subunit blunts the induction of cocaine sensitization. Genes. Brain. Behav. *7*, 96–102.

Hodgkin, A.L., and Huxley, A.F. (1952). A quantitative description of membrane current and its application to conduction and excitation in nerve. J. Physiol. *117*, 500–544.

Holbrook, J.D., Gill, C.H., Zebda, N., Spencer, J.P., Leyland, R., Rance, K.H., Trinh, H., Balmer, G., Kelly, F.M., Yusaf, S.P., Courtenay, N., Luck, J., Rhodes, A., Modha, S., Moore, S.E., Sanger, G.J., and Gunthorpe, M.J. (2009). Characterisation of 5-HT 3C, 5-HT 3Dand 5-HT 3Ereceptor subunits: evolution, distribution and function. J. Neurochem. *108*, 384–396.

van Hooft, J.A., Kreikamp, A.P., and Vijverberg, H.P. (1997). Native serotonin 5-HT3 receptors expressed in Xenopus oocytes differ from homopentameric 5-HT3 receptors. J. Neurochem. *69*, 1318–1321.

Hope, A.G., Downie, D.L., Sutherland, L., Lambert, J.J., Peters, J.A., and Burchell, B. (1993). Cloning and fnctional expression of an apparent splice variant of the murine 5-HT3 receptor A subunit. Eur. J. Pharmacol. Mol. Pharmacol. *245*, 187–192.

Hu, X.Q., Zhang, L., Stewart, R.R., and Weight, F.F. (2003). Arginine 222 in the Pre-transmembrane Domain 1 of 5-HT3A Receptors Links Agonist Binding to Channel Gating. J. Biol. Chem. *278*, 46583–46589.

Huang, X., Chen, H., Michelsen, K., Schneider, S., and Shaffer, P.L. (2015). Crystal structure of human glycine receptor-α3 bound to antagonist strychnine. Nature *526*, 277–280.

Humphrey, P.P., Bountra, C., Clayton, N., and Kozlowski, K. (1999). Review article: the therapeutic potential of 5-HT3 receptor antagonists in the treatment of irritable bowel syndrome. Aliment. Pharmacol. Ther. *13 Suppl 2*, 31–38.

Hussy, N., Lukas, W., and Jones, K.A. (1994). Functional properties of a cloned 5-hydroxytryptamine ionotropic receptor subunit: comparison with native mouse receptors. J. Physiol. *481 (Pt 2*, 311–323.

Huxley, H.E., and Zubay, G. (1961). Preferential staining of nucleic acid-containing structures for electron microscopy. J. Biophys. Biochem. Cytol. *11*, 273–296.

Johnson, B.A., Roache, J.D., Ait-Daoud, N., Zanca, N.A., and Velazquez, M. (2002). Ondansetron reduces the craving of biologically predisposed alcoholics. Psychopharmacology (Berl). *160*, 408–413.

Katona, C.L., and Katona, C.P. (2014). New generation multi-modal antidepressants: focus on vortioxetine for major depressive disorder. Neuropsychiatr. Dis. Treat. *10*, 349–354.

Katz, B., and Thesleff, S. (1957). A study of the desensitization produced by acetylcholine at the motor end-plate. J. Physiol. *138*, 63–80.

Kelley, S.P., Dunlop, J.I., Kirkness, E.F., Lambert, J.J., and Peters, J.A. (2003). A cytoplasmic region determines single-channel conductance in 5-HT3 receptors. Nature *424*, 321–324.

Keramidas, A., and Lynch, J.W. (2012). An outline of desensitization in pentameric ligand-gated ion channel receptors. Cell. Mol. Life Sci. *70*, 1241–1253.

Kesters, D., Thompson, A.J., Brams, M., van Elk, R. eacute, Spurny, R., Geitmann, M., Villalgordo, J.M., Guskov, A., Danielson, U.H., Lummis, S.C.R., Smit, A.B., and Ulens, C. (2012). Structural basis of ligand recognition in 5-HT3 receptors. EMBO Rep. 1–8.

Kilpatrick, G.J., Jones, B.J., and Tyers, M.B. (1987). Identification and distribution of 5-HT3 receptors in rat brain using radioligand binding. Nature *330*, 746–748.

Koyama, Y., Kondo, M., and Shimada, S. (2017). Building a 5-HT3A Receptor Expression Map in the Mouse Brain. Sci. Rep. *7*, 42884.

Kozuska, J.L., Paulsen, I.M., Belfield, W.J., Martin, I.L., Cole, D.J., Holt, A., and Dunn, S.M.J. (2014). Impact of intracellular domain flexibility upon properties of activated human 5-HT 3receptors. Br. J. Pharmacol. *171*, 1617–1628.

Lansdell, S.J. (2005). RIC-3 Enhances Functional Expression of Multiple Nicotinic Acetylcholine Receptor Subtypes in Mammalian Cells. Mol. Pharmacol. *68*, 1431–1438.

Laverty, D., Thomas, P., Field, M., Andersen, O.J., Gold, M.G., Biggin, P.C., Gielen, M., and Smart, T.G. (2017). Crystal structures of a GABAA-receptor chimera reveal new endogenous neurosteroid-binding sites. Nat. Struct. Mol. Biol. *24*, 977–985.

Laverty, D., Desai, R., Uchański, T., Masiulis, S., Stec, W.J., Malinauskas, T., Zivanov, J., Pardon, E., Steyaert, J., Miller, K.W., and Aricescu, A.R. (2019). Cryo-EM structure of the human α1β3γ2 GABAA receptor in a lipid bilayer. Nature *565*, 516–520.

Lester, H. (2004). Cys-loop receptors: new twists and turns. Trends Neurosci. *27*, 329–336.

Lester, H. (2004). Cys-loop receptors: new twists and turns. Trends Neurosci. *27*, 329–336.

Liao, M., Cao, E., Julius, D., and Cheng, Y. (2013). Structure of the TRPV1 ion channel determined by electron cryo-microscopy. Nature *504*, 107–112.

Loo, T., Patchett, M.L., Norris, G.E., and Lott, J.S. (2002). Using Secretion to Solve a Solubility Problem: High-Yield Expression in Escherichia coli and Purification of the Bacterial Glycoamidase PNGase F. Protein Expr. Purif. *24*, 90–98.

Marabelli, A., Lape, R., and Sivilotti, L. (2015). Mechanism of activation of the prokaryotic channel ELIC by propylamine: a single-channel study. J. Gen. Physiol. *145*, 23–45.

Maricq, A. V, Peterson, A.S., Brake, A.J., Myers, R.M., and Julius, D. (1991). Primary structure and functional expression of the 5HT3 receptor, a serotonin-gated ion channel. Science (80-.). *254*, 432–437.

Masiulis, S., Desai, R., Uchański, T., Serna Martin, I., Laverty, D., Karia, D., Malinauskas, T., Zivanov, J., Pardon, E., Kotecha, A., Steyaert, J., Miller, K.W., and Aricescu, A.R. (2019). GABAA receptor signalling mechanisms revealed by structural pharmacology. Nature *565*, 454–459.

Mawe, G.M., Branchek, T.A., and Gershon, M.D. (1986). Peripheral neural serotonin receptors: identification and characterization with specific antagonists and agonists. Proc. Natl. Acad. Sci. *83*, 9799–9803.

McKinnon, N.K., Reeves, D.C., and Akabas, M.H. (2011). 5-HT3 receptor ion size selectivity is a property of the transmembrane channel, not the cytoplasmic vestibule portals. J. Gen. Physiol. *138*, 453–466.

McKinnon, N.K., Bali, M., and Akabas, M.H. (2012). Length and amino acid sequence of peptides substituted for the 5-HT3A receptor M3M4 loop may affect channel expression and desensitization. PLoS One *7*, e35563.

Meltzer, H.Y., Li, Z., Kaneda, Y., and Ichikawa, J. (2003). Serotonin receptors : their key role in drugs to treat schizophrenia. Prog. Neuro-Psychopharmacology Biol. Psychiatry *27*, 1159–1172.

Miller, P.S., and Aricescu, A.R. (2014). Crystal structure of a human GABAA receptor. Nature *512*, 270–275.

Miquel, M.-C., Emerit, M.B., Nosjean, A., Simon, A., Rumajogee, P., Brisorgueil, M.-J., Doucet, E., Hamon, M., and Vergé, D. (2002). Differential subcellular localization of the 5-HT3-As receptor subunit in the rat central nervous system. Eur. J. Neurosci. *15*, 449–457.

Miyazawa, A., Fujiyoshi, Y., and Unwin, N. (2003). Structure and gating mechanism of the acetylcholine receptor pore. Nature *423*, 949–955.

Monod, J., Wyman, J., and Changeux, J.-P. (1965). On the nature of allosteric transitions: A plausible model. J. Mol. Biol. *12*, 88–118.

Morales-Perez, C.L., Noviello, C.M., and Hibbs, R.E. (2016). X-ray structure of the human α4β2 nicotinic receptor. Nat. Publ. Gr. 1–17.

Nachmansohn, D. (1959). Role of acetylcholine in axonal conduction and neuromuscular transmission. Am. J. Phys. Med. *38*, 190–206.

Niesler, B., Weiss, B., Fischer, C., Nöthen, M.M., Propping, P., Bondy, B., Rietschel, M., Maier, W., Albus, M., Franzek, E., and Rappold, G.A. (2001). Serotonin receptor gene HTR3A variants in schizophrenic and bipolar affective patients. Pharmacogenetics *11*, 21–27.

Niesler, B., Frank, B., Kapeller, J., and Rappold, G.A. (2003). Cloning, physical mapping and expression analysis of the human 5-HT3 serotonin receptor-like genes HTR3C, HTR3D and HTR3E. Gene *310*, 101–111.

Niesler, B., Walstab, J., Combrink, S., Moller, D., Kapeller, J., Rietdorf, J., Bonisch, H., Gothert, M., Rappold, G., and Bruss, M. (2007). Characterization of the Novel Human Serotonin Receptor Subunits 5-HT3C,5-HT3D, and 5-HT3E. Mol. Pharmacol. *72*, 8–17.

Nishtala, S.N., Mnatsakanyan, N., Pandhare, A., Leung, C., and Jansen, M. (2016).

Direct interaction of the resistance to inhibitors of cholinesterase type 3 protein with the serotonin receptor type 3A intracellular domain. J. Neurochem. *137*, 528–538.

Nury, H., Van Renterghem, C., Weng, Y., Tran, A., Baaden, M., Dufresne, V., Changeux, J.-P., Sonner, J.M., Delarue, M., and Corringer, P.-J. (2011). X-ray structures of general anaesthetics bound to a pentameric ligand-gated ion channel. Nature *469*, 428–431.

Nys, M., Kesters, D., and Ulens, C. (2013). Structural insights into Cys-loop receptor function and ligand recognition. Biochem. Pharmacol. 1–53.

Oluwole, A.O., Danielczak, B., Meister, A., Babalola, J.O., Vargas, C., and Keller, S. (2017). Solubilization of Membrane Proteins into Functional Lipid-Bilayer Nanodiscs Using a Diisobutylene/Maleic Acid Copolymer. Angew. Chem. Int. Ed. Engl. *56*, 1919–1924.

Pardon, E., Laeremans, T., Triest, S., Rasmussen, S. oslash ren G.F., nig, A.W. ouml, Ruf, A., Muyldermans, S., Hol, W.G.J., Kobilka, B.K., and Steyaert, J. (2014). A general protocol for the generation of Nanobodies for structural biology. Nat. Protoc. *9*, 674–693.

Pfeiffer, F., Graham, D., and Betz, H. (1982). Purification by affinity chromatography of the glycine receptor of rat spinal cord. J. Biol. Chem. *257*, 9389–9393.

Phulera, S., Zhu, H., Yu, J., Claxton, D.P., Yoder, N., Yoshioka, C., and Gouaux, E. (2018). Cryo-EM structure of the benzodiazepine-sensitive α1β1γ2S tri-heteromeric GABAA receptor in complex with GABA. Elife *7*, 531.

Polovinkin, L., Hassaine, G., Perot, J., Neumann, E., Jensen, A.A., Lefebvre, S.N., Corringer, P.-J., Neyton, J., Chipot, C., Dehez, F., Schoehn, G., and Nury, H. (2018). Conformational transitions of the serotonin 5-HT3 receptor. Nature *563*, 275–279.

Price, K.L., Lillestol, R.K., Ulens, C., and Lummis, S.C.R. (2016). Palonosetron-5-HT3 Receptor Interactions As Shown by a Binding Protein Cocrystal Structure. ACS Chem. Neurosci. *7*, 1641–1646.

Pytliak, M., Vargová, V., Mechírová, V., and Felšöci, M. (2011). Serotonin receptors - from molecular biology to clinical applications. Physiol. Res. *60*, 15–25.

Rigaud, J.L., Mosser, G., Lacapere, J.J., Olofsson, A., Levy, D., and Ranck, J.L. (1997). Bio-Beads: an efficient strategy for two-dimensional crystallization of membrane proteins. J. Struct. Biol. *118*, 226–235.

Rondé, P., and Nichols, R.A. (1998). High calcium permeability of serotonin 5-HT3 receptors on presynaptic nerve terminals from rat striatum. J. Neurochem. *70*, 1094–1103.

Roux, B. (2017). Ion channels and ion selectivity. Essays Biochem. *61*, 201–209.

Ruepp, M.-D., Wei, H., Leuenberger, M., Lochner, M., and Thompson, A.J. (2017). The binding orientations of structurally-related ligands can differ; A cautionary note. Neuropharmacology *119*, 48–61.

Sanger, G.J., and Andrews, P.L.R. (2018). A History of Drug Discovery for Treatment of Nausea and Vomiting and the Implications for Future Research. Front. Pharmacol. *9*, 913.

Sauguet, L., Shahsavar, A., and Delarue, M. (2015). Crystallographic studies of pharmacological sites in pentameric ligand-gated ion channels. BBA - Gen. Subj. *1850*, 511–523.

Scheres, S.H.W. (2012). RELION: implementation of a Bayesian approach to cryo-EM structure determination. J. Struct. Biol. *180*, 519–530.

Schofield, P.R., Darlison, M.G., Fujita, N., Burt, D.R., Stephenson, F.A., Rodriguez, H., Rhee, L.M., Ramachandran, J., Reale, V., and Glencorse, T.A. (1987). Sequence and functional expression of the GABA A receptor shows a ligand-gated receptor super-family. Nature *328*, 221–227.

Seddon, A.M., Curnow, P., and Booth, P.J. (2004). Membrane proteins, lipids and detergents: not just a soap opera. Biochim. Biophys. Acta *1666*, 105–117.

Sobel, A., Weber, M., and Changeux, J.P. (1977). Large-scale purification of the acetylcholine-receptor protein in its membrane-bound and detergent-extracted forms from Torpedo marmorata electric organ. Eur. J. Biochem. *80*, 215–224.

Spier, A.D., and Lummis, S.C. (2000). The role of tryptophan residues in the 5-Hydroxytryptamine(3) receptor ligand binding domain. J. Biol. Chem. *275*, 5620–5625.

Stephenson, F.A., Watkins, A.E., and Olsen, R.W. (1982). Physicochemical characterization of detergent-solubilized gamma-aminobutyric acid and benzodiazepine receptor proteins from bovine brain. Eur. J. Biochem. *123*, 291–298.

Stevens, R., Rüsch, D., Solt, K., Raines, D.E., and Davies, P.A. (2005). Modulation of human 5-hydroxytryptamine type 3AB receptors by volatile anesthetics and n-alcohols. J. Pharmacol. Exp. Ther. *314*, 338–345.

Tasneem, A., Iyer, L.M., Jakobsson, E., and Aravind, L. (2005). Identification of the prokaryotic ligand-gated ion channels and their implications for the mechanisms and origins of animal Cys-loop ion channels. Genome Biol. *6*, R4.

Tecott, L.H., Maricq, A. V, and Julius, D. (1993). Nervous system distribution of the serotonin 5-HT3 receptor mRNA. Proc. Natl. Acad. Sci. *90*, 1430–1434.

Therien, J.P.D., and Baenziger, J.E. (2017). Pentameric ligand-gated ion channels

exhibit distinct transmembrane domain archetypes for folding/expression and function. Sci. Rep. *7*, 450.

Thompson, A.J., and Lummis, S.C.R. (2003). A single ring of charged amino acids at one end of the pore can control ion selectivity in the 5-HT 3receptor. Br. J. Pharmacol. *140*, 359–365.

Thompson, A.J., and Lummis, S.C.R. (2009). Calcium modulation of 5-HT3 receptor binding and function. Neuropharmacology *56*, 285–291.

Thompson, A.J., Price, K.L., Reeves, D.C., Chan, S.L., Chau, P.-L., and Lummis, S.C.R. (2005). Locating an antagonist in the 5-HT3 receptor binding site using modeling and radioligand binding. J. Biol. Chem. *280*, 20476–20482.

Thompson, A.J., Lester, H.A., and Lummis, S.C.R. (2010). The structural basis of function in Cys-loop receptors. Q. Rev. Biophys. *43*, 449–499.

Tribet, C., Audebert, R., and Popot, J.L. (1996). Amphipols: polymers that keep membrane proteins soluble in aqueous solutions. Proc. Natl. Acad. Sci. *93*, 15047–15050.

Turner, T.J., Mokler, D.J., and Luebke, J.I. (2004). Calcium influx through presynaptic 5-HT3 receptors facilitates GABA release in the hippocampus: in vitro slice and synaptosome studies. Neuroscience *129*, 703–718.

Tyers, M.B., and Freeman, A.J. (1992). Mechanism of the anti-emetic activity of 5-HT3 receptor antagonists. Oncology *49*, 263–268.

Unwin, N. (2005). Refined structure of the nicotinic acetylcholine receptor at 4A resolution. J. Mol. Biol. *346*, 967–989.

Urban, B.W., Bleckwenn, M., and Barann, M. (2006). Interactions of anesthetics with their targets: non-specific, specific or both? Pharmacol. Ther. *111*, 729–770.

Walsh, R.M., Roh, S.-H., Gharpure, A., Morales-Perez, C.L., Teng, J., and Hibbs, R.E. (2018). Structural principles of distinct assemblies of the human α4β2 nicotinic receptor. Nature *557*, 261–265.

Walstab, J., Hammer, C., Lasitschka, F., Moller, D., Connolly, C.N., Rappold, G., Bruss, M., Bonisch, H., and Niesler, B. (2010). RIC-3 Exclusively Enhances the Surface Expression of Human Homomeric 5-Hydroxytryptamine Type 3A (5-HT3A) Receptors Despite Direct Interactions with 5-HT3A, -C, -D, and -E Subunits. J. Biol. Chem. *285*, 26956–26965.

Willegems, K., and Efremov, R.G. (2018). Influence of Lipid Mimetics on Gating of Ryanodine Receptor. Structure *26*, 1303-1313.e4.

Yakel, J.L., Lagrutta, A., Adelman, J.P., and North, R.A. (1993). Single amino acid

substitution affects desensitization of the 5-hydroxytryptamine type 3 receptor expressed in Xenopus oocytes. Proc. Natl. Acad. Sci. *90*, 5030–5033.

Yan, D., and White, M.M. (2005). Spatial orientation of the antagonist granisetron in the ligand-binding site of the 5-HT3 receptor. Mol. Pharmacol. *68*, 365–371.

Yang, J. (1990). Ion permeation through 5-hydroxytryptamine-gated channels in neuroblastoma N18 cells. J. Gen. Physiol. *96*, 1177–1198.

Zhu, S., Noviello, C.M., Teng, J., Walsh, R.M., Kim, J.J., and Hibbs, R.E. (2018). Structure of a human synaptic GABAA receptor. Nature *559*, 67–72.

Zoonens, M., and Popot, J.-L. (2014). Amphipols for Each Season. *247*, 759–796.

8 Supplementary data

Table 1 | The summary of the pLGIC structures solved by different methods.

This table was generated using data and online software provided by rcsb.org (the PDB; Protein Data Bank). Data generated on 12 August, 2019.

PDB ID	Structure Title	Method	Resolution	DOI	Year
6HUG	CryoEM structure of human full-length alpha1beta3gamma2L GABA(A)R in complex with picrotoxin and megabody Mb38.	Cryo-EM	3.10	10.1038/s41586-018-0832-5	2019
6HUJ	CryoEM structure of human full-length heteromeric alpha1beta3gamma2L GABA(A)R in complex with picrotoxin, GABA and megabody Mb38.	Cryo-EM	3.04	10.1038/s41586-018-0832-5	2019
6HUK	CryoEM structure of human full-length alpha1beta3gamma2L GABA(A)R in complex with bicuculline and megabody Mb38.	Cryo-EM	3.69	10.1038/s41586-018-0832-5	2019
6HUO	CryoEM structure of human full-length heteromeric alpha1beta3gamma2L GABA(A)R in complex with alprazolam (Xanax), GABA and megabody Mb38.	Cryo-EM	3.26	10.1038/s41586-018-0832-5	2019
6HUP	CryoEM structure of human full-length alpha1beta3gamma2L GABA(A)R in complex with diazepam (Valium), GABA and megabody Mb38.	Cryo-EM	3.58	10.1038/s41586-018-0832-5	2019
6I53	Cryo-EM structure of the human synaptic alpha1-beta3-gamma2 GABAA receptor in complex with Megabody38 in a lipid nanodisc	Cryo-EM	3.20	10.1038/s41586-018-0833-4	2019
6NP0	Cryo-EM structure of 5HT3A receptor in presence of granisetron	Cryo-EM	2.92	10.1038/s41467-019-11142-8	2019
5MUO	X-ray structure of the 2-22' locally-closed mutant of GLIC in complex with propofol	X-Ray	3.19	10.1016/j.celrep.2018.03.108	2018
5MUR	X-ray structure of the F14'A mutant of GLIC in complex with propofol	X-Ray	3.10	10.1016/j.celrep.2018.03.108	2018
5MVN	X-ray structure of the M205W mutant of GLIC in complex with propofol	X-Ray	3.49	10.1016/j.celrep.2018.03.108	2018
5MZQ	X-ray structure of the M205W mutant of GLIC in complex with bromoform	X-Ray	2.80	10.1016/j.celrep.2018.03.108	2018
5NKJ	X-ray structure of the N239C mutant of GLIC	X-Ray	3.74	10.1016/j.celrep.2018.03.108	2018
6A96	Cryo-EM structure of the human alpha5beta3 GABAA receptor in complex with GABA and Nb25	Cryo-EM	3.51	10.1038/s41422-018-0077-8	2018
6BE1	Cryo-EM structure of serotonin receptor	Cryo-EM	4.31	10.1038/s41467-018-02997-4	2018
6CNJ	Structure of the 2alpha3beta stiochiometry of the human Alpha4Beta2 nicotinic receptor	Cryo-EM	3.70	10.1038/s41586-018-0081-7	2018
6CNK	Structure of the 3alpha2beta stiochiometry of the human Alpha4Beta2 nicotinic receptor	Cryo-EM	3.90	10.1038/s41586-018-0081-7	2018

PDB ID	Structure Title	Method	Resolution	DOI	Year
6D6T	Human GABA-A receptor alpha1-beta2-gamma2 subtype in complex with GABA and flumazenil, conformation B	Cryo-EM	3.86	10.1038/s41586-018-0255-3	2018
6D6U	Human GABA-A receptor alpha1-beta2-gamma2 subtype in complex with GABA and flumazenil, conformation A	Cryo-EM	3.92	10.1038/s41586-018-0255-3	2018
6DG7	Full-length 5-HT3A receptor in a serotonin-bound conformation-State 1	Cryo-EM	3.32	10.1038/s41586-018-0660-7	2018
6DG8	Full-length 5-HT3A receptor in a serotonin-bound conformation-State 2	Cryo-EM	3.89	10.1038/s41586-018-0660-7	2018
6DW0	Cryo-EM structure of the benzodiazepine-sensitive alpha1beta1gamma2S tri-heteromeric GABAA receptor in complex with GABA (Whole map)	Cryo-EM	3.80	10.7554/eLife.39383	2018
6DW1	Cryo-EM structure of the benzodiazepine-sensitive alpha1beta1gamma2S tri-heteromeric GABAA receptor in complex with GABA (ECD map)	Cryo-EM	3.10	10.7554/eLife.39383	2018
6EMX	X-ray structure of the N15'C mutant of GLIC in complex with bromoform	X-Ray	3.20	10.1016/j.celrep.2018.03.108	2018
6F7A	Gloeobacter Ligand-gated Ion Channel (GLIC) closed state crystallized in an ultra-swollen lipidic mesophase	X-Ray	6.00	10.1038/s41467-018-02996-5	2018
6FL9	The active form of a pentameric ion channel (sTeLIC) gated by alkaline pH - Wild type 2.3 Angstrom resolution	X-Ray	2.30	10.1073/pnas.1717700115	2018
6FLI	The active form of a pentameric ion channel (sTeLIC) gated by alkaline pH - Co-crystallization with 4-bromo cinnamic acid	X-Ray	3.00	10.1073/pnas.1717700115	2018
6FVQ	The active form of a pentameric ion channel (sTeLIC) gated by alkaline pH - R86A	X-Ray	3.30	10.1073/pnas.1717700115	2018
6FVR	The active form of a pentameric ion channel (sTeLIC) gated by alkaline pH - sTeLIC in complex with Cesium ions (Cs+)	X-Ray	4.20	10.1073/pnas.1717700115	2018
6FVS	The active form of a pentameric ion channel (sTeLIC) gated by alkaline pH - sTeLIC in complex with Barium ions (Ba2+)	X-Ray	3.20	10.1073/pnas.1717700115	2018
6HIN	Mouse serotonin 5-HT3 receptor, serotonin-bound, F conformation	Cryo-EM	4.10	10.1038/s41586-018-0672-3	2018
6HIO	Mouse serotonin 5-HT3 receptor, serotonin-bound, I1 conformation	Cryo-EM	4.20	10.1038/s41586-018-0672-3	2018
6HIQ	Mouse serotonin 5-HT3 receptor, serotonin-bound, I2 conformation	Cryo-EM	3.20	10.1038/s41586-018-0672-3	2018

PDB ID	Structure Title	Method	Resolution	DOI	Year
6HIS	Mouse serotonin 5-HT3 receptor, tropisetron-bound, T conformation	Cryo-EM	4.50	10.1038/s41586-018-0672-3	2018
6HY5	The GLIC Pentameric Ligand-Gated Ion Channel Mutant Q193C	X-Ray	2.58	10.1073/pnas.1813378116	2018
6HY9	The GLIC Pentameric Ligand-Gated Ion Channel Mutant Q193M	X-Ray	2.95	10.1073/pnas.1813378116	2018
6HYA	The GLIC Pentameric Ligand-Gated Ion Channel Mutant Q193L	X-Ray	3.39	10.1073/pnas.1813378116	2018
6HYR	The GLIC Pentameric Ligand-Gated Ion Channel Mutant Q193C+Mmts	X-Ray	3.50	10.1073/pnas.1813378116	2018
6HYV	The GLIC Pentameric Ligand-Gated Ion Channel Mutant Y119A	X-Ray	2.80	10.1073/pnas.1813378116	2018
6HYW	The GLIC Pentameric Ligand-Gated Ion Channel Mutant Y119F	X-Ray	2.80	10.1073/pnas.1813378116	2018
6HYX	The GLIC Pentameric Ligand-Gated Ion Channel Mutant Y197F-P250C	X-Ray	3.00	10.1073/pnas.1813378116	2018
6HYZ	The GLIC Pentameric Ligand-Gated Ion Channel Mutant K248C	X-Ray	3.05	10.1073/pnas.1813378116	2018
6HZ0	The GLIC Pentameric Ligand-Gated Ion Channel Mutant K248A	X-Ray	2.75	10.1073/pnas.1813378116	2018
6HZ1	The GLIC Pentameric Ligand-Gated Ion Channel Mutant E243C	X-Ray	2.50	10.1073/pnas.1813378116	2018
6HZ3	The GLIC Pentameric Ligand-Gated Ion Channel Mutant E243G	X-Ray	3.15	10.1073/pnas.1813378116	2018
6HZW	The Glic Pentameric Ligand-Gated Ion Channel 2.22 Resolution	X-Ray	2.22	10.1073/pnas.1813378116	2018
6I08	The Glic Pentameric Ligand-Gated Ion Channel Mutant E243C-I201W	X-Ray	3.00	10.1073/pnas.1813378116	2018
5IUX	GLIC-V135C bimane labelled X-ray structure	X-Ray	2.60	10.7554/eLife.23955	2017
5L47	X-ray structure of the 2-22' locally-closed mutant of GLIC in complex with cyanoselenobarbital (seleniated barbiturate)	X-Ray	3.30	10.1074/jbc.M116.766964	2017
5L4E	X-ray structure of the 2-22' locally-closed mutant of GLIC in complex with thiopental	X-Ray	3.50	10.1074/jbc.M116.766964	2017
5L4H	X-ray structure of the 2-22' locally-closed mutant of GLIC in complex with 5-(2-BROMO-ETHYL)-5-ETHYL-PYRIMIDINE-2,4,6-TRIONE (brominated barbiturate)	X-Ray	3.30	10.1074/jbc.M116.766964	2017
5SXU	X-ray structure of 2-bromoethanol bound to a pentameric ligand gated ion channel (ELIC) in a desensitized state	X-Ray	3.10	10.1016/j.str.2016.11.007	2017

PDB ID	Structure Title	Method	Resolution	DOI	Year
5SXV	X-ray structure of 2-bromoethanol bound to a pentameric ligand gated ion channel (ELIC) in a resting state	X-Ray	3.40	10.1016/j.str.2016.11.007	2017
5V6N	Crystal Structure of the highly open channel-stabilized mutant C27S + K33C + I9'A + N21'C of GLIC under reducing conditions.	X-Ray	3.36	10.1085/jgp.201711803	2017
5V6O	Crystal Structure of the highly open channel-stabilized mutant G-2'I + I9'A of GLIC	X-Ray	3.12	10.1085/jgp.201711803	2017
5VDH	Crystal Structure of Human Glycine Receptor alpha-3 Bound to AM-3607, Glycine, and Ivermectin	X-Ray	2.85	10.1016/j.str.2017.04.007	2017
5VDI	Crystal Structure of Human Glycine Receptor alpha-3 Mutant N38Q Bound to AM-3607, Glycine, and Ivermectin	X-Ray	3.10	10.1016/j.str.2017.04.007	2017
6F0I	GLIC mutant E26A	X-Ray	3.00	10.1371/journal.pbio.2004470	2017
6F0J	GLIC mutant E26A	X-Ray	3.15	10.1371/journal.pbio.2004470	2017
6F0M	GLIC mutant E35Q	X-Ray	2.65	10.1371/journal.pbio.2004470	2017
6F0N	GLIC mutant E82A	X-Ray	3.20	10.1371/journal.pbio.2004470	2017
6F0R	GLIC mutant E82Q	X-Ray	2.50	10.1371/journal.pbio.2004470	2017
6F0U	GLIC mutant E35A	X-Ray	2.35	10.1371/journal.pbio.2004470	2017
6F0V	GLIC mutant E82Q	X-Ray	2.85	10.1371/journal.pbio.2004470	2017
6F0Z	GLIC mutant D88N	X-Ray	2.50	10.1371/journal.pbio.2004470	2017
6F10	GLIC mutant D88N	X-Ray	2.85	10.1371/journal.pbio.2004470	2017
6F11	GLIC mutant D86A	X-Ray	2.95	10.1371/journal.pbio.2004470	2017
6F12	GLIC mutant E181A	X-Ray	3.20	10.1371/journal.pbio.2004470	2017
6F13	GLIC mutant E75A	X-Ray	2.70	10.1371/journal.pbio.2004470	2017
6F15	GLIC mutant H127Q	X-Ray	2.85	10.1371/journal.pbio.2004470	2017
6F16	GLIC mutant H277Q	X-Ray	2.60	10.1371/journal.pbio.2004470	2017
4ZZB	The GLIC pentameric Ligand-Gated Ion Channel Locally-closed form complexed to xenon	X-Ray	3.40	10.1371/journal.pone.0149795	2016
4ZZC	The GLIC pentameric Ligand-Gated Ion Channel open form complexed to xenon	X-Ray	3.10	10.1371/journal.pone.0149795	2016
5HCJ	Cationic Ligand-Gated Ion Channel	X-Ray	2.95	10.1016/j.str.2016.02.014	2016
5HCM	The GLIC pentameric Ligand-Gated Ion Channel 2-21' cross-linked mutant complexed to bromoform	X-Ray	3.15	10.1016/j.str.2016.02.014	2016
5HEG	Pentameric ligand-gated ion channel GLIC mutant P246G	X-Ray	3.21	10.1371/journal.pbio.1002393	2016
5HEH	Pentameric ligand-gated ion channel GLIC mutant P246A	X-Ray	3.30	10.1371/journal.pbio.1002393	2016
5HEJ	Pentameric ligand-gated ion channel ELIC mutant F116A	X-Ray	3.50	10.1371/journal.pbio.1002393	2016
5HEO	Pentameric ligand-gated ion channel ELIC mutant P254G	X-Ray	3.30	10.1371/journal.pbio.1002393	2016
5HEU	Pentameric ligand-gated ion channel ELIC mutant A257Y	X-Ray	3.20	10.1371/journal.pbio.1002393	2016
5HEW	Pentameric ligand-gated ion channel ELIC mutant T28D	X-Ray	4.50	10.1371/journal.pbio.1002393	2016

PDB ID	Structure Title	Method	Resolution	DOI	Year
5KXI	X-ray structure of the human Alpha4Beta2 nicotinic receptor	X-Ray	3.94	10.1038/nature19785	2016
5LG3	X-ray structure of a pentameric ligand gated ion channel from Erwinia chrysanthemi (ELIC) in complex with chlorpromazine	X-Ray	3.57	10.1073/pnas.1603101113	2016
5LID	X-ray structure of a pentameric ligand gated ion channel from Erwinia chrysanthemi (ELIC) in complex with bromopromazine	X-Ray	4.50	10.1073/pnas.1603101113	2016
3JAD	Structure of alpha-1 glycine receptor by single particle electron cryo-microscopy, strychnine-bound state	Cryo-EM	3.90	10.1038/nature14853	2015
3JAE	Structure of alpha-1 glycine receptor by single particle electron cryo-microscopy, glycine-bound state	Cryo-EM	3.90	10.1038/nature14853	2015
3JAF	Structure of alpha-1 glycine receptor by single particle electron cryo-microscopy, glycine/ivermectin-bound state	Cryo-EM	3.80	10.1038/nature14853	2015
4QH1	The GLIC pentameric Ligand-Gated Ion Channel (wild-type) in complex with bromoacetate	X-Ray	3.40		2015
4QH5	The GLIC pentameric Ligand-Gated Ion Channel (wild-type) crystallized in phosphate buffer	X-Ray	3.00		2015
4Z90	ELIC bound with the anesthetic isoflurane in the resting state	X-Ray	3.00	10.1038/srep13833	2015
4Z91	ELIC cocrystallized with isofluorane in a desensitized state	X-Ray	3.39	10.1038/srep13833	2015
5CFB	Crystal Structure of Human Glycine Receptor alpha-3 Bound to Strychnine	X-Ray	3.04	10.1038/nature14972	2015
4COF	Crystal structure of a human gamma-aminobutyric acid receptor, the GABA(A)R-beta3 homopentamer	X-Ray	2.97	10.1038/nature13293	2014
4NPP	The GLIC-His10 wild-type structure in equilibrium between the open and locally-closed (LC) forms	X-Ray	3.35	10.1073/pnas.1314997111	2014
4NPQ	The resting-state conformation of the GLIC ligand-gated ion channel	X-Ray	4.35	10.1073/pnas.1314997111	2014
4PIR	X-ray structure of the mouse serotonin 5-HT3 receptor	X-Ray	3.50	10.1038/nature13552	2014
4TWD	X-ray structure of a pentameric ligand gated ion channel from Erwinia chrysanthemi (ELIC) in complex with memantine	X-Ray	3.20	10.1016/j.str.2014.07.013	2014
4TWF	X-ray structure of a pentameric ligand gated ion channel from Erwinia chrysanthemi (ELIC) in complex with bromomemantine	X-Ray	3.90	10.1016/j.str.2014.07.013	2014

PDB ID	Structure Title	Method	Resolution	DOI	Year
4TWH	X-ray structure of a pentameric ligand gated ion channel from Erwinia chrysanthemi (ELIC) mutant F16'S	X-Ray	3.60	10.1016/j.str.2014.07.013	2014
2M6B	Structure of full-length transmembrane domains of human glycine receptor alpha1 monomer subunit	NMR		10.1016/j.str.2013.07.014	2013
2M6I	Putative pentameric open-channel structure of full-length transmembrane domains of human glycine receptor alpha1 subunit	NMR		10.1016/j.str.2013.07.014	2013
2MAW	NMR structures of the alpha7 nAChR transmembrane domain.	NMR		10.1074/jbc.M113.508333	2013
3ZKR	X-ray structure of a pentameric ligand gated ion channel from Erwinia chrysanthemi (ELIC) in complex with bromoform	X-Ray	3.65	10.1074/jbc.M112.424507	2013
4BOG	The structure and super-organization of acetylcholine receptor-rapsyn complexes	Cryo-EM	50.00	10.1073/pnas.1301277110	2013
4BOI	The structure and super-organization of acetylcholine receptor-rapsyn complexes class A	Cryo-EM	41.00	10.1073/pnas.1301277110	2013
4BON	The structure and super-organization of acetylcholine receptor-rapsyn complexes class B	Cryo-EM	40.00	10.1073/pnas.1301277110	2013
4BOO	The structure and super-organization of acetylcholine receptor-rapsyn complexes class C	Cryo-EM	42.00	10.1073/pnas.1301277110	2013
4BOR	The structure and super-organization of acetylcholine receptor-rapsyn complexes class D	Cryo-EM	42.00	10.1073/pnas.1301277110	2013
4BOT	The structure and super-organization of acetylcholine receptor- rapsyn complexes class E	Cryo-EM	42.00	10.1073/pnas.1301277110	2013
4HFB	The GLIC pentameric Ligand-Gated Ion Channel F14'A ethanol-sensitive mutant (Apo)	X-Ray	2.75	10.1038/ncomms2682	2013
4HFC	The GLIC pentameric Ligand-Gated Ion Channel F14'A ethanol-sensitive mutant complexed to 2-bromo-ethanol	X-Ray	3.05	10.1038/ncomms2682	2013
4HFD	The GLIC pentameric Ligand-Gated Ion Channel F14'A ethanol-sensitive mutant complexed to bromoform	X-Ray	3.10	10.1038/ncomms2682	2013
4HFE	The GLIC pentameric Ligand-Gated Ion Channel F14'A ethanol-sensitive mutant complexed to ethanol	X-Ray	2.80	10.1038/ncomms2682	2013

PDB ID	Structure Title	Method	Resolution	DOI	Year
4HFH	The GLIC pentameric Ligand-Gated Ion Channel (wild-type) complexed to bromoform	X-Ray	2.65	10.1038/ncomms2682	2013
4HFI	The GLIC pentameric Ligand-Gated Ion Channel at 2.4 A resolution	X-Ray	2.40	10.1038/emboj.2013.17	2013
4IL4	The pentameric ligand-gated ion channel GLIC in complex with Se-DDM	X-Ray	3.30	10.1038/emboj.2013.17	2013
4IL9	The pentameric ligand-gated ion channel GLIC A237F in complex with bromide	X-Ray	2.83	10.1038/emboj.2013.17	2013
4ILA	The pentameric ligand-gated ion channel GLIC A237F in complex with Cesium	X-Ray	3.50	10.1038/emboj.2013.17	2013
4ILB	The pentameric ligand-gated ion channel GLIC A237F in complex with Rubidium	X-Ray	3.15	10.1038/emboj.2013.17	2013
4ILC	The GLIC pentameric ligand-gated ion channel in complex with sulfates	X-Ray	2.99	10.1038/emboj.2013.17	2013
4IRE	Crystal structure of GLIC with mutations at the loop C region	X-Ray	3.19	10.1371/journal.pone.0064326	2013
4LMJ	GLIC Liganded-closed-channel Conformation, Mutant T25'A	X-Ray	3.44	10.1073/pnas.1313156110	2013
4LMK	GLIC Liganded-closed-channel Conformation, Mutant Y27'A	X-Ray	3.22	10.1073/pnas.1313156110	2013
4LML	GLIC double mutant I9'A T25'A	X-Ray	3.80	10.1073/pnas.1313156110	2013
2YN6	Pentameric Ligand-Gated Ion Channel ELIC in Complex with Barium	X-Ray	3.31	10.1371/journal.pbio.1001429	2012
2YOE	X-ray structure of a pentameric ligand gated ion channel from Erwinia chrysanthemi (ELIC) in complex with GABA and flurazepam	X-Ray	3.90	10.1073/pnas.1208208109	2012
3RQU	Crystal structure of a prokaryotic pentameric ligand-gated ion channel, ELIC	X-Ray	3.09	10.1038/ncomms1703	2012
3RQW	Crystal structure of acetylcholine bound to a prokaryotic pentameric ligand-gated ion channel, ELIC	X-Ray	2.91	10.1038/ncomms1703	2012
3TLS	The GLIC pentameric Ligand-Gated Ion Channel E19'P mutant in a locally-closed conformation (LC2 subtype)	X-Ray	3.20	10.1038/nsmb.2307	2012
3TLT	The GLIC pentameric Ligand-Gated Ion Channel H11'F mutant in a locally-closed conformation (LC1 subtype)	X-Ray	3.30	10.1038/nsmb.2307	2012
3TLU	The GLIC pentameric Ligand-Gated Ion Channel Loop2-24' oxidized mutant in a locally-closed conformation (LC1 subtype)	X-Ray	2.85	10.1038/nsmb.2307	2012

PDB ID	Structure Title	Method	Resolution	DOI	Year
3TLV	The GLIC pentameric Ligand-Gated Ion Channel Loop2-22' oxidized mutant in a locally-closed conformation (LC3 subtype)	X-Ray	2.90	10.1038/nsmb.2307	2012
3TLW	The GLIC pentameric Ligand-Gated Ion Channel Loop2-21' oxidized mutant in a locally-closed conformation (LC2 subtype)	X-Ray	2.60	10.1038/nsmb.2307	2012
3UQ4	X-ray structure of a pentameric ligand gated ion channel from Erwinia chrysanthemi (ELIC) mutant F247L (F16L)	X-Ray	3.50	10.1073/pnas.1119268109	2012
3UQ5	X-ray structure of a pentameric ligand gated ion channel from Erwinia chrysanthemi (ELIC) mutant L240A F247L (L9A F16L) in the presence of 10 mM cysteamine	X-Ray	4.20	10.1073/pnas.1119268109	2012
3UQ7	X-ray structure of a pentameric ligand gated ion channel from Erwinia chrysanthemi (ELIC) mutant L240S F247L (L9S F16L) in presence of 10 mM cysteamine	X-Ray	3.80	10.1073/pnas.1119268109	2012
3UU3	The GLIC pentameric Ligand-Gated Ion Channel Loop2-20' oxidized mutant in a locally-closed conformation (LC1 subtype)	X-Ray	3.15	10.1038/nsmb.2307	2012
3UU4	The GLIC pentameric Ligand-Gated Ion Channel Loop2-21' mutant reduced in the crystal in a locally-closed conformation (LC1 subtype)	X-Ray	3.05	10.1038/nsmb.2307	2012
3UU5	The GLIC pentameric Ligand-Gated Ion Channel Loop2-20' mutant reduced in solution	X-Ray	2.90	10.1038/nsmb.2307	2012
3UU6	The GLIC pentameric Ligand-Gated Ion Channel Loop2-22' mutant reduced in solution	X-Ray	2.98	10.1038/nsmb.2307	2012
3UU8	The GLIC pentameric Ligand-Gated Ion Channel Loop2-24' mutant reduced in solution	X-Ray	3.25	10.1038/nsmb.2307	2012
3UUB	The GLIC pentameric Ligand-Gated Ion Channel Loop2-21' mutant reduced in solution	X-Ray	2.90	10.1038/nsmb.2307	2012
4A97	X-ray structure of a pentameric ligand gated ion channel from Erwinia chrysanthemi (ELIC) in complex with zopiclone	X-Ray	3.34	10.1073/pnas.1208208109	2012
4A98	X-ray structure of a pentameric ligand gated ion channel from Erwinia chrysanthemi (ELIC) in complex with bromoflurazepam	X-Ray	3.61	10.1073/pnas.1208208109	2012
4AQ5	Gating movement in acetylcholine receptor analysed by time-resolved electron cryo-microscopy (closed class)	Cryo-EM	6.20	10.1016/j.jmb.2012.07.010	2012

PDB ID	Structure Title	Method	Resolution	DOI	Year
4AQ9	Gating movement in acetylcholine receptor analysed by time-resolved electron cryo-microscopy (open class)	Cryo-EM	6.20	10.1016/j.jmb.2012.07.010	2012
4F8H	X-ray Structure of the Anesthetic Ketamine Bound to the GLIC Pentameric Ligand-gated Ion Channel	X-Ray	2.99	10.1016/j.str.2012.08.009	2012
2YKS	Pentameric Ligand Gated Ion Channel Elic Mutant F246A	X-Ray	3.30	10.1371/journal.pbio.1001101	2011
3P4W	Structure of desflurane bound to a pentameric ligand-gated ion channel, GLIC	X-Ray	3.20	10.1038/nature09647	2011
3P50	Structure of propofol bound to a pentameric ligand-gated ion channel, GLIC	X-Ray	3.30	10.1038/nature09647	2011
3RHW	C. elegans glutamate-gated chloride channel (GluCl) in complex with Fab and ivermectin	X-Ray	3.26	10.1038/nature10139	2011
2XQ3	Pentameric ligand gated ion channel GLIC in complex with Br-lidocaine	X-Ray	3.50	10.1038/nsmb.1933	2010
2XQ4	Pentameric ligand gated ion channel GLIC in complex with tetramethylarsonium (TMAs)	X-Ray	3.60	10.1038/nsmb.1933	2010
2XQ5	Pentameric ligand gated ion channel GLIC in complex with tetraethylarsonium (TEAs)	X-Ray	3.50	10.1038/nsmb.1933	2010
2XQ6	Pentameric ligand gated ion channel GLIC in complex with cesium ion (Cs+)	X-Ray	3.70	10.1038/nsmb.1933	2010
2XQ7	Pentameric ligand gated ion channel GLIC in complex with cadmium ion (Cd2+)	X-Ray	3.40	10.1038/nsmb.1933	2010
2XQ8	Pentameric ligand gated ion channel GLIC in complex with zinc ion (Zn2+)	X-Ray	3.60	10.1038/nsmb.1933	2010
2XQ9	Pentameric ligand gated ion channel GLIC mutant E221A in complex with tetraethylarsonium (TEAs)	X-Ray	3.20	10.1038/nsmb.1933	2010
2XQA	Pentameric ligand gated ion channel GLIC in complex with tetrabutylantimony (TBSb)	X-Ray	3.70	10.1038/nsmb.1933	2010
3IGQ	Crystal structure of the extracellular domain of a bacterial pentameric ligand-gated ion channel	X-Ray	2.30	10.1016/j.jmb.2009.11.024	2010
3LSV	Structure of the A237F mutant of the pentameric ligand gated ion channel from Gloeobacter Violaceus	X-Ray	3.15	10.1073/pnas.1001832107	2010
3EAM	An open-pore structure of a bacterial pentameric ligand-gated ion channel	X-Ray	2.90	10.1038/nature07462	2009
2VL0	X-ray structure of a pentameric ligand gated ion channel from Erwinia chrysanthemi (ELIC)	X-Ray	3.30	10.1038/nature06717	2008

PDB ID	Structure Title	Method	Resolution	DOI	Year
3EHZ	X-ray structure of the pentameric ligand gated ion channel of Gloebacter violaceus (GLIC) in a presumptive open conformation	X-Ray	3.10	10.1038/nature07461	2008
3EI0	Structure of the E221A mutant of the Gloebacter violaceus pentameric ligand gated ion channnel (GLIC)	X-Ray	3.50	10.1038/nature07461	2008
2BG9	Refined Structure Of The Nicotinic Acetylcholine Receptor At 4A Resolution.	Cryo-EM	4.00	10.1016/j.jmb.2004.12.031	2005
1OED	Structure Of Acetylcholine Receptor Pore From Electron Images	Cryo-EM	4.00	10.1038/nature01748	2003
4QH4	The GLIC pentameric Ligand-Gated Ion Channel (wild-type) crystallized in acetate buffer at pH3	X-Ray	3.20		
5J0Z	Crystal structure of GLIC in complex with DHA	X-Ray	3.25		
5MVM	X-ray structure of the F14'A - N15'A double mutant of GLIC in complex with propofol	X-Ray	3.10		
5MZR	X-ray structure of the H235Q mutant of GLIC in complex with propofol	X-Ray	2.65		
5MZT	X-ray structure of the H235Q mutant of GLIC in complex with bromoform	X-Ray	2.65		
5NJY	X-ray structure of the H235Q mutant of GLIC	X-Ray	2.95		
5TIN	Crystal Structure of Human Glycine Receptor alpha-3 Mutant N38Q Bound to AM-3607	X-Ray	2.61		
5TIO	Crystal Structure of Human Glycine Receptor alpha-3 Bound to AM-3607	X-Ray	3.25		